

**DESIGN, FABRICATION AND THERMOMECHANICAL TESTING OF A
VERTICAL BIMORPH SENSOR IN THE
WAFER PLANE**

A Thesis

Submitted to the Graduate Faculty of the
Louisiana State University and
Agricultural and Mechanical College
in partial fulfillment of the
requirements for the degree of
Master of Science in Mechanical Engineering

in

The Department of Mechanical Engineering

by

Madhulika Sathe
B.Tech, Bapatla Engineering College, India, 2000
December 2004

To my husband Akshay and my parents Meera and Dilip Sathe, who always believed in me and were there for me at each and every stage of life

ACKNOWLEDGEMENTS

I have learned a lot during the course of completion of my thesis. I have grown both emotionally and intellectually. I undertook more roles than any one around me. I was a tutor for LSU student athletes in the Department of Kinesiology for two semesters and then I worked as a student worker and as graduate assistant at CAMD. I was also a TA for three semesters for Capstone Design and Fundamentals of Instrumentation Lab. I was juggling between CAMD and LSU many number of times for almost three years just to catch up with all the work. During summer of 2002, I was given a role of surveyor through Department of Sociology for conducting survey of people on social security. I used to commute between Baton Rouge and New Orleans for almost three months. I used to go door to door to conduct interviews.

I finished my research in October 2003 and since then my defense had been scheduled nine times, before I defended on August 5, 2004. In Spring 2004 I had moved to New Orleans with my husband and so I was again commuting between New Orleans and Baton Rouge until September 10, 2004 when I finally received my thesis approval sheet.

My role model in this passage was my mother. There were many occasions when I felt lonely and betrayed. At that time I would think “What would she do, if she was in the same situation?” She has shown me how to lead life with courage and determination.

I am grateful to Dean Monroe for being a guide and a counselor to me. I would like to thank Dr. Charalampopoulos for his encouragement and support. I would also like to thank Dr. Sinclair for his cooperation and mediation.

Dr. Podlaha taught me electrochemistry and was always patient with me. I extend my gratitude towards her. I learnt modeling from Dr. Wang. I would like to thank him for the classes that I took with him which helped me with my research. I would like to express thanks to Dr. Acharya for providing the basic foundation for the project.

My uncle, Dr. Vijay Singh, provided me with the right amount of courage to take better decisions each time my life went downhill. I would like to thank my uncle and my aunt to help me build up my morale from time to time. I would like to express my thanks to my brother-in-law, Abhishek, who drove 725 miles one way from Fayetteville to Baton Rouge at a moments notice to attend my thesis defense.

I would like to thank my husband, Akshay who was always with me in all the ups and downs. He taught me to be independent and emotionally strong. If it were not for him, I would have quit my degree long time back. He was always optimistic and provided unyielding support. We were married on January 16, 2004.

My parents helped me to reach where I am today. I would like to express my sincere gratitude to them. I would like to thank my brother Nilesh, for bringing out the best in me. I would also like to extend my heartfelt gratefulness to my mother-in-law and father-in-law whose encouraging words have always uplifted me. Last but not least, I thank my grandmother who showed me how to prove your enemies wrong by challenging the adversities of life and come out victorious.

TABLE OF CONTENTS

ACKNOWLEDGEMENTS.....	iii
ABSTRACT.....	viii
1. INTRODUCTION.....	1
1.1 Introduction to the Project.....	1
1.2 Project Requirements.....	2
1.3 Thesis Outline.....	5
2. BACKGROUND.....	6
2.1 Temperature Measurements Techniques.....	6
2.1.1 Bimetallic.....	7
2.1.2 Resistive.....	8
2.1.3 Thermo-couple Thermometers.....	11
2.2 Detailed Description to the Bimetallic Effect.....	15
2.3 Applications of the Bimetallic Effect.....	16
3. ANALYTICAL MODELING AND NUMERICAL SIMULATION (BIMETALLIC BEAMS AND GOVERNING BOUNDARY CONDITIONS).....	22
3.1 Introduction.....	22
3.2 Analytical Modeling.....	24
3.2.1 Linear Bi-metallic Beam.....	24
3.2.2 Reactions at Each Strip.....	29
3.2.3 Modeling for Recurve Architecture.....	31
3.3 Analytical and Numerical Simulation.....	34
3.3.1 Free Deflection.....	35
3.3.2 Blocking Force.....	36
3.3.3 Self Weight Analysis.....	39
3.3.4 Thermal Deflection.....	40
3.3.5 Thermal Stresses.....	41
3.3.6 Temperature Response.....	42
3.4 Summary.....	44
4. PROCESS COMPARISION.....	46
4.1 Background.....	46
4.2 Criterion for X-Ray Mask Fabrication.....	46
4.3 First Generation Process.....	47
4.4 Second Generation Process.....	48
4.5 Comparison of Two Generations.....	49
4.6 Types of X-Ray Mask.....	53
4.6.1 Basic X-Ray Mask.....	54
4.6.2 X-Ray Mask for Aligned Exposure.....	56
4.7 Summary.....	57

5. FABRICATION OF RECURVE STRUCTURE.....	58
5.1 Introduction.....	58
5.2 Analysis of First and Second Generation Process Based on Tolerance Stacking..	58
5.3 Fabrication Process for the Improved Second Generation.....	63
5.3.1 Substrate Preparation.....	63
5.3.2 PMMA Bonding.....	64
5.3.3 X-Ray Exposure and Development.....	65
5.3.4 Invar Electrodeposition.....	66
5.3.5 Lapping and Polishing.....	67
5.3.6 PMMA Casting.....	67
5.3.7 Aligned Exposure and Development.....	68
5.3.8 Electroplating of Ni.....	69
5.3.9 Etching and Release of the Recurve Structures.....	70
5.4 Summary.....	71
6. INVAR PROPERTIES AND ELECTRODEPOSITION.....	73
6.1 Introduction.....	73
6.2 Invar.....	73
6.3 Investigation of Nickel-Iron Alloys for MEMS.....	76
6.4 Electrodeposition.....	77
6.5 Performance Measurement of Invar Electrodeposition.....	78
6.5.1 Test Sample Preparation and Results.....	78
6.5.2 CTE Measurements.....	81
6.5.3 Advantages of Pulse Plating.....	82
6.6 Summary.....	83
7. EXPERIMENTAL MEASUREMENTS.....	85
7.1 Introduction to the Dynamic Mechanical Analyzer (DMA).....	85
7.2 Experimental Setup.....	86
7.3 Test Results and Discussions.....	87
7.4 Comparison of Analytical, Numerical and Experimental Results.....	91
7.5 Summary.....	94
8. CONCLUSIONS AND RECOMMENDATIONS.....	96
8.1 Summary of Results.....	96
8.2 Recommendations to the Future Work.....	99
REFERENCES.....	101
APPENDIX A. X-RAY MASK FABRICATION.....	106
APPENDIX B. RECIPE AND DATA SHEETS.....	109
APPENDIX C. PERCENT COMPOSITION OF NICKEL AND IRON ALONG THE LENGTH OF THE POST.....	111

APPENDIX D. PROCESS SHEET FOR FABRICATION OF THE RECURVE.....	113
APPENDIX E. RECIPE AND DATA SHEETS FOR FABRICATION OF DEVICE...	115
APPENDIX F. EXPERIMENTAL RESULTS.....	116
APPENDIX G. COMMAND FILE FOR DEFLECTION OF RECURVE ELEMENT UNDER THERMAL LOAD.....	122
VITA.....	124

ABSTRACT

A bimetallic recurve device was designed, fabricated and tested as a temperature sensor. The device is to be used for sensing temperatures up to 300°C inside oil wells for downhole condition monitoring. Continuous downhole measurements at high temperatures and pressures are required to monitor conditions downhole instruments are exposed to during use. Currently mercury thermometers and resistive temperature detectors (RTD) are used for downhole temperature measurements. Microsensors have potential application downhole, due to their small size and inherent robustness.

The principle of a bimetallic beam was used to measure temperature. A bimetallic beam deflects with changes in temperature due to differential thermal expansion of the two materials in the beam. Analytical and numerical models were developed for parametric analysis of recurve thermomechanical elements. Invar was electrodeposited with the desired ratio through the depth of the structures of Ni to Fe as 36%:64%. Prototype recurve structures were fabricated using the LIGA microfabrication process. X-ray masks were designed and fabricated to improve the alignment process. A substrate containing twelve different devices was fabricated using a two mask process, with eleven of the structures successfully released.

Recurve structures 8 mm long with a 500 μm X 100 μm cross-sections were tested using a dynamic mechanical analyzer. The prototypes were loaded at room temperature and a heating rate of 10°C/min was applied in 20°C steps, with a one minute hold at each step for deflection measurement, until the temperature reached 300°C. The deflection was measured using a probe tip resting against the sample with a force of 0.0001N. Deflection increased linearly to a maximum deflection of 65 μm at a

temperature of 200°C. With further increase in temperature, the deflection was found to decrease linearly. The Curie effect was hypothesized to influence this behavior of the Invar alloy. The analytical model of the bimetallic recurve beam with the given experimental conditions and nominal dimensions predicted a maximum free deflection of 54.17 μm at 200°C. Differences were attributed to differences between the experimental conditions and model assumptions.

1. INTRODUCTION

1.1 INTRODUCTION TO THE PROJECT

Microelectromechanical Systems, or MEMS, are integrated micro devices or systems combining electrical and mechanical components. They range in size from micrometers to millimeters. These systems can sense, control and actuate on the micro-scale, and function individually or in arrays to generate effects on the macroscale. Micro-machines are divided into two functional groups: sensors and actuators. Sensors and actuators are incorporated for the condition monitoring of the device. They occupy a minimum volume and thus do not interfere with the primary functions. A sensor is defined as a device that provides a usable output signal in response to an input signal. Sensor principles are based on physical or chemical effects (Jerman and Terry, 1997).

Temperature is a fundamental physical quantity. Several phenomena or effects are used to assess temperature change. The simplest and most widely used principle in the design of temperature sensors is thermal expansion. The best known example is the liquid-in-glass thermometer. However, temperature can be measured with resistive temperature detectors (RTDs), thermistors, thermocouples, thermoelectric contact sensors and semiconductor, optical and piezoelectric temperature detectors (Webster, 2000).

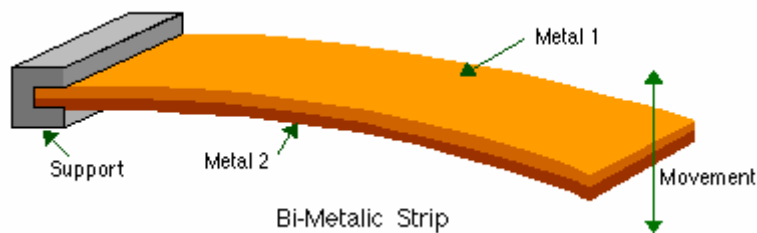


Figure 1: Bimetallic strip.

Another example is temperature measurement by sensing the deflection of a bimetallic beam. In a bimetallic beam two different materials, usually metals, with a significant difference in coefficient of thermal expansion (CTE) are joined throughout their length (Fukuda, 1998). Figure 1 gives a schematic of the bimetallic strip. The bimetallic beam deflects due to variation in temperature causing the cross-sectional plane to bend.

1.2 PROJECT REQUIREMENTS

The project goal was to design and test the bimetallic recurve as a temperature sensor. The temperature sensor was to be used to monitor the temperature inside an oil well. Temperature measurements are performed periodically to monitor the environmental conditions downhole. Currently mercury thermometers and RTDs with 100 ohm resistance which are several inches in dimensions are used for downhole temperature measurements.

The temperature measuring device had to be robust and able to survive high temperatures. The maximum operating temperature was set to 300 °C. It also must be small and light weight.

The proposed solution of using a thermomechanical bimorph as the sensing element is justified due to many reasons. The device would be smaller in size. It was robust and the deflection produced was predicted to be linear with temperature.

The design of recurve architecture was based on the work done by Ervin and Brei (1998). Bimorph piezoelectric elements stacked in a recurve configuration were introduced to produce the linear, large stroke displacements required for sensing and actuation. The recurve principle was later applied to a bimetallic thermomechanical

recurve pattern by Datta (2001) and Datta et al. (2003). The bimetallic recurve deflected with changes in temperature with no tip rotation, unlike in a cantilever bimetallic beam. The recurve elements can be replicated in arrays and tailored to produce a specific displacement output or configured in a variety of ways to make efficient use of the available design space. The basic building block is a thermally-actuated recurve element of nickel and Invar-like nickel-iron. Invar is an alloy (Ni 36 % and Fe 64%) that was used as a low expansion component due to its known low CTE (4.18×10^{-6} at room temperature (25°C): Marsh, 1938) and potential for electrodeposition. Nickel (CTE: 13.3×10^{-6} at room temperature (25°C): Marsh, 1938) used in conjunction with Invar provides a large difference in the CTE values, thus producing a greater deflection.

In the previous work (Datta, 2001) many problems were encountered in the fabrication process for the thermal recurve. The recurve structures could not be released effectively. These problems were carefully studied, by step-by-step analysis of the entire fabrication cycle.

One problem encountered during the fabrication process was that of alignment error. An X-ray mask was fabricated by transfer of a pattern by optical lithography to a graphite membrane. A three mask set was required to pattern the base layer (with alignment markers), the nickel layer, and the Invar layer. These markers were used for aligning both of the X-ray masks. Alignment of all the three different layers is necessary for successful fabrication of the bimorph structures. A manual alignment system ($\pm 10 \mu\text{m}$) at the Center for Advanced Microsystems and Devices (CAMD) was used leading to significant offset. An effective way to align the pattern was required.

The main problem encountered, however, was that of Invar electrodeposition. Earlier attempts made towards Invar plating resulted in cracks due to residual stress (Datta, 2001). The overall percent composition over the entire depth of deposit was also nonuniform. Namburi (Datta, et al., 2001) solved the problems by replacing the chloride ions in the electroplating solution by sulfate ions, chloride ions led to stress cracking in the posts, and by developing a pulse plating scheme to improve transport in the holes. The overall composition throughout the length of the post required further improvement.

A modified microfabrication process was required to successfully release the structures. The errors had to be reduced and quantified. The alignment process needed improvement to obtain the least amount of alignment error possible.

In this thesis analytical models were developed to parametrically evaluate different designs and evaluate the maximum stresses in the recurve elements. Posts with square cross section were plated and conditions governing the ratio of nickel and iron in the alloy were studied. The electroplating bath was adapted from work by Namburi (Datta, et al., 2001) and modified to achieve a more uniform ratio of Ni: Fe. It was found that the desired percentage of nickel and iron could be achieved by applying a duty cycle with a large ratio of 'OFF' time to 'ON' time. This helped mass transfer into the deep structures, yielding the desired composition and also greatly reducing the stress values, whereas in the previous thesis electrodeposition of Invar led to stress cracking. Micro-probe analysis of the posts revealed a consistent ratio of the constituent elements along the posts. The alloy samples were later analyzed for the CTE value and the results showed that electrodeposited samples had CTE's comparable to the bulk value.

The LIGA microfabrication process was used to fabricate the recurve arrays. To build up the recurve pattern, two X-ray exposures were performed, one for each layer of the bimetallic strip. These were released successfully and then tested using Dynamic Mechanical Analyzer (DMA 2980 Series, TA Instruments, Houston, TX), through a series of heating and cooling cycles, to record the deflection generated. The sample was loaded at room temperature and heated to a maximum temperature of 300 °C.

1.3 THESIS OUTLINE

The work carried out in this study is organized as follows. Chapter 1 and 2 deals with the introduction to the project and provides background for the project. Chapter 3 presents the analytical modeling performed and gives the results for the analytical and numerical simulations. The bimorph recurve architecture was characterized by analytical models of the thermal and mechanical behavior of the system. The X-ray mask was modified to eliminate the alignment error; the steps towards the modified X-ray mask are given in Chapter 4. Alignment of the pattern was reduced to two main steps. The ‘first alignment’ of the pattern was reduced to ‘no alignment’ step, as the X-ray mask was modified to pattern both the recurve and the alignment marks into one single X-ray exposure. The second alignment consisted of aligning the pattern marks with that of the X-ray mask. The details of the various steps involved in the fabrication of the bimetallic recurve are described in detail in Chapter-5. Characteristics of the Invar alloy and its plating are described in detail in Chapter 6 and the experimental test results and discussion are provided in Chapter 7. Finally, the results are summarized and recommendations for future work are presented in Chapter 8.

2. BACKGROUND

2.1 TEMPERATURE MEASUREMENT TECHNIQUES

Temperature is a measure of the thermodynamic state of an object or system. It is a macroscopic description of the aggregate amount of microscopic kinetic energy in a material. If two bodies are at the same temperature, they are in thermodynamic equilibrium with each other. If they were connected to each other, there is no net flow of heat from one to the other (Guyer, 1989). Selecting the right temperature sensor depends on the process being measured, the temperature range stipulated, the response time desired, the accuracy required, and the operating environment.

Temperature can be measured via a diverse array of sensors. All of them infer temperature by sensing some change in a physical characteristic. The most common one is the mercury thermometer. In other cases sensors generate output signals in one of two ways: through a change in output voltage or through a change in resistance of the sensor's electrical circuit. Thermocouples and IR devices generate voltage output signals. RTDs and thermistors output signals via a change in resistance (Busch-Vishniac, 1998).

To accommodate a variety of applications, the sensor industry has developed a number of temperature measurement techniques. This chapter investigates the various kinds of temperature sensing principles that can be used. The different types of temperature measuring principles outlined in the following sections are:

- Bimetallics
- Resistive temperature detector (RTD)
- Thermocouple thermometers

The next section describes each of these principles in detail.

2.1.1 BIMETALLIC

Bimetallic thermometers consist of two metals with different coefficients of thermal expansion bonded together. As the temperature varies from the temperature at which the metals were bonded, the metals expand by different amounts and the composite experiences a shearing force (Webster, 2000). The most common method of monitoring the shearing is to allow the metal composite to bend in response to temperature changes. The form of the composite can take on many configurations varying in complexity from a simple leaf spring fixed at one end with a pointer on the other to a small helix fixed at one end and a turning shaft at the other linked to a pointer, possibly through a gear train.

Since the temperature variations produce a force, there must be some graduated restoring force applied to the bimetallic strip. The most common approach is to use the bimetallic strip itself as a restoring spring. The final position of the strip is a balance between the shear imposed by the differing temperature coefficients and the spring force of the strip.

The ASTM Design Formula for bimetallic strips¹ for a simply supported beam is:

$$D = \frac{0.1325F \cdot \Delta T \cdot L^2}{t} \quad (1)$$

where

D = deflection for the beam (inches)

F = flexivity in the range of temperature change (inch-pound)

ΔT = temperature change (°C)

L = free deflection length (inches)

1 - ASTM Standard B388, Standard Specification for Thermostat Metal Sheet and Strip, ASTM International, October 2003.

t = thickness of strip (inches)

Here, flexivity is a bulk property intrinsic to a given alloy combination in a given temperature range. The parameters of the composite combination that determine flexivity are the coefficient of thermal expansion (CTE) of each component, the volume percent of each component, and the elastic modulus of each component. Since CTE is a function of temperature, so is flexivity (Guyer, 1989).

There are instances where bimetallic thermometers are required to actuate a switch. In these cases the load imposed by the switch must be overcome by the shear forces of the strip and the designer must consider it as an external load. The temperature range of bimetallic thermometers is limited by the annealing temperature or the phase transformations of the metals. Bimetallic strips are mainly used below 700°C, and they can be permanently damaged if the metals change their properties or the bond between the metals fails. A common example is the nickel steel, Invar, with a very low CTE ($4.18 \times 10^{-6} / ^\circ\text{C}$ at room temperature (25°C): Marsh, 1938) bonded to a brass alloy with a high CTE ($11 \times 10^{-6} / ^\circ\text{C}$ at room temperature (25°C): Marsh, 1938).

2.1.2 RESISTIVE

Resistive temperature detectors (or RTD's) are electrical temperature measurement instruments. The principle depends on the change in electrical resistance with a change in the temperature. The RTD can be used to measure any temperature from the measured change of the resistance.

- **Working Principle**

Temperature measurement with resistance is based on the intrinsic property of all conductors and semiconductors, namely that their resistance varies with temperature. The

measuring instrument applies a constant current through a RTD (Busch-Vishniac, 1998). As temperature increases the resistance increases, and as temperature drops the resistance decreases. This change in resistance is converted into temperature, usually through a curve fit for the resistance versus temperature characteristic for a specific material. Strain produced in the measuring wire also affects the resistance of the sensor.

Each metal has a specific and unique resistivity that can be determined experimentally. The resistance, R , is directly proportional to a metal wire's length, L , and inversely proportional to the cross-sectional area, A :

$$R = \rho L / A \quad (2)$$

where:

ρ = the constant of proportionality (Ωm)

- **Principle of Operation**

RTDs are manufactured from metals whose resistance increases with temperature. Within a limited temperature range, this resistivity increases linearly with temperature:

$$\rho_t = \rho_0 [1 + a (T - T_0)] \quad (3)$$

where:

ρ_t = resistivity at temperature, T (Ω)

ρ_0 = resistivity at a standard temperature, T_0 (Ω)

a = temperature coefficient of resistance ($^{\circ}\text{C}^{-1}$)

Combining Equations 2 and 3, setting t_0 to 0°C , and rearranging to obtain the standard linear equation

$$y = mx + b,$$

the resistance versus temperature is linear with a slope a ;

$$R/R_0 = aT + 1 \tag{4}$$

In theory, any metal could be used to measure temperature. The metal selected should have a high melting point and an ability to withstand the effects of corrosion. Platinum is the metal of choice for RTD's (Webster, 2000). Its desirable characteristics include chemical stability, availability in a pure form, and electrical properties that are highly reproducible.

- **Fabrication**

RTD elements take either of two forms: wire wound or thin film. Wire-wound elements are made primarily by winding a very fine strand of platinum wire into a coil until there is enough material to equal $100 \ \Omega$ of resistance. The coil is then inserted into a mandrel and powder is packed around it to prevent the sensor from shorting and to provide vibration resistance. Thin film elements are manufactured by depositing a thin layer of platinum or its alloys on a ceramic substrate. The metal is deposited in a specific pattern and trimmed to the final resistance. The elements are coated with a glass or epoxy for moisture resistance. An advantage of the thin film sensor is that a greater resistance can be placed in a smaller area; $1000 \ \Omega$ RTD sensors are readily available.

Several element configurations are available for different applications. The platinum RTD sensor generally provides better accuracy and long-term stability than thermocouple sensors. Calibration laboratories and standards bodies use platinum RTD sensors as reference instruments when calibrating other thermometers (Webster, 2000). Figure 2.1 shows a schematic of standard platinum RTD (wire wound). It is suitable for use from -50°C to 550°C when long-term stability and repeatability are required. RTD's produce an electrical signal and due to a much simpler interface with automatic controllers, provide a safer environment, unlike mercury thermometers (which are the basis of temperature measurement) for which the disposal of mercury is a problem.

2.1.3 THERMOCOUPLE THERMOMETERS

Another popular temperature sensor is the thermocouple. A pair of electrically conducting and thermoelectrically dissimilar materials coupled at an interface forms a thermocouple. It works on the Seebeck effect.

- **Working Principle**

The two junctions of a thermocouple are placed at two different temperature points. This produces a voltage, which is a product of the dissimilar metals at the same temperature. Any interface between dissimilar electric conductors is a thermoelectric junction (Figiola and Beasley, 2000). The thermoelements determine the thermocouple sensitivity and calibration. The net electromotive force is calibrated from the end points of the thermoelements. Proper alloy selection results in a measurable and predictable voltage-to-temperature relationship. The output voltage is generated along the length of the junction as it passes through a temperature variation. The thermocouple voltage is the difference between the thermoelectric energies of the chosen metals as measured at the

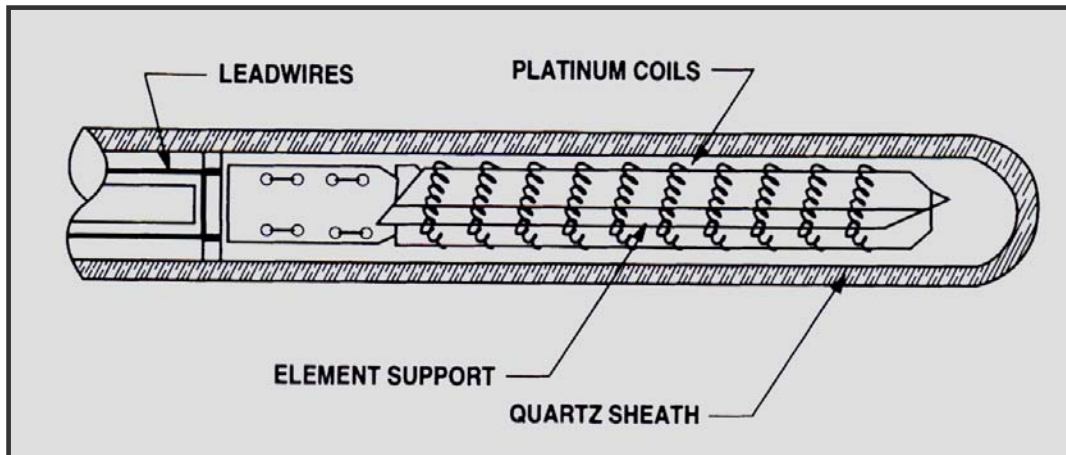


Figure 2.1 Standard platinum resistance thermometer (Webster, 2000).

instrument connection. This predictable voltage can be related to actual process temperature.

These devices are also best for applications requiring miniature sensor designs. The inherent simplicity enables them to withstand high shock and vibration entailing loads of up to 30,000 pounds (Webster, 2000). Thermocouples can be configured in small sizes to offer near-immediate response to temperature change (Webster, 2000).

- **Thermoelectric Effect**

If a conductor is heated at one end, the mechanism giving rise to a thermoelectric current is that the electrons at the "hot" end (hot junction) will acquire increased thermal energy relative to those at the "cold" end (cold or reference junction). The electrons from the hot end will diffuse to the cold end thus lowering their energy. This is essentially the manner in which heat is conducted in a metal and is accompanied by the accumulation of negative charge at the cold end, setting up an electric field or a potential difference between the ends of the material. The electric field will build up until a state of dynamic

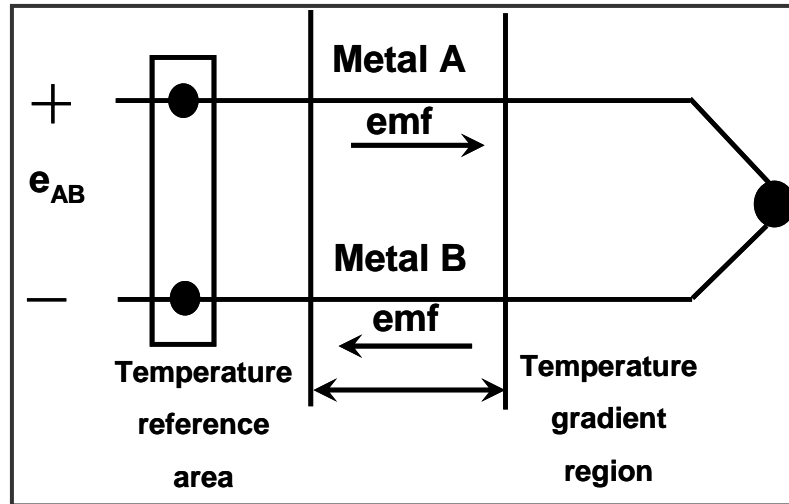


Figure 2.2: Thermocouple circuit (<http://allaboutcircuits.com>)

equilibrium is established between the electrons moving down the temperature gradient and electrostatic repulsion due to the excess of charge at the cold end. The number of electrons passing through a cross-section normal to the direction of flow in both directions will be equal, but the velocities of the electrons proceeding from the hot end will be higher than the velocities of the electrons passing through the section from the cold end. This difference ensures that there is a continuous transfer of heat (thermal conduction) down the temperature gradient without actual charge transfer once dynamic equilibrium is established. This phenomenon is the basis of the thermoelectric effects: Seebeck, Thompson and Peltier.

- **Principle of Operation**

The thermoelectric voltage resulting from the temperature difference from one end of the wire to the other is actually the sum of all the voltage differences along the wire from end to end:

$$V = \int_0^L S(dT / dx) dx \quad (5)$$

where:

$S = \text{Seebeck coefficient } (\mu\text{V}/^\circ\text{C})$

The temperature difference between the endpoints determines the net effect of the summation of all the infinitesimal voltages developed across the infinitesimal distances resulting from the temperature gradient. The Seebeck coefficient of a particular wire material is the first derivative of the thermoelectric voltage as a function of temperature, the difference in potential that results from a difference in temperature. Unfortunately, the Seebeck coefficient is not constant with temperature. The Seebeck coefficient for Type K thermocouples, for example, drops rapidly below 40°C , where it is $\sim 36 \mu\text{V}/^\circ\text{C}$, to $17.8 \mu\text{V}/^\circ\text{C}$ at 190°C (Webster, 2000). It peaks at $\sim 630^\circ\text{C}$ at $42 \mu\text{V}/^\circ\text{C}$ (Webster, 2000).

- **Fabrication**

Thermocouples come in a variety of shapes and sizes. An insulated wire product is the most common one. These special wire-formed metal alloys are covered with insulating material, which provides both physical and electrical isolation between thermocouple wire alloys. The insulating materials are operative in temperatures as high as 2300°F . This kind of thermocouple is cost-effective for short-term measurements. Junctions and instrumentation connections are easily fabricated on site.

The principal advantages of thermocouples are that they are inexpensive, provide moderately accurate and consistent measurements, and operate over a wide temperature range (from $<0^\circ\text{C}$ to $>1000^\circ\text{C}$) and are best suited for high temperatures. In the negative temperature range, thermocouples can be used to -200°C . For temperatures above 1000°C thermocouples made of platinum and a platinum/rhodium alloy are used. Thermocouples

of noble metal alloys can be used for monitoring and controlling temperatures as high as 3100°F.

Their principal disadvantage is that they produce small output voltages. For example, a Type J thermocouple (iron/constantan) produces only about 50 $\mu\text{V}/^\circ\text{C}$ (Webster, 2000). Since thermocouples do not have sensing elements, they are less limited than RTDs by the materials of construction. Thermocouples are normally built around bare conductors that are then insulated in a compacted ceramic powder or in formed ceramic insulators. This construction allows thermocouples to be used at much higher temperatures than RTDs can survive.

2.2 DETAILED DESCRIPTION OF THE BIMETALLIC EFFECT

The first known use of differential thermal expansion of metals in a mechanical device was that of the English clock maker John Harrison in 1735 (Goldstein et al., 1998). Harrison used two different metals in a clock escapement to account for the changes in temperature on board a ship. This marine chronometer used a grid of two metals that altered the flywheel period of the clock through a simple displacement. This mechanical actuation, resulting from the differential expansion of two metals in contact, is the basis for all bimetallic actuation.

The bimetallic effect is now used in numerous applications ranging from domestic appliances to compensation in satellites. The effect can be used in two ways: either as an actuator or as a temperature measurement system (or sensor). A bimetallic actuator consists of two metal strips fixed together. If the two metals have different CTE's then as the temperature of the actuator changes, one element will expand more than the other, causing the device to bend out of plane.

As a temperature measuring device, the bimetallic element, similar in design to that of the actuator above can be used to determine the ambient temperature if the degree of bending can be measured. The advantage of such a system is that the amount of bending can be mechanically amplified to produce a large and easily measurable displacement. In the basic model of a bimetallic actuator, two metal strips of different thermal expansion are bonded together. When the temperature of the assembly is changed, in the absence of external forces, the bimetallic actuator will take shape of an arc. The total displacement of the actuator out of the plane of the metal strips is much greater than the individual expansion of the metallic elements. To maximize the bending of the actuator, metals or alloys with greatly differing CTE's are normally selected. The metal having the largest thermal expansivity is known as the 'active element', while the metal having the smaller CTE is known as the 'passive element'. For maximum actuation the passive element has to be the one with the least amount of expansion coefficient (best known is Invar- an iron-nickel alloy). The active element is then chosen to have maximum thermal expansivity given the constraints of operating environment and costs.

To maximize the actuation of the bimetallic element, a third metallic layer is sometimes added so as to increase both electrical and thermal conductivity of the actuator. This is especially important where the actuator is part of an electrical circuit and needs to pass current in addition to being a temperature sensor.

2.3 APPLICATIONS OF THE BIMETALLIC EFFECT

Bimetallic strips are found in a variety of applications. Some of the applications in the area of MEMS microfabrication are discussed in the following sections.

Reithmuller and Benecke (1988) fabricated, electro-thermally actuated structures using gold and silicon to obtain monolithic **micro-cantilevers**. These cantilevers deflected out of plane in a bimetallic strip-like manner when a voltage was applied across them.

Takeshima and Fujita (1991) used this idea to build polyimide **bimorph actuators** for a ciliary motion system. Guckel et al. (1992) pioneered thermomagnetically actuated compliant metal flexure actuators which deflected in the plane of the substrate.

Chu and Mehregany (1994) demonstrated **micro-fabricated tweezers** with a large gripping force and a wide range of motion. Sun et. al (1998) fabricated a bi-stable micro relay based on surface micro-machined multi-morph cantilever actuator. The device used a two-segment multi-morph cantilever actuator, a combination of two independently actuated recurve segments. These elements had two stable latching states, “ON” and “OFF”. Most of the above work used a laminated composite of materials with differing thermal expansion coefficients. Uniform heating of this laminate gave rise to thermoelastic actuation.

Thermostatic valves are a means of measuring the temperature and controlling heating and cooling in industrial applications. New applications of bimetallic beams are in the area of micro-actuators and microsensors. Their use can extend from temperature measuring to temperature controlling devices. Actuators have been successfully used for controlling gas flow rates from 0.1 to 600 standard cm³ per minute with pressures ranging from 5 psi to 200 psi (Jerman and Terry, 1997)

AFM (Atomic force microscopes): One way of achieving greater thermal sensitivity is by using micromechanical bimetallic cantilevers developed by Barnes and Stephenson (1994) to measure deflection (Figure 2.3). Precise measurement at the free end was made using atomic force microscope (AFM). Therefore it can be used to measure temperature, heat, and power in the range of 10^{-5} K, 150 f J, or 100 pW, respectively.

Scanning force microscopy has been given a new approach by Jung and Choi in 1999. The bimetallic beams are made of SiO_2 or Si_3N_4 coated with films of around 100 nm Al and 20 nm of Pt. The cantilever beam acts as a thermal probe. The bimetallic beam is heated with tetradecanal placed on the beam. Tetradecanal undergoes an endothermic reaction at ~ 313 K; at this temperature the deflection of the beam can be observed and the amount of tetradecanal calibrated.



Figure 2.3: Thermal actuator made of silicon (w-5 μm) and aluminum (w-2 μm) (Barnes and Stephenson; 1994)

If the reaction is endothermic the heat is absorbed and the nano-sized bimetallic beam deflects upward, whereas an exothermic reaction bends the bimetallic beam in the downward direction. This way the chemical can be easily identified based on the deflection of the beam. This nano-sized bimetallic element can also be used to measure the weight of the given chemical. The maximum deflection achieved with tetradecanal on the bimetallic beam was 40 μm at 313 K.

Bi-layered cantilevers can be used to calibrate the CTE of silicon. Silicon and SiO_2 formed the two layers of the composite beam. An experimental apparatus was designed to measure the deflection and measure the thermal expansion. The beam was designed by Tada and Nieva (1999) (Figure 2.4) in a way such that it was independent of the thermomechanical properties of silicon dioxide. The deflection produced was a direct function of only the properties of the Si. The CTE values were measured in the range from 25°C to 1000°C.

Thermal deflections are produced in polycrystalline silicon at CMOS compatible driving voltages. These deflections were accounted to the distinctive property of thermal conductivity and resistivity of the material. Silversmith and Reid (1998) extended the Joule

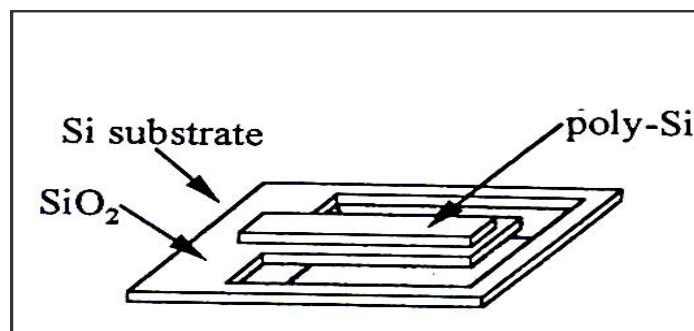


Figure 2.4: Bi-layered cantilever beam (Tada and Nieva, 1999).

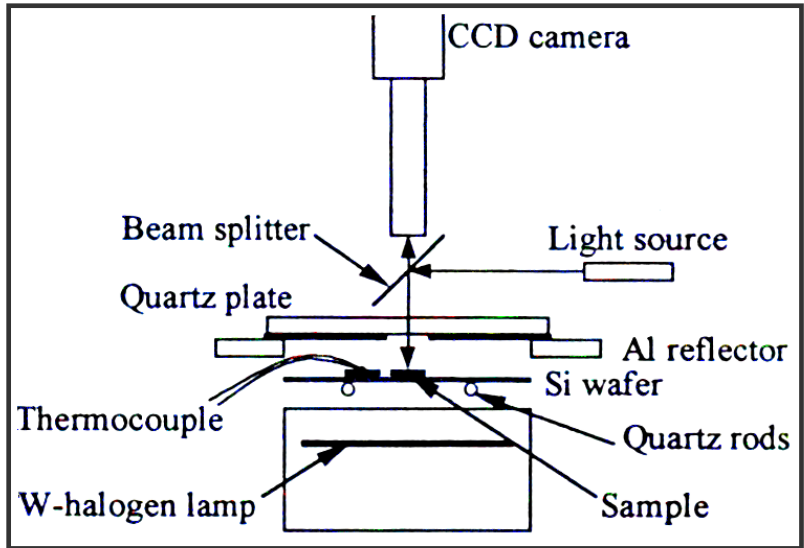


Figure 2.5: Experimental apparatus to measure CTE of Si (Tada and Nieva, 1999).

heating FEM model as the design principle to account for the intrinsic losses from the thermal conduction and temperature variation effects.

Thermal actuators were used in the bimorph structure by Sehr and Evans (2001) to produce deflections in the plane of the wafer (Figure 2.6). Current was passed through the beam and the power calculated based on the voltage reading across contact pads. Aluminum and silicon structures made up the bimetallic strips. For a bimorph of 1000 μm a center displacement of 4.5 μm was achieved with an input power of 3mW.

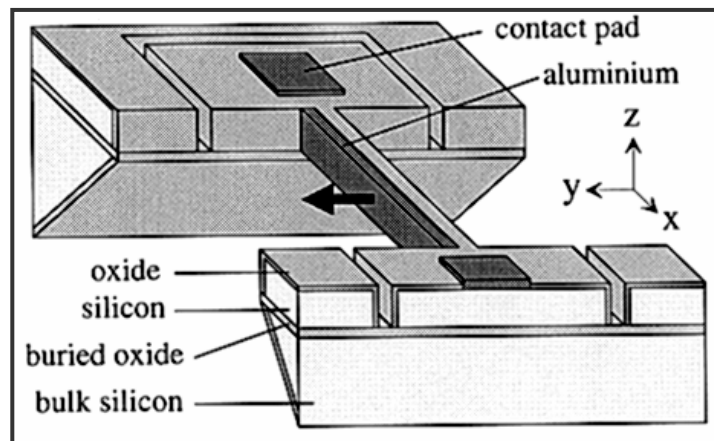


Figure 2.6: Vertical basic recurve actuator (Sehr and Evans, 2001).

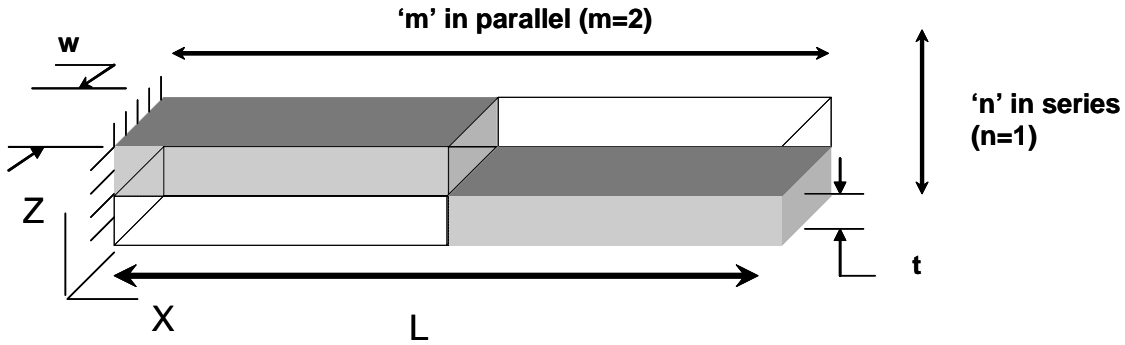


Figure 2.7: Basic building block for the recurve architecture.

The **recurve architecture** consists of an array of bimetallic beams in a series and/or parallel combination. Bimorph elements stacked in such a recurve architecture were used to produce deflection by Ervin and Brei (1998). Al and PVDF were used as the bimorph elements. Recurve arrays were arranged in series and parallel combinations to increase the net deflection and force, respectively. The maximum deflection obtained was 1.2 mm. Structuring of the bimetallic beams in parallel increases the net force and adding in series increases the net displacement. This architecture can be structured based on the desired deflection, force and volume constraints.

The basic building block was the recurve element shown in Figure 2.7. Elements were added, ' m ' in parallel and ' n ' in series, based on the required force or displacement thus increasing the displacement on mechanical elements.

The recurve principle was later applied to a bimetallic **thermomechanical recurve** pattern by Datta (2001; Datta et al. (2003)). The idea was to use nickel and Invar as the bimetallic elements, in the recurve architecture. The fabrication process was not successful, mainly due to the set backs in the plating of Invar. The alignment process during X-ray exposure had to be improved to reduce the errors.

3. ANALYTICAL MODELING AND NUMERICAL SIMULATIONS (BIMETALLIC BEAMS AND GOVERNING BOUNDARY CONDITIONS)

3.1 INTRODUCTION

- **Design Specifications/Requirements**

In order to design and microfabricate a temperature sensor for downhole use, it needed to survive temperatures to a maximum of 300°C. The initial aim was to use the existing recurve configuration to produce bimorph structures and to validate the mathematical models to extend the application of a thermal actuator to a sensor.

In order to measure the temperature change, a bimetallic beam approach was used. The foundation of the project was the thermal recurve actuator based on bimetallic effect (Datta, 2001). It was proposed to electroplate nickel and Invar as bimetallic elements. Datta adapted the recurve architecture from Ervin and Brei (1998). They proved that the free deflection of a recurve array was the sum of the deflections of each of the individual recurve elements. This could be modified to suit the requirements of force and deflection.

- **Performance Evaluation**

In the first generation approach for fabrication of a thermal recurve actuator, there were no limitations on the force produced. It was decided to adopt the previous design of the recurve array to fabricate the sensor and calibrate the deflections produced. In the first generation process the recurve arrays suffered from poor adhesion between the two bimetallic elements. The electroplated Invar was found to be brittle and would disintegrate upon etching of the resist. Two main areas were identified that needed correction: electrodeposition of Invar and improvements of the fabrication process so as to

reduce the errors during X-ray exposures and other associated handling and machine errors .

- **Proposed Design**

The recurve array pattern was a bimorph in its simplest form. Both the components must be plated side by side with good contact. Alignment of the pattern was assigned as the primary goal. The mask design of the recurve array architecture, laid out by Datta (Figure 3.1), was adopted. The optical mask consisted of 12 arrays of recurve elements. There were 6 sets of arrays with lengths of the recurve as 8000 μm , 12000 μm and 16000 μm , with widths 100 μm and 200 μm (refer to Table 3.1). All 12 arrays were to be fabricated to a height of 500 μm . An X-ray mask was built from this optical mask. A modified X-ray mask was fabricated in the second generation process to reduce the errors. The details of the modified fabrication process and its justification in the successful release of the recurve structures are listed in Chapter 4.

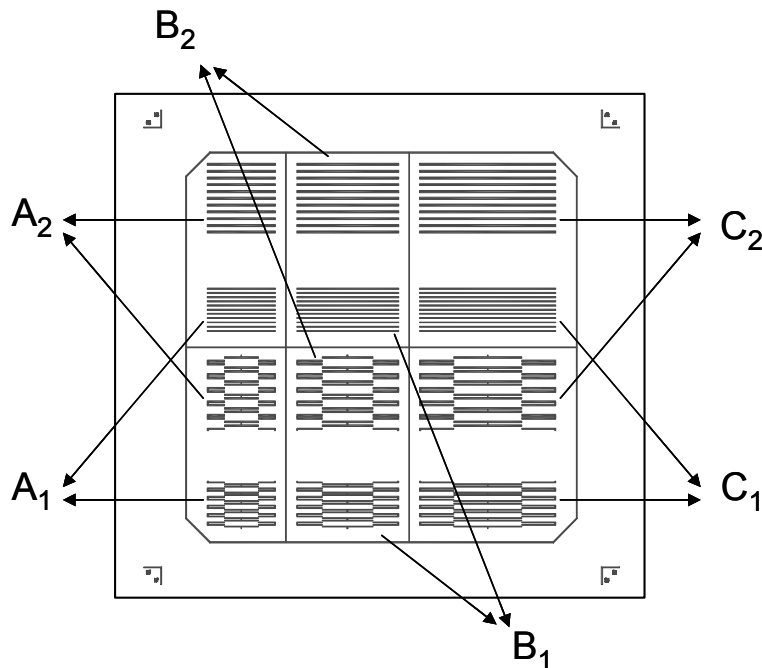


Figure 3.1: Optical mask patterns for recurve array architecture (Datta, 2001). See Table 3.1 for design dimensions.

Table 3.1: Dimensions of the three sets of recurve array.

No.	Length(μm)	Width(μm)	Height(μm)
A ₁	8000	100	500
A ₂	8000	200	500
B ₁	12000	100	500
B ₂	12000	200	500
C ₁	16000	100	500
C ₂	16000	200	500

The length, breadth and height of the recurve elements of the recurve were taken as the input parameters for the analytical and numerical models. These simulations were performed to predict the performance of the bimorphs. Analytical models were developed from the static equations governing the deflection produced due to temperature rise. The following sections give the various equations formulated to calculate the deflection, the blocking force, and the stress produced. Self-weight analysis was performed and it revealed that the recurve elements were able to support the array structure and not buckle under their own weight. The time constant was also determined.

3.2 ANALYTICAL MODELING

3.2.1 LINEAR BIMETALLIC BEAM

A bimetallic strip consists of two different metals bonded along the length of the beam. Timoshenko (1925) was the first to study stresses in bimaterial beams. He used elementary beam theory to obtain an expression for the curvature of a bimetallic beam due to a uniform temperature change. Figure 3.2 shows a schematic of a bimetallic beam. The general expression for the radius of curvature of a cantilever beam of unit width heated from temperature T_0 to T in absence of external forces (Timoshenko, 1953) is:

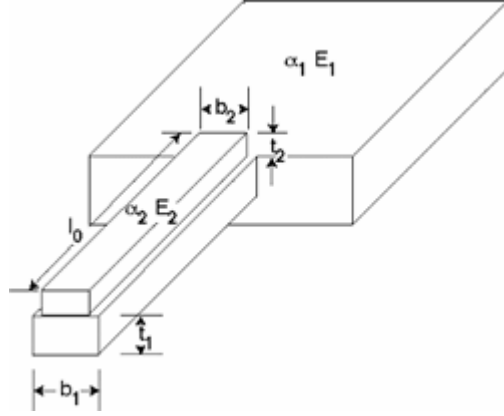


Figure 3.2: Schematic of a bimetallic beam (Chu, et al, 1993)

$$\frac{1}{R} - \frac{1}{R_0} = \frac{6(1+p)^2(\alpha_2 - \alpha_1)(T - T_0)}{t[3(1+p)^2 + (1+pq)(p^2 + \frac{1}{pq})]} \quad (1)$$

where

$$\frac{1}{R_0} = \text{Initial curvature of the strip at temperature at } T_0 \text{ (}\mu\text{m}^{-1}\text{)}$$

α_1 and α_2 are the CTE of low and high expansion materials ($\mu\text{m/m} \times 10^{-6}/^\circ\text{C}$)

$q = \frac{E_1}{E_2}$ where E_1 and E_2 are the Young's moduli of the two materials

$p = \frac{t_1}{t_2}$, with t_1 and t_2 the thickness of the bimorph layers

$t = t_1 + t_2$, the total thickness of the strip (μm)

3.2.1.1 FOR A BIMETALLIC BEAM SIMPLY SUPPORTED AT BOTH ENDS

A simply supported bimetallic beam is shown in Figure 3.3. Equation 1 can be extended for both simply-supported and cantilever beams. This equation determines the deflection produced from the value of the curvature obtained. Consider the deflection produced by a bimetallic beam simply supported at both ends. The initial curvature is

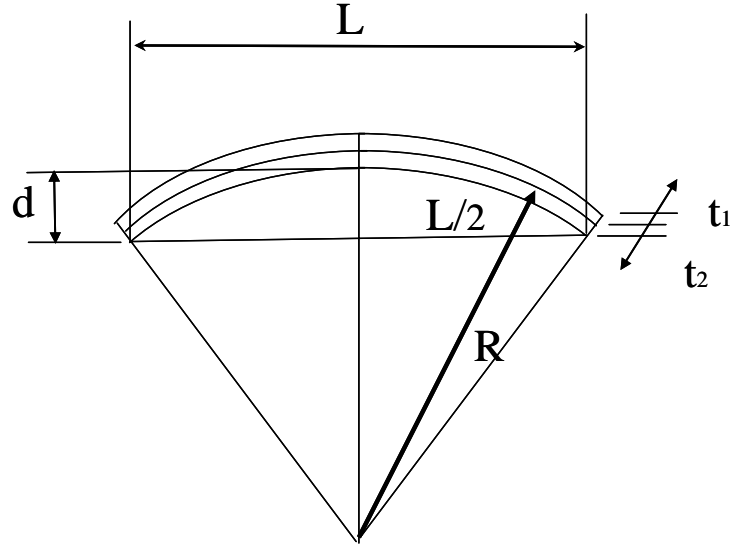


Figure 3.3: Simply supported bi-metallic beam.

considered to be zero ($\frac{1}{R_0} = 0$). The internal forces and moments induce bending in the bimetallic beam with an ideal stress distribution. The deflection at the mid point can be given as (Timoshenko, 1955):

$$(R - t_2)^2 = (R - d - t_2)^2 + \left(\frac{L}{2}\right)^2 \quad (2)$$

The radius of curvature after deflection:

$$\frac{1}{R} = \frac{8d}{L^2 + 4d^2 + 8dt_2} \quad (3)$$

Assuming that the deflection and the thickness are less than 10% of its length, $8dt_2$ and $4d^2$ can be neglected giving

$$d = \frac{L^2}{8R} \quad (4)$$

Then from Equation (1)

$$d = L^2 \frac{3(1+p)^2}{4t \left[3(1+p)^2 + \left(1+pq\right)\left(p^2 + \frac{1}{pq}\right) \right]} (\alpha_2 - \alpha_1)(T - T_0) \quad (5)$$

Equation (5) defines a relationship between the deflection produced to the length and the temperature change. In this parametric equation, the values of p and q can be changed to obtain specific deflections for desired applications.

3.2.1.2 FOR A BIMETALLIC CANTILEVER STRIP

The deflection produced at the free end of a cantilever beam can be calculated. Based on the geometry of the beam when deflected (Figure 3.4):

$$(R + t_1)^2 = (R + t_1 - d)^2 + L^2 \quad (6)$$

Rearranging,

$$\frac{1}{R} = \frac{2d}{L^2 + d^2 - 2dt_1} \quad (7)$$

If $d^2 \ll L^2$ and $t_1 \ll L^2$, then the deflection of the free end is given by:

$$d = \frac{L^2}{2R} \quad (8)$$

The final equation is:

$$d = L^2 \frac{3(1 + p^2)}{t \left[3(1 + p^2) + (1 + pq) \left(p^2 + \frac{1}{pq} \right) \right]} (\alpha_2 - \alpha_1)(T - T_0) \quad (9)$$

The magnitude of the ratio of $q = E_1/E_2$ has no substantial effect on the curvature of the strip; taking $q=1$, the error is less than 3%. The radius of curvature then reduces to:

$$\frac{1}{R} = \frac{6p}{t(p+1)^2} (\alpha_2 - \alpha_1)(T - T_0) \quad (10)$$

If the thickness of the two strips is the same ($p=1$):

$$\frac{1}{R} = \frac{3}{2} \frac{(\alpha_2 - \alpha_1)(T - T_0)}{t} \quad (11)$$

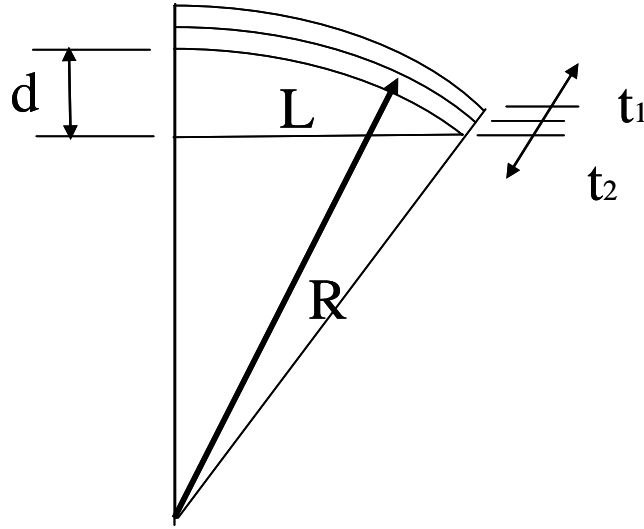


Figure 3.4: Bi-metallic cantilever beam.

Introducing the constant, $k = \frac{3}{2}(\alpha_2 - \alpha_1)$, called the flexivity²,

Equation (11) becomes:

$$k = \frac{\frac{t}{R}}{T - T_0}; \quad (12)$$

Flexivity can be defined as the change of curvature of a bimetallic strip for the product ($\Delta T * t$). Using the Equation (11) for curvature and substituting $q=1$;

$$d = \frac{k L^2}{2 t} (T - T_0); \quad (13)$$

Based on Equation (13), the free deflection of a cantilever produced at the end point is directly proportional to the difference in temperature, the square of length, and inversely proportional to the thickness of the strips. The next section defines the reactions occurring in each strip as the deflection is produced due to a temperature change.

2 - ASTM Standard B-106, Standard Test Methods for Flexivity of Thermostat Metals, ASTM International, 2002.

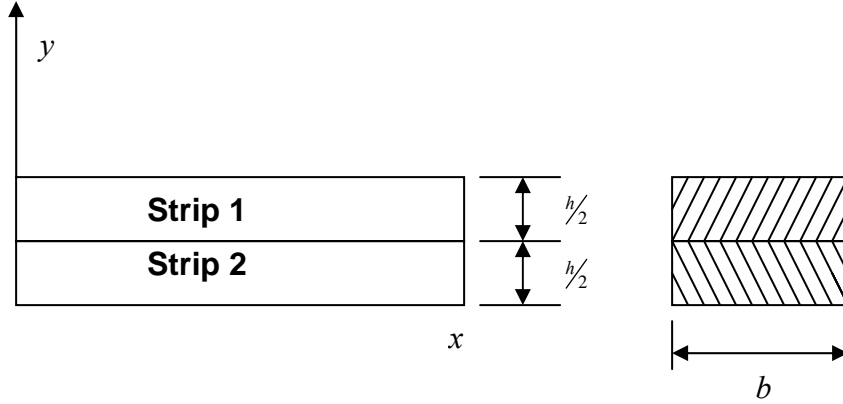


Figure 3.5: Bimetallic strip model.

3.2.2 REACTIONS AT EACH STRIP

A bimetallic beam is made of two different materials with different CTE's (see Figure 3.5). Let the CTE of the two materials be α_1 and α_2 , and the moduli of elasticity be E_1 and E_2 , respectively.

An increase in temperature causes the two metal strips to expand. The bimetallic beam bends with the metal of lower CTE on its concave side. Figure 3.6 shows the force P and the moment ($Ph/4$) at the cross-section of each strip.

The axial strains acting on the beams are given by Equation (14) and (15).

$$\varepsilon_1(y) = \alpha_1 T + \frac{2P}{E_1 h b} - \frac{1}{\rho_1} \left(y - \frac{h}{4} \right) \quad (14)$$

$$\varepsilon_2(y) = \alpha_2 T + \frac{2P}{E_2 h b} - \frac{1}{\rho_2} \left(y + \frac{h}{4} \right) \quad (15)$$

where ρ_1 and ρ_2 represent the radii of curvature of the strip. Solving for ρ_1 and ρ_2 ,

yields Equations (16) and (17):

$$\frac{1}{\rho_1} = \frac{M_1}{E_1 I} = \frac{24P}{E_1 h^2 b} \quad (16)$$

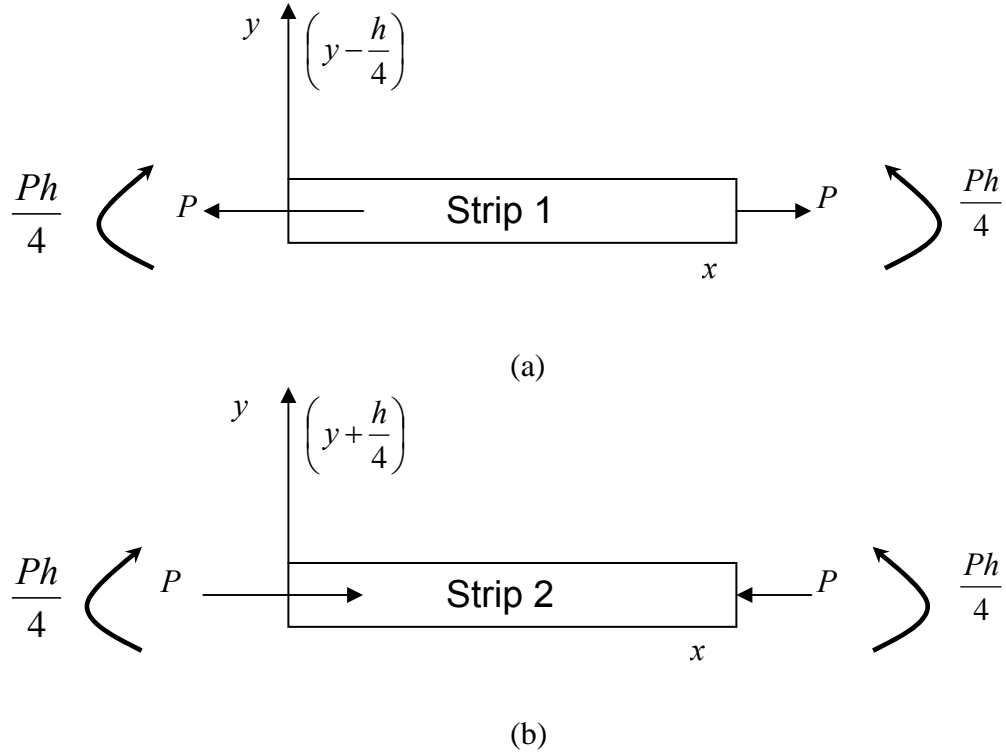


Figure 3.6: Reactions for (a) Strip 1 (b) Strip 2.

$$\frac{1}{\rho_2} = \frac{M_2}{E_2 I} = \frac{24P}{E_2 h^2} b \quad (17)$$

Continuity requires that the strains must be equal at the interface, $y = 0$; this can be expressed as in Equation (18):

$$\alpha_1 T + \frac{2P}{E_1 h b} + \frac{h}{4\rho_1} = \alpha_2 T - \frac{2P}{E_2 h b} - \frac{h}{4\rho_2} \quad (18)$$

Substituting ρ_1 and ρ_2 into Equation (18) the force, P , is produced (in Equation (19))

$$P = \frac{(\alpha_2 - \alpha_1) T}{8} \frac{h b}{\left(\frac{1}{E_1} + \frac{1}{E_2} \right)} \quad (19)$$

Substituting this into Equations (16) and (17) gives expressions for the curvature of the beams as a function of CTE (Equation (20)).

$$\frac{1}{\rho_1} = \frac{3(\alpha_2 - \alpha_1)T}{\left(1 + \frac{E_1}{E_2}\right)h} ; \quad \frac{1}{\rho_2} = \frac{3(\alpha_2 - \alpha_1)T}{\left(1 + \frac{E_2}{E_1}\right)h} \quad (20)$$

The total moment of the bimetallic beam is defined as Equation (21) (t_1 and t_2 are the thickness of the strip 1 and 2).

$$M = M_1 + M_2 = P((t_1 + t_2)/2) \quad (21)$$

Substituting for P from (19), the combined moment, M , is obtained (Equation (22))

$$M = \frac{(\alpha_2 - \alpha_1)T}{8} \frac{hb}{\left(\frac{1}{E_1} + \frac{1}{E_2}\right)} ((t_1 + t_2)/2) \quad (22)$$

3.2.3 MODELING RECURVE ARCHITECTURE

The approach used for the bimetallic beam (Figures 3.6(a) and (b)) can be extended for a recurve structure. The basic building block for the recurve architecture is shown in Figure 2.7. A quasi-static model of the recurve architecture based on applying Castigliano's second theorem to the recurve element is shown in Figure 3.7. The total moment acting on the beam is the sum of the internal moment, external moment, and the moment due to any applied force, F , acting at the end of the beam (Equation (23)).

$$M = F_j(L - x) + M_{oj} + M_{eh} \quad (23)$$

$$M_{eh} = \int_A \sigma_m z dA \quad (24)$$

where M_{eh} is the internal moment (from Figure 3.7 , $M_1 = -M_2$).

For the recurve element the quasi-static force – deflection is:

$$\Delta_{zj} = \frac{F_j L^3}{3D} + \frac{M_{oj} L^2}{2D} + \frac{3M_1 L^2}{8D} + \frac{M_2 L^2}{8D} \quad (25)$$

and

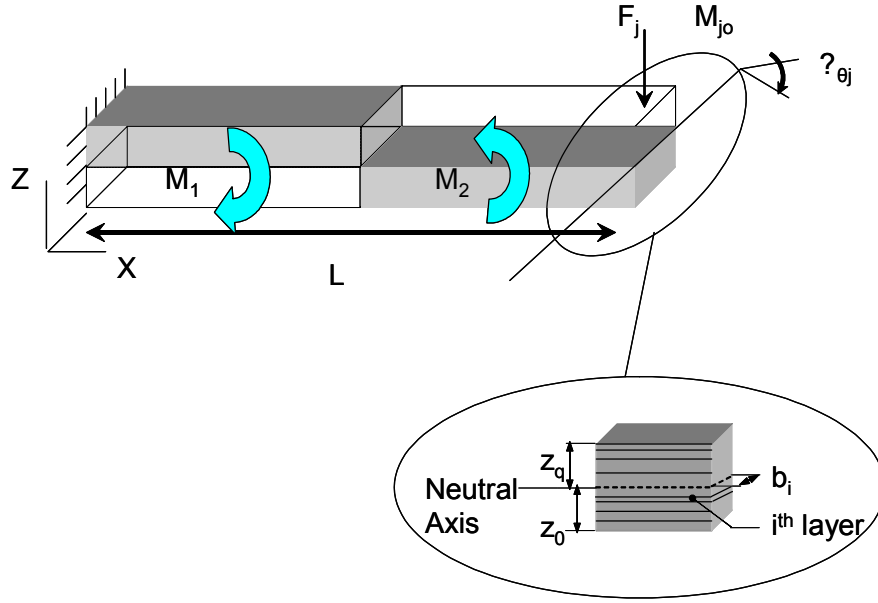


Figure 3.7: Recurve element and its cross-section (Ervin and Brei, 1998).

$$\Delta_{\theta_j} = \frac{F_j L^2}{2D} + \frac{M_{oj} L}{D} + \frac{M_1 L}{2D} + \frac{M_2 L}{2D} \quad (26)$$

$$\text{where } D = \sum_{q\text{-layers}} Y_i b_i \left(\frac{z_i^3 - z_{i-1}^3}{3} \right) \quad (27)$$

is the composite stiffness.

For a bimetallic beam with thicknesses t_1 and t_2 ,

$$D = \frac{b}{3} (E_1 t_1^3 + E_2 t_2^3) \quad (28)$$

For $t_1=t_2$ this reduces to:

$$D = \frac{b}{3} (E_1 + E_2) t^3; \quad (29)$$

For a recurve array member the elements are built up by adding 'm' in series and 'n' in parallel. The total force applied in a series element:

$$F_{\text{total}} = F/m \quad (30)$$

The force-deflection relationship is given in Equation (31):

$$\Delta_z = n \left[\frac{F_j L^3}{3D} + \frac{M_o L^2}{2D} + \frac{ML^2}{4D} \right] \quad (31)$$

and the simplified rotation model (Equation (26)) gives:

$$\Delta_\theta = n \left[\frac{F_j L^2}{2D} + \frac{M_{oj} L}{D} \right] \quad (32)$$

In modeling the recurve architecture two main assumptions were made. The tip rotation for each member was taken as zero, since the array members were loaded and assembled symmetrically. Moments produced in series elements cancelled each other. This provided for a balance of the forces applied to each member. The array was assumed to be homogenous at all connections for any external load, F_j .

Equating Equation (32) to zero,

$$\frac{\Delta_z}{n} = \frac{F}{m} \frac{L^3}{12D} + \frac{ML^2}{4D} \quad (33)$$

The moment, M , is the total moment applied in the bimetallic beam. Substituting the expression for M from Equation, (22):

$$\frac{\Delta_z}{n} = \frac{F}{m} \frac{L^3}{12D} + \frac{L^2}{4D} \left[\frac{(\alpha_2 - \alpha_1) T}{8} \frac{hb}{\left(\frac{1}{E_1} + \frac{1}{E_2} \right)} ((t_1 + t_2)/2) \right] \quad (34)$$

If the thickness of both the beams is the same (i.e. $t_1=t_2$):

$$\frac{\Delta_z}{n} = \frac{F}{m} \frac{L^3}{12D} + \frac{L^2}{4D} \left[\frac{(\alpha_2 - \alpha_1) T}{8} \frac{hbt}{\left(\frac{1}{E_1} + \frac{1}{E_2} \right)} \right] \quad (35)$$

For free deflection; (substituting blocking force, F in Equation (35), to zero):

$$\Delta_z = \frac{nL^2}{4D} \left[\frac{(\alpha_2 - \alpha_1) T}{8} \frac{hbt}{\left(\frac{1}{E_1} + \frac{1}{E_2} \right)} \right] \quad (36)$$

For the blocking force, the free deflection term was set to zero:

$$F = \frac{3m}{L} \left[\frac{(\alpha_2 - \alpha_1) T}{8} \frac{hbt}{\left(\frac{1}{E_1} + \frac{1}{E_2} \right)} \right] \quad (37)$$

and the maximum stress produced is :

$$\sigma_{\max} = \frac{2F}{bh} + \frac{h E_1}{4 r} = \frac{2}{bh} \frac{3m}{L} \left[\frac{(\alpha_2 - \alpha_1) T}{8} \frac{hbt}{\left(\frac{1}{E_1} + \frac{1}{E_2} \right)} \right] + \frac{h E_1}{4 r} \quad (38)$$

For a cantilever beam element, the total moment equals the sum of the moments of the two strips. Both of the moments act throughout the beam. Recurve architecture is different from the traditional cantilever element. For example, if in the case of a recurve element, where the moments distributed in an equal and opposite manner, are in the x - y plane, in the traditional bimetallic beam they are in the y - z plane. A recurve array member produces more blocking force than deflection as compared to the traditional cantilever beam. These arrays can be easily tailored according to the force and deflection requirements.

3.3 ANALYTICAL AND NUMERICAL SOLUTION

Based on the recurve analytical models, the free deflection (Equation (36)) and blocking force (Equation 37) were plotted. The thermomechanical properties of nickel

and Invar were obtained from the bulk properties (Appendix B gives a list of these properties). Deflection of a single recurve element was obtained for various lengths and changes in temperature. The different values for length, width and height were selected from the work done in the previous thesis (Datta, 2001). The value of deflection as a function of temperature for each different length of the beam would help in parametric design.

3.3.1 FREE DEFLECTION

The analytical equations obtained in the previous section for deflection based on length and temperatures of the beam were solved. These represent the calculations done for the basic bimorph architecture ($m=2$ and $n=1$) (refer to Figure 2.7). Parametric relationships were established based on the free deflection (Equation (36)). For a particular value of length, a value of deflection was obtained at a given difference in temperature. Figure 3.8 shows the combined relationship between bimorph length and temperature versus the free deflection produced.

The relative temperature was plotted as ΔT . The reference temperature was set to 25°C and the maximum temperature was set to the maximum governing temperature of 500°C. As the length of beam was increased, the deflection produced due to temperature increased in a parabolic curve. The plot shows a linear relationship between the rise in temperature and the free deflection. For a bimorph beam of length 8000 μm , a temperature of 300°C produced a deflection of 80.45 μm . From the graph, the deflection for any length of the bimetallic beam at the given temperature can be obtained.

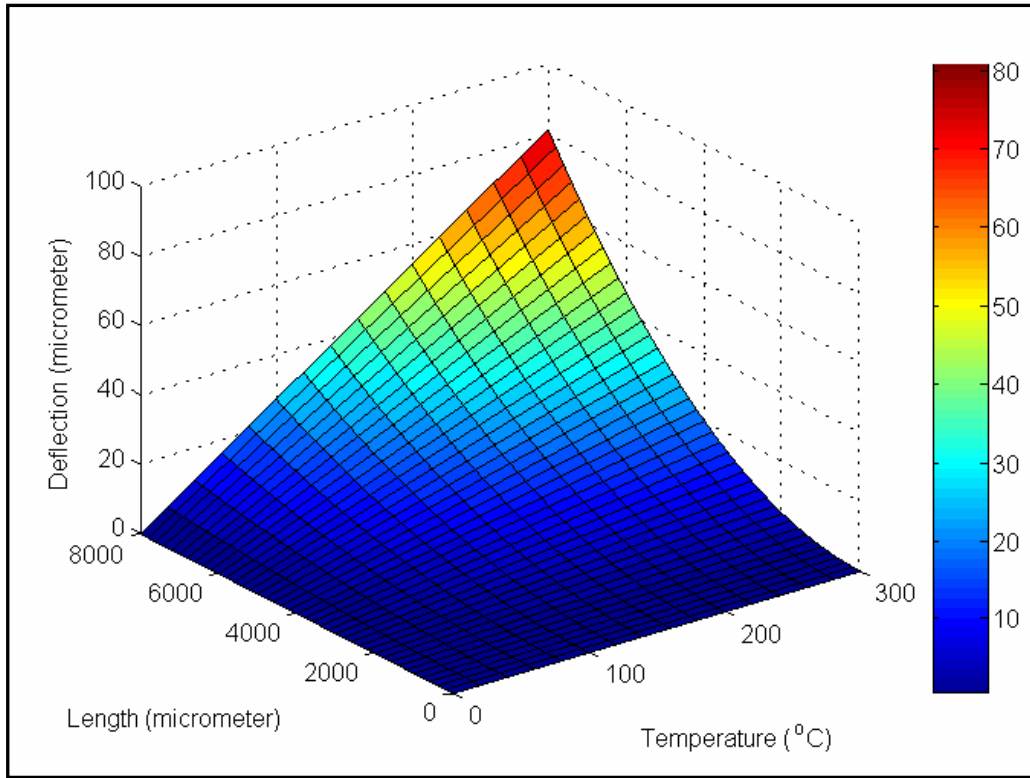


Figure 3.8: Deflection with change in length and temperature ($w=100\ \mu\text{m}$, $h=500\ \mu\text{m}$, $m=2$ and $n=1$).

3.3.2 BLOCKING FORCE

Equation (37) gives the blocking force, which is inversely proportional to the length of the beam. Simply stated, the blocking force is the amount of force required to prevent the recurve from deflecting due to a thermal gradient. Figures 3.9 and 3.10 show the variation of blocking force with length at 300°C and 500°C . The length of the beam plotted against the blocking force is a parabolic curve as seen in the Figures 3.9 and 3.10.

From the plots, it is evident that a significant change in the value of blocking force occurs as the beam is lengthened from 0 to $1000\ \mu\text{m}$. The incremental change in the blocking force decreases with an increase in the beam length beyond $1000\ \mu\text{m}$. This is due to the quadratic dependence on the length of the beam.

For a beam of length 8000 μm , when the temperature is increased to 300°C, the blocking force is 0.2 N and when the temperature is further increased to 500°C, the blocking increases to 0.33 N (from Figures 3.9(b) and 3.10(b)).

These graphs provide insight into selection of an optimum length of the bimetallic beam which is an important design parameter. They show that minimal change in the blocking force occurs with significant changes in the beam span for lengths of beam ranging from 2000 μm to 8000 μm , whereas for range 0 to 2000 μm , there is a significant variation in the value of blocking force.

- **Finite Element Modeling**

ANSYS (Version 5.7, ANSYS, Inc., Canonsburg PA) was used for finite element modeling of the recurve beam. Simulations were run to determine the quasi-static deflection produced with an increase in temperature.

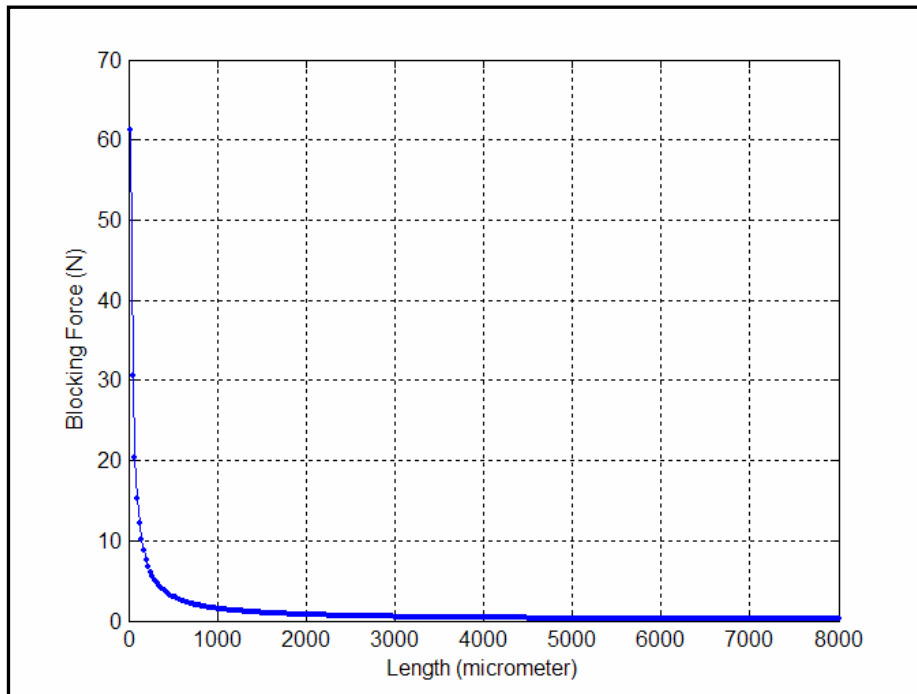


Figure 3.9(a): Blocking Force vs. Length at a temperature of 300°C ($l=8000 \mu\text{m}$, $w=100 \mu\text{m}$, $h = 500 \mu\text{m}$, $m=2$ and $n=1$).

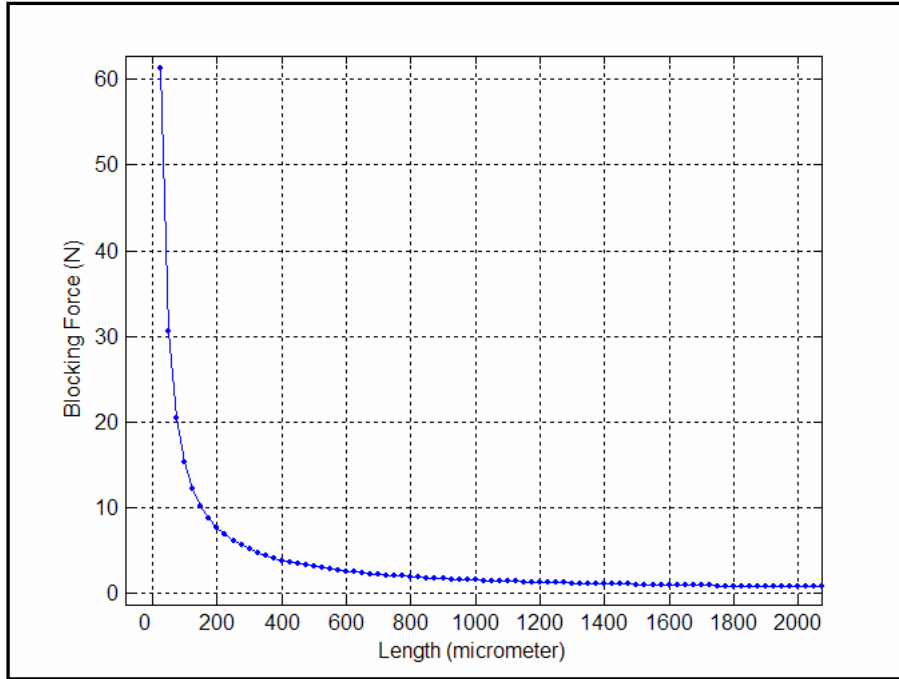


Figure 3.9(b): Zoom of 3.9 (a).

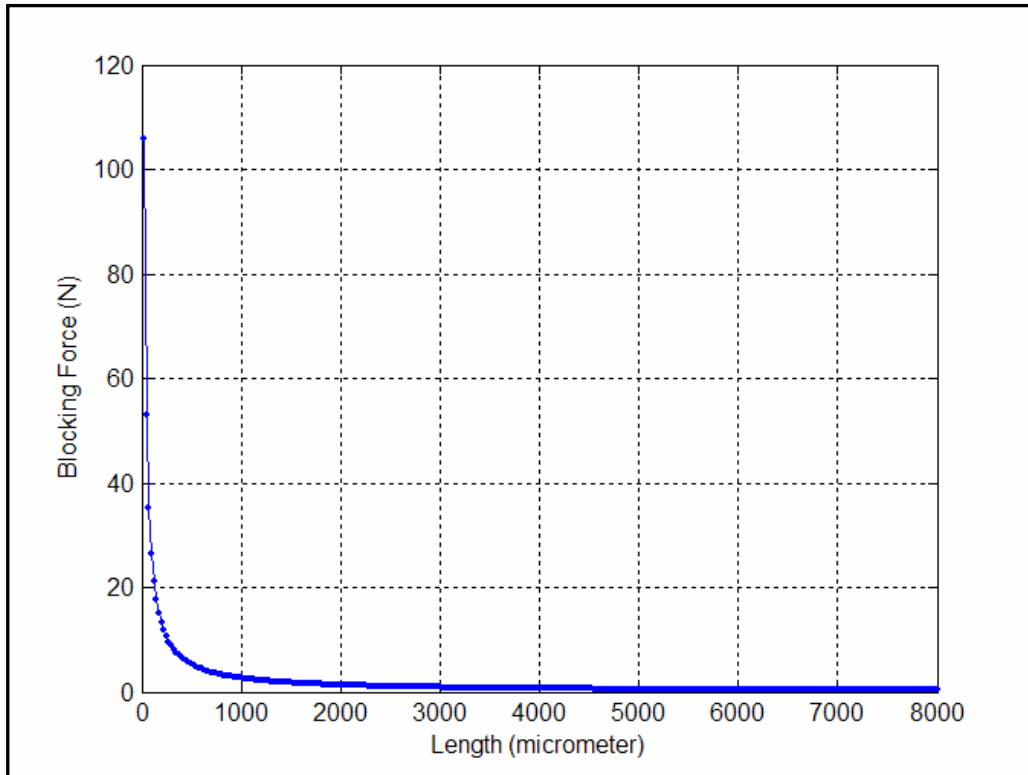


Figure 3.10(a): Blocking Force vs. Length at a temperature of 500°C ($l=8000 \mu\text{m}$, $w=100 \mu\text{m}$, $h = 500 \mu\text{m}$, $m=2$ and $n=1$).

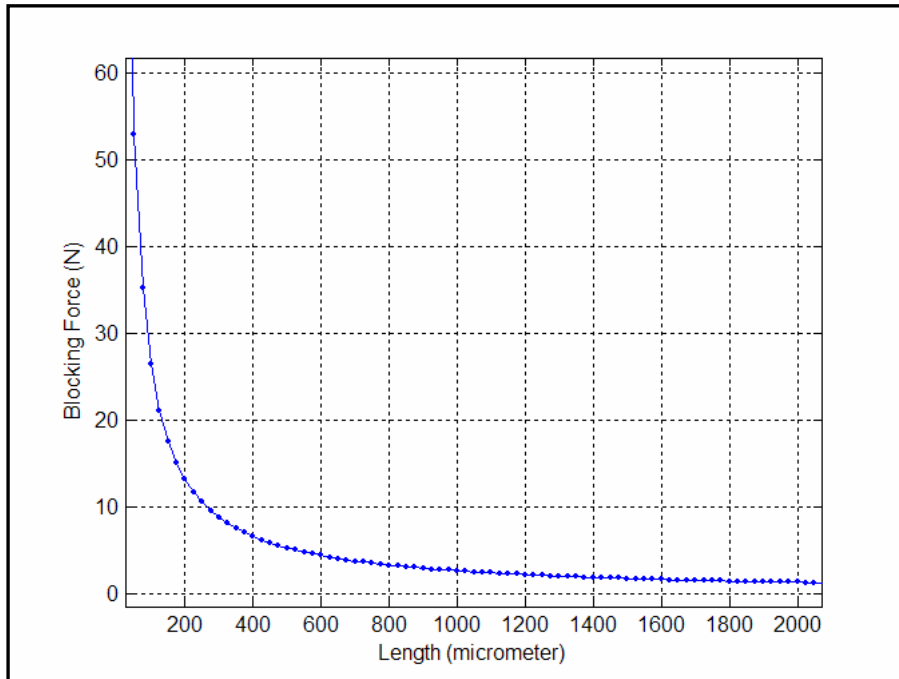


Figure 3.10(b): Zoom of 3.10(a).

3.3.3 SELF-WEIGHT ANALYSIS

The self-weight analysis was performed to determine whether the bimetallic array could support its own weight. The microfabrication process ends by etching the bimetallic array structure out of the resist. It was imperative that it maintain its structural integrity upon release and did not collapse under its own weight.

To calculate the out-of-plane deflection (Z axis) produced due to self-weight an array of 11 recurve elements was built up. To simulate the model three main types of solid elements were considered; Brick 8-node, 20-node and Solid 187. Solid 187 (10-node elements) were found to accommodate both the structural and thermal properties. The basic structure was repeated eleven times to get the complete array with $m=2$ (number of elements in series) and $n=11$ (number of elements in parallel) as shown in Figure 3.11. The two base end connectors were constrained in all the axes. Gravitational force was

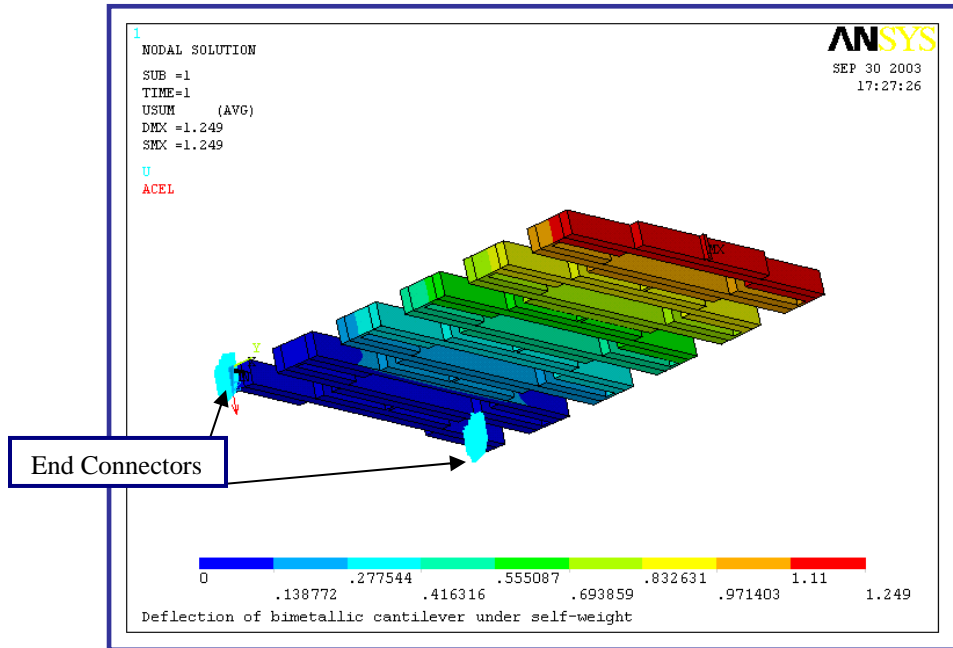


Figure 3.11: Deflection of recurve array due to self-weight ($l=8000 \mu\text{m}$, $w=100 \mu\text{m}$, $h = 500 \mu\text{m}$, $m=2$ and $n=11$).

applied to the entire structure. The maximum end point deflection obtained was $1.249 \mu\text{m}$ at room temperature.

3.3.4 THERMAL DEFLECTION

A single recurve element was modeled to calculate the thermal deflection. The basic element member with $m=2$ and $n=1$ was used with two end connectors (see Figure 3.12). The volume surrounding the recurve element was considered as insulated and the only source of heat input was at the base of the two connectors. In reality the recurve array would be encapsulated with only the base end connectors exposed to the heated environment. So the measurements obtained would be affected largely by conduction rather than convection.

This condition was applied based on the fact that the conduction of heat through the array was a dominant factor over the convection. Thermal modeling was performed

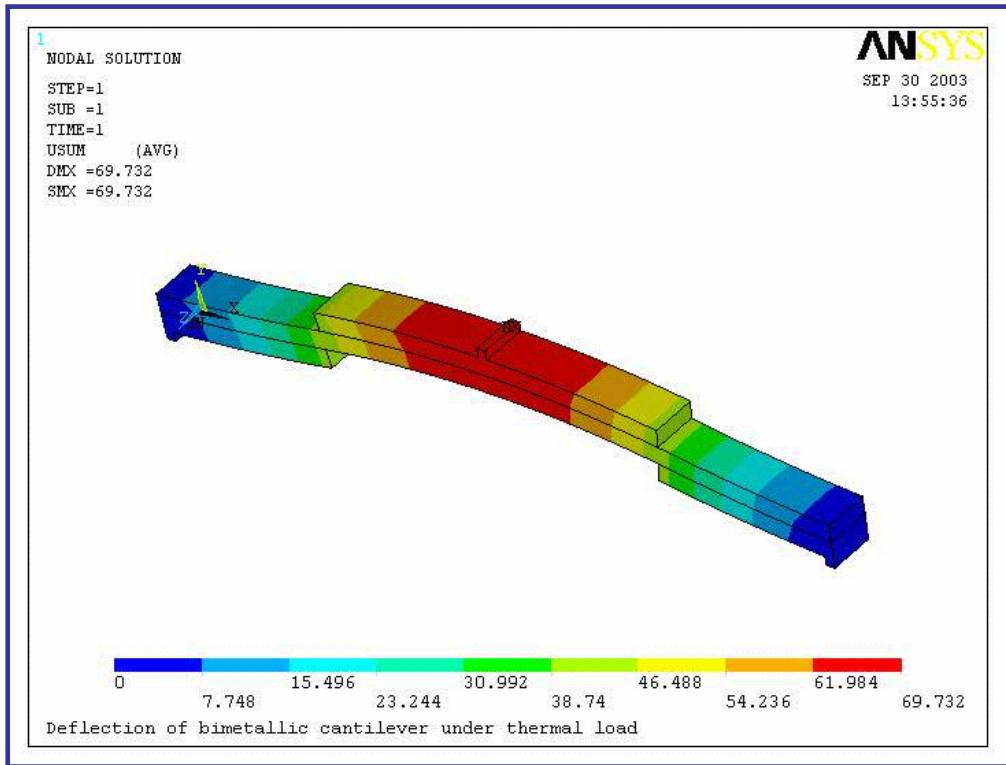


Figure 3.12: Deflection of the recurve element in micrometers at steady state temperature of 300°C ($l=8000 \mu\text{m}$, $w=100 \mu\text{m}$, $h=500 \mu\text{m}$, $m=2$ and $n=1$).

followed by mechanical force-deflection analysis. A temperature input was given to the base of the element to get an overall temperature output distribution. This was used as an input to the mechanical model for the calculation of deflection. For thermal modeling, thermal shell elements were used to get the thermal image for the recurve model. Temperature values were varied from 25°C to 300°C. The maximum deflection (in-plane) obtained for a length of 8000 μm was 69.732 μm at 300°C.

3.3.5 THERMAL STRESSES

Stresses were determined from Von Mises stress analysis. From Figure 3.13, the maximum stress concentration area was at the connectors. The maximum yield stress of electroplated nickel (810 MPa - Fritz and Leuerer, 2000) and bulk Invar were

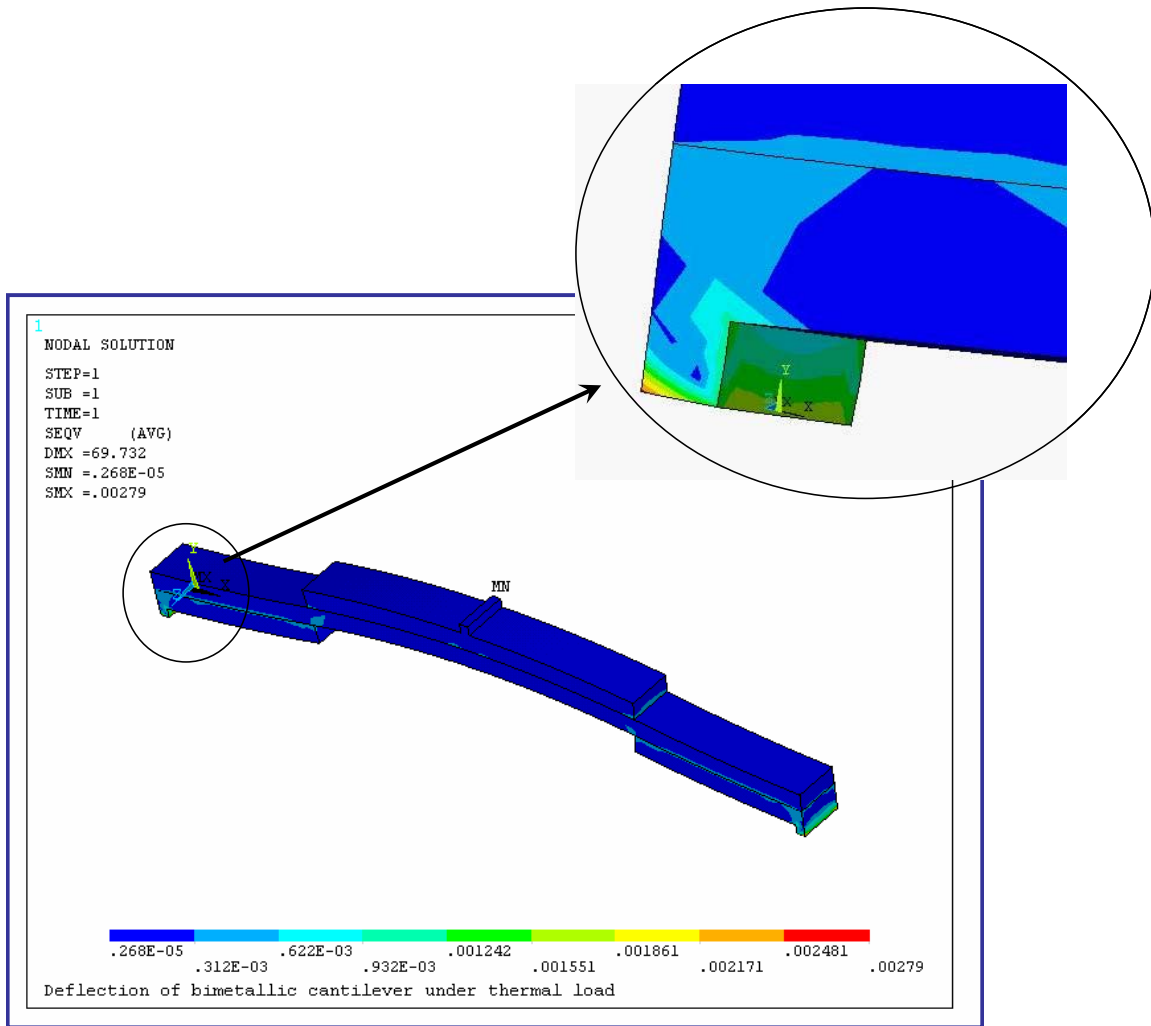


Figure 3.13: Thermal stresses produced in the recurve element at 300 °C for a deflection of 69.73 μm ($l=8000 \mu\text{m}$, $w=100 \mu\text{m}$, $h=500 \mu\text{m}$, $m=2$ and $n=1$).

significantly higher than the calculated stress values at the connections. The maximum stress obtained was 279 MPa.

3.3.6 TEMPERATURE RESPONSE

The response of a temperature sensor depends on the physical properties of the sensor and the properties of the environment. The recurve model was built and thermal

analysis was performed. The thermal results were then transferred onto the structural model. A temperature input was given at the base of the two end connectors.

The entire recurve structure was allowed to reach a steady-state temperature of 300°C. It was assumed that, at the node selected for temperature response, the temperature was uniform and that the thermomechanical properties of the system were invariant with temperature. Figure 3.14 shows the dynamic response of time versus the temperature attained by the structure.

The time constant (value obtained at 63.2% of the maximum) for the recurve bimorph was found to be 1.44 seconds. It took 7.2 seconds to attain the isothermal state of 300°C. In the model, the recurve was considered to be insulated. Heat loss to the environment

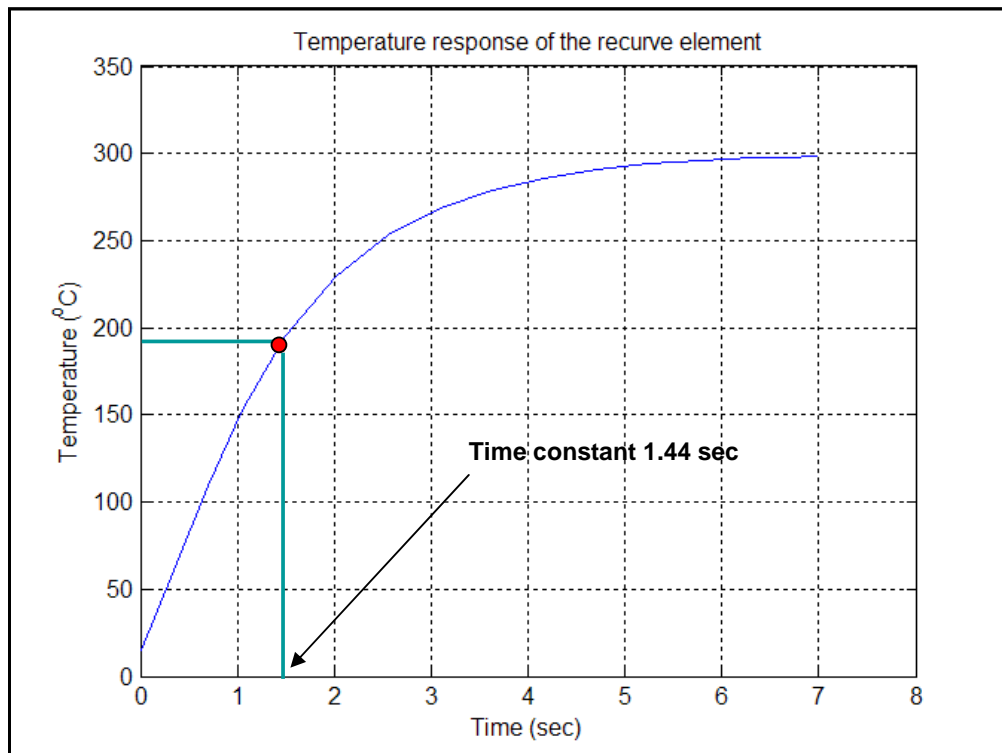


Figure 3.14: Thermal response of the basic recurve element ($l=8000 \mu\text{m}$, $w=100 \mu\text{m}$, $h=500 \mu\text{m}$, $m=2$ and $n=1$).

would increase the time constant, as convection to the environment would cause the structure to attain the maximum temperature more slowly. In order to reduce the time constant further, dimensions of the recurve pattern would have to be reduced thus decreasing the value of deflection. This could be helpful in applications that require a fast response rather than large deflection.

3.2 SUMMARY

Analytical models developed helped to define the relationship between the various parameters of the beam as a function of temperature. The deflection of the beam was linearly related to the rise in temperature, whereas the curve for the deflection of the beam and the length shows a parabolic trend. It was found that a bimetallic beam of length 8 mm with cross-section area (500 μm X 100 μm) gave a free deflection of 54.17 μm at 200°C. The blocking force was calculated from Equation (37). The parabolic curve provided the design criteria in selection of the length of the beam. The slope of the curve did not change much for lengths between 7 mm and 8 mm. The value of blocking force was found to increase with temperature, but the increase was less significant for greater length of the beam (> 7 mm). For a beam of length 7 mm the blocking force was 0.23 N at 300°C and 0.38 N at 500°C.

Numerical analysis was also performed by using ANSYS (Version 5.7, ANSYS, Inc., Canonsburg, PA). Thermal input was given to the system and the temperature at each node served as an input in the mechanical deflection of the recurve. The yield stresses were less than the electroplated yield stress of nickel. Self-weight analysis confirmed that the entire array (11-element) will be able to support its own weight in

order to ensure the integrity of the array upon release with a maximum out of plane deflection of 1.25 μm . The value of time constant was estimated to be 1.44 seconds.

The analytical models derived were based on thermal and mechanical properties of the bulk materials. The variation with temperature for these properties was not well defined to take into account the changes in the behavior of the materials at the granular level with higher temperatures (in this case temperatures above 230°C for Invar). To obtain a consistent result with that of the experimental observation, new models may have to be developed to take into consideration the change in values of the physical parameters at higher temperatures. Temperature is given as an input to the base of the two end connectors and the temperature response is calculated when the steady state response is attained.

4. PROCESS COMPARISON

4.1 BACKGROUND

The recurve-array architecture was adopted from the design of the thermo-mechanical actuator, to fabricate the X-ray mask. The analytical and numerical results for deflection, blocking force, stress, and self-weight analysis estimated the model performance.

The first generation process was studied carefully step-by-step and a second generation process was proposed. In the new process, the X-ray mask was fabricated to incorporate both the alignment pattern and the structure into a single step. The idea was to eliminate the excess steps in the process and try to reduce the possible sources of error.

This process thus helped to reduce the alignment errors, which were described as ‘cumbersome and extremely unpredictable’ (Datta, 2001) and also made an attempt to quantify them. Tolerance stack analysis for a worst case scenario is presented in detail in Chapter 5. A detailed description of the new method and how it helped in reducing the errors is presented in this chapter.

4.2 CRITERION FOR X-RAY MASK FABRICATION

The bimetallic beam consisted of a composite beam of two different materials, and required fabrication of two X-ray masks, one for each layer. X-ray masks were fabricated from graphite and Kapton. Kapton was preferred over graphite for better resolution, sharp imaging during exposure, and relatively high shelf life. Process sheets for making Kapton and graphite X-ray masks are given in Appendix A. Alignment of the pattern during each exposure was a key issue in the composite beam fabrication. The fabrication process was carried out in two main steps each corresponding to one layer of

the composite beam. The first generation process is explained and the improved second-generation process is compared to, in detail.

4.3 FIRST GENERATION PROCESS

A passive thermomechanical valve was designed (Datta, 2001). The array architecture proposed by Ervin and Brie (1998) was modified to be used as a thermal bimetallic recurve. Nickel and Invar were chosen as the elements for the bimetallic beam. The known low CTE of Invar made it the best choice for the lower CTE element of the bimetallic beams. The recurve actuator was required to survive a maximum temperature of 500°C, with a deflection of 500 μm , so Invar was a proof of concept.

A three mask set was required to obtain the base layer or the patterning layer, the nickel layer, and the Invar-like layer. Both the bimetallic elements were to be plated side by side. Alignment markers were patterned on the base layer. These markers were used to align each of the layers. The three principal steps in the first generation fabrication process were:

- The alignment marks were patterned on the substrate, using UV lithography and an etch;
- X-ray mask – 1 was aligned with the patterned substrate for the first layer;
- X-ray mask – 2 was aligned and exposed for the second layer.

In the first step, the alignment marks were patterned on a titanium substrate. The titanium was oxidized and copper was plated. Positive resist SJR 5740 (Shipley MICROPOSIT, Philadelphia, PA) was spun and exposed, and nickel was electroplated to denote the alignment marks to a thickness of 10 μm . PMMA was bonded to the prepared substrate and exposed with the mask for first layer of the bimorph. An aligned exposure was

performed to match the alignment pattern of the substrate (nickel) and that of the X-ray mask (gold). Nickel was electroplated in the recesses and after polishing the overplated structures, PMMA was cast as a protective layer. Next, X-ray exposure was carried out by matching the alignment marks on the second X-ray mask to the base layer. Invar was electroplated into the resulting pattern adjacent to the first layer structures. The resulting recurve structure was lapped, polished, and etched out for the release of the structures.

For a bimetallic beam, it is imperative that both the elements be electroplated with good adhesion between the two layers. Due to the poor adhesion and poor alignment between the two layers, and to poor Invar quality the fabrication process led to the disintegration of the recurve structures. Nevertheless, this project did not result in successful structures. So the process was modified in the second generation approach.

4.4 SECOND GENERATION PROCESS

A modified microfabrication process evolved from evaluation of the first generation process.

The two main steps are:

- Resist was X-ray exposed using X-ray mask – 1 with alignment markers (Figure 4.1);
- X-ray mask – 2 was aligned with the developed alignment marks and exposed.

The second generation process reduced the number of alignment steps that contributed to the unsuccessful attempt at the earlier process. A detailed description of the second generation process is given in Section 4.5. The successful electrodeposition of Invar reduced the adhesion problems that resulted in the disintegration of the recurve.

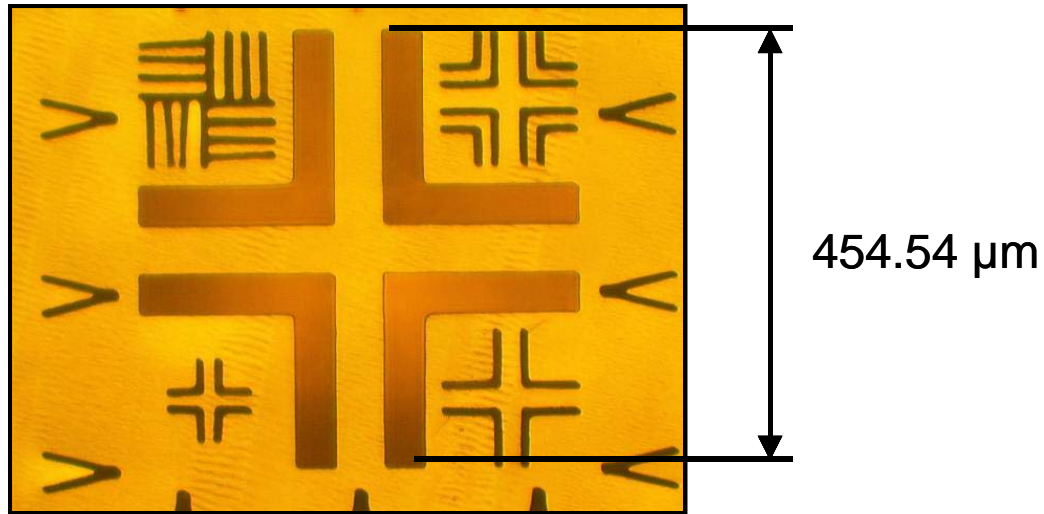


Figure 4.1: Alignment mark after development of PMMA (lowest feature size-10 μm). The errors introduced in the first generation process are compared to in detail in the next section and have been quantified in Chapter 5.

4.5 COMPARISON OF TWO GENERATIONS

In the first generation process, the fabrication process was a total of 25 steps. The three significant fabrication steps of the first generation process are listed in Section: 4.3. This process called for aligned exposures twice, which had alignment errors due to the manual alignment jig (error: $\pm 10 \mu\text{m}$), and resulted in a reduction of the alignment accuracy of the pattern. The $\pm 10 \mu\text{m}$ error was due to hardware and optics limitations and did not account for errors related to the alignment marks, which would probably add more error. Contrast played a major part in the alignment error. For aligned exposures, the alignment marks of the X-ray mask should have significant contrast to the prepared substrate in order to be able to be viewed through the alignment window.

All these errors were reduced in the improved method. Table 4.1 lists the criteria for the differences between the two methods. Aligning the pattern was critical as there

would be dimensional changes due to overlap or rotational error (the two beams were to be plated side and side). In the second generation method, 'the first alignment step' was modified to a 'no alignment step'. The alignment marks and the recurve pattern (first layer) were patterned in a single step. In the first X-ray exposure the recurve pattern and the alignment marks were X-ray exposed. However, the cost is possible loss of resolution of the alignment mark in resist. A minimum bottom dose of 3500 J/cm^3 was applied with the maximum top to bottom ratio of 4. A carbon filter of thickness $39.8 \mu\text{m}$ was used with a proximity gap of $500 \mu\text{m}$.

Initially, after the three cycles of development the alignment patterns were covered while the development process was continued for the rest of the recurve structure. This was done in order to ensure that the alignment marks did not overdevelop and remained intact. The aspect ratio of the alignment marks when developed completely would be 1:50. Hence the development process was cut short at an aspect ratio of around 1:30. A few of the samples were developed completely for further investigation. It was found that the alignment marks were rigid and did not break or dissolve, when they were completely developed but were not measured (see Figure 4.1). So the process was modified and the alignment marks were completely developed. This also helped in providing good contrast in the alignment process, as when completely developed the black oxide layer at the base was in good contrast to the developed PMMA patterns. The marks were protected during the electroplating step. Invar was electroplated with titanium as the electroplating base layer. The electrodeposition process is explained in detail in Chapter 6.

Table: 4.1 Comparison of previous and improved method.

No.	Criterion	1 st Generation	2 nd Generation
1	Total time required for fabrication	More time	Less time
2	Number of steps	25 steps	11 steps
3	Alignment error	There was a greater chance of error due to the shifting of mask and human error during aligned exposure ($\pm 10\mu\text{m}$)	Chances of error were reduced due to the alignment system using Jenoptic aligner ($\pm 1\mu\text{m}$)
4	Total error	More (as there were two alignment steps each with $\pm 10\mu\text{m}$ error)	Less (as only one aligned exposure- though there was some error due to the thickness of the substrate)

This approach increased the aspect ratio of the alignment markers from (1:1 to 50:1). These markers were now X-ray exposed with a PMMA resist thickness of 500 μm . This introduced gradual loss of the resist with a tapered profile from the top of the resist to the bottom. Based on tests carried out by Desta et al. (2001), the lateral dimensional loss of 500 μm thick patterned PMMA, with a ring energy of 1.5 GeV; and dose ratio of 4, was quantified to be 2.75 μm .

In the second X-ray exposure, for nickel electroplating, the alignment marks of the X-ray mask were matched to the alignment marks of PMMA on the substrate. The aligned X-ray exposure was carried out at the XRLM-1 beamline, which incorporates an optical alignment scanner DEX02 from Jenoptik GmbH (JENOPTIK Laser, OPTIK, Systeme GmbH, Jena, Germany). This scanner has a maximum scan length of 100 mm. The alignment error was $\pm 1\mu\text{m}$. This error was significantly less than the error introduced

Table 4.2: Process comparison of previous method and improved method

Previous Method		Improved Method	
Process	Time	Process	Time
Clean Titanium	5min	Clean Titanium	5 min
Oxidize Titanium	30min	Oxidize Titanium	30min
Plate copper	30min		
Polish lightly	20min		
Spin SJR 5740 (for photolithographic layer) and bake	2 hrs		
Expose and Develop SJR 5740 for alignment marks	30 min		
Plate Nickel Alignment marks	1 hr		
Oxidation of copper surface of wafer	30 min		
Bonding 500mm thick layer of PMMA to wafer	15 min + 8hrs in press	Bonding 500mm thick layer of PMMA to wafer	15 min + 8hrs in press
Alignment of 1 st mask with wafer	30 min-1 hr		
X-ray exposure of wafer with first mask	~ 5hrs	X-ray exposure of wafer with first mask	~ 5 hrs
Development of exposed PMMA	6 hrs	Development of exposed PMMA	6 hrs
Etching of black copper oxide	30min		
Plating Ni into mold	1 day	Plating Ni-Fe alloy into mold	14 days
Polishing/Lapping of surface	2 hrs	Polishing/Lapping of surface	2 hrs
Bonding of 2 nd layer of PMMA (500mm)	15 min + 8 hrs in press	PMMA Casting (50 microns)	15 min + 8 hrs
Fly-cutting 2 nd PMMA layer down to ~100mm	30 min		
Alignment of 2 nd mask with wafer	30 min - 1hr	Alignment of 2nd mask with wafer	30 min - 1hr
X-ray exposure - 2	~ 5 hrs	X-ray exposure - 2	~ 5 hrs
Development of exposed PMMA	6hrs	Development of exposed PMMA	6hrs
Etching of black copper oxide	30min		
Plating Ni-Fe alloy into mold	14 days	Plating Ni into mold	1day
Polishing/Lapping of surface	2 hrs	Polishing/Lapping of surface	2 hrs
Removal of PMMA	1 day	Removal of PMMA	1 day
Etching Copper & Titanium to release actuator	4-6 hrs	Etching Titanium to release actuator	30 minutes
Total Time involved	~ 440.4 hrs	Total Time involved	~ 427.8 hrs

by the manual alignment process used in the first generation process ($\pm 10 \mu\text{m}$).

Nickel was electroplated after the second aligned exposure and development of the resist. During the process of electroplating nickel the deposit grew along the walls of the Invar on one side and from the conductive base of titanium. If nickel were to be plated first (as was done in the first generation process), then the growth of Invar in both the directions may have led to a different composition ratio of iron: nickel.

Table 4.2 describes in detail the various processes steps followed in both the methods. The fabrication steps followed are described in detail in Chapter 5. The total time required for the first generation process (440.4 hours) was not much different when compared to second generation (427.8 hours). Nevertheless, the second generation process had fewer steps (11) as compared to the first (25). This reduced the chance of error or mishandling. The resulting increased accuracy, as each step incorporated machine and handling error, led to the successful release of the recurve. With proper approach to the fabrication cycle and errors being reduced in the alignment process by the design of new X-ray mask, the overall output improved. The recurve array structures were fabricated successfully (described in detail in Chapter 5) and were later tested for thermomechanical properties (Chapter 7).

4.6 TYPES OF X-RAY MASK

Two X-ray masks were made by different processes, one for each part of the device;

- (1) First layer X-ray mask;
- (2) X-ray mask for aligned exposure;

The basic X-ray mask was the one which was used for exposure of the first layer of the resist to the X-ray mask. In the X-ray mask for aligned exposure, the X-ray mask had alignment markers, placed at the four corners of the recurve pattern. These markers were transparent to light. The markers were patterned by UV lithography on the glass ring that was attached to the graphite disc. The detailed description of fabrication of the basic X-ray mask and the X-ray mask for aligned exposures is given in the following sections.

4.6.1 BASIC X-RAY MASK

In this process graphite was selected as the mask membrane. Graphite wafers (POCO Graphite Inc, Texas, DFP-3, density-1.8 g/cm³) were used as the substrate. The wafers were cleaned using acetone and IPA. Glass disks with a diameter the same as those of the wafers (4 inch) were also cleaned and then dried in the oven at a temperature of 120°C for 30 minutes and then slowed to room temperature in 1 hour. The glass disks were spin coated with AZ – 4620 (MicroChem. Corp., Newton, MA) and bonded to the graphite wafers. Care was taken to ensure a smooth contact between the wafer and the glass to avoid bubbles. Glass disks were bonded to the wafers to ensure a rigid base while subsequently fly cutting the wafer. They were then baked for 30 minutes at 70°C and then cooled down to room temperature over 4 hours. At this stage the resist hardened providing good adhesion. The graphite wafer was fly cut down to a thickness of 125 µm.

After flycutting the graphite wafer was debonded by soaking it in acetone for 5 – 6 minutes. It was cleaned using acetone and IPA, followed by rinsing in DI water. The wafer was then dried at 100 °C for 25 minutes to evaporate any volatile matter. The wafer was now ready for the actual mask fabrication process. A layer of SU-8 25 (MicroChem,

Newton, MA) an epoxy-based resist, was spun on the wafer to a thickness of 50 μm . Graphite is a porous material so parameters for spin coating were optimized to get the desired thickness by increasing the amount of the resist and decreasing the speed compared to metals or silicon substrates. This was followed by pre-exposure baking (soft-baking in the oven) following an increasing temperature ramp from 60°C to 95°C in 10 minutes, maintaining that temperature for 60 minutes, and followed by a cool down to room temperature inside the oven over a period of 4-5 hours. UV exposure was performed with the incident dose of 330 mJ/cm^2 . Calculations revealed that the incident dose to be 86 % of the actual dosage of the UV radiation (Quintel UL7000-OBS Aligner and DUV Exposure Station, QUINTEL Corporation, San Jose, CA), the rest of the incident radiation is lost in reflection and absorption by the substrate. This factor was taken into account for the total post-exposure bake, or hard baking. The pattern was similar to the pre-bake. The temperature was increased from 60°C to 95°C over 10 minutes inside the oven, kept at a constant temperature for 20 minutes, and followed by cooling down to room temperature in the oven for over 4 hours.

The samples were developed in SU-8 developer (Micro Chem. Corp., Newton, MA) for about 6 minutes, examined under a microscope to detect any remaining residue and were soaked in IPA followed by a rinse in DI water. In the case of the appearance of a white residue, the cycle was repeated for another minute, before rinsing again in an IPA solution. The developed samples were electroplated in a gold electroplating bath with a current density of 2 mA/cm^2 and an electrodeposition rate of 4 $\mu\text{m}/\text{hour}$. Electroplating was continued until a 15 μm layer of gold in the mold was reached.

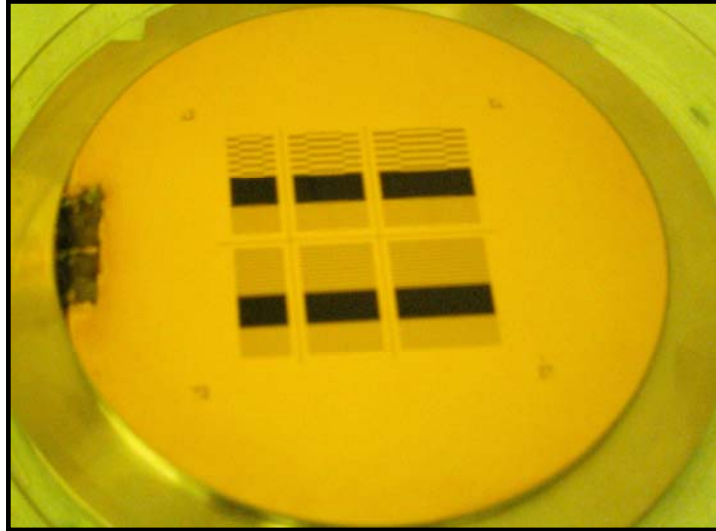


Figure 4.2: X-ray mask for improved method for the first layer of Invar.

4.6.2 X-RAY MASK FOR ALIGNED EXPOSURE

The graphite was glued to a glass ring using a UV cured epoxy. The outer diameter of the ring was same diameter as the graphite, but the inner diameter of the ring was chosen so that it was in the region between the pattern and the alignment marks. The ring was glued carefully to insure that there was no sagging in the graphite after bonding. The glue was cured for 8 hrs at room temperature, before moving to the next step.

Chrome and gold ($0.89\ \mu\text{ms}$) were evaporated over the entire surface of glass ring and graphite. The wafer was spin coated with SU-8:25 to a thickness of about $55\text{-}60\ \mu\text{m}$. The pre-bake cycle was the same as in Section 4.2.1. The wafer was exposed by UV over the entire surface. The post-bake cycle was followed by a slow cool down process. The alignment marks and pattern were developed after the post bake cycle. The chrome and gold were etched out from the alignment marks over the glass ring and then gold was electroplated into the pattern.

4.7 SUMMARY

The second generation process was developed after investigating the sources of error of the first generation process. The second generation process had less number of steps than the first generations process and thereby helped in reducing the machine and handling errors associated with each step of the fabrication process. The two alignment steps were reduced to one aligned exposure, though there was some error introduced ($\pm 1.625 \mu\text{m}$), it was less significant than that introduced by aligning the substrate twice. The modified X-ray mask was successfully fabricated and used for the alignment of the pattern and the alignment marks in one single step.

5. FABRICATION OF RECURVE STRUCTURES

5.1 INTRODUCTION:

A new and improved second generation fabrication method was implemented. The tolerance stack analysis was performed for each of the processes. The following sections describe in detail the revised fabrication processes and the resulting release of the recurve structures.

5.2 ANALYSIS OF FIRST & SECOND GENERATION PROCESS BASED ON TOLERANCE STACKS

A tolerance stack analysis was carried out for the process steps. Error in each process was estimated by the worst case model.

Equation (39) gives the total worst case tolerance error (Drake, 1999):

$$t_{wc} = \sum_{i=1}^n |a_i t_i| \quad (39)$$

where

t_{wc} = maximum expected variation (μm)

a_i = sensitivity factor that defines the magnitude and direction of the i^{th} dimension

t_i = equal bi-lateral tolerance of the i^{th} element of the stack (μm)

Using the worst case model, the minimum gap is the mean value minus the “worst case” variation and the maximum gap is equal to the mean value plus the “worst case” variation.

In the first generation process, there were three layers included in the fabrication process. The first layer was the base layer with the alignment marks or the patterning layer, the second layer was the structures for Ni, and the third was the Invar structures.

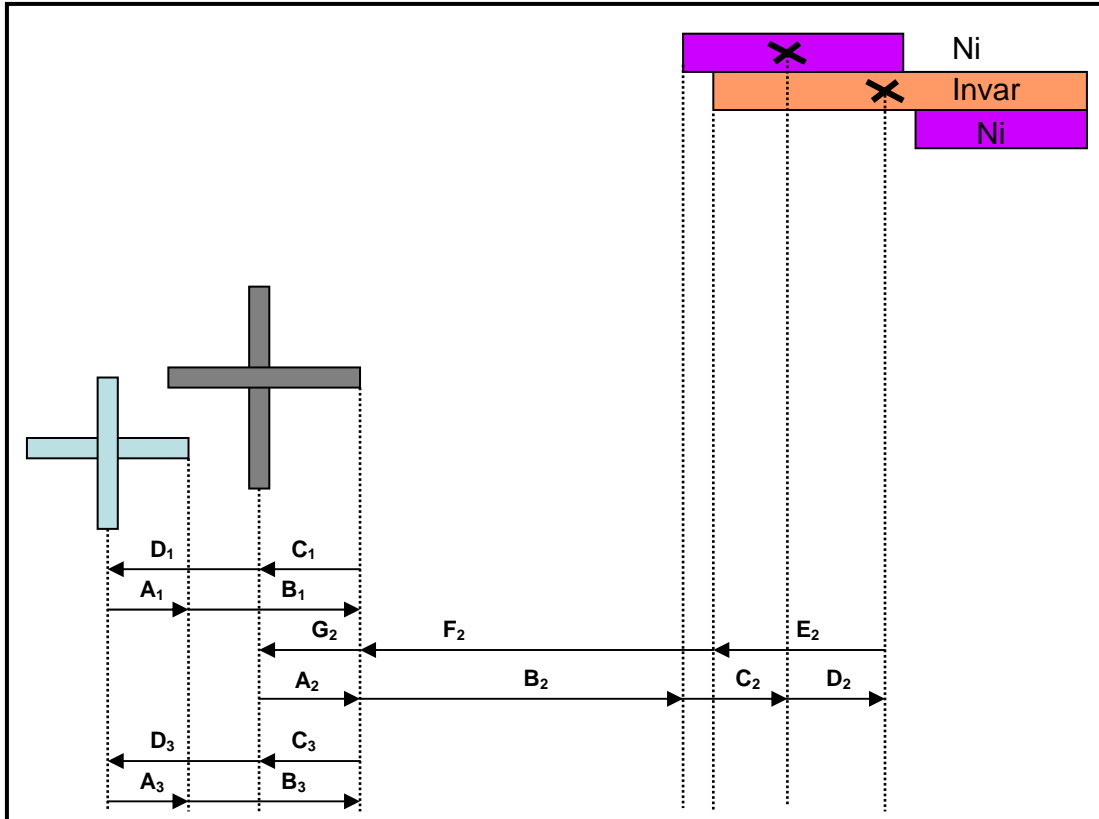


Figure: 5.1 Tolerance stack analysis for the first generation process.

Variables with suffices 1, 2 and 3, each represent the three layers, respectively. The tolerance is calculated step by step as each layer of the device is fabricated.

Figure 5.1 gives a schematic of the stacking of tolerances for the first generation process. The error involved during X-ray exposure of 500 μm thick PMMA (layer 2 and layer 3) was determined based on the work done by Desta et al. (2001) as $\pm 1.625 \mu\text{m}$.

To calculate the error by tolerance stack process the fabrication process was divided into three main steps.

Step 1: Layer 1 \rightarrow Layer 2

This step locates the Ni layer relative to the substrate. The loop for alignment marked A_1, B_1, C_1 and D_1 is shown in Figure 5.1. The alignment marks are patterned using the UV (Oriel UV Exposure station, LOT-Oriel, Darmstadt, Germany). The

distances A_1 , B_1 , C_1 and D_1 are tabulated along with the tolerance error for each of the distances. This completes one entire loop for the first step. The alignment error was introduced due to the manual alignment process ($\pm 10 \mu\text{m}$). Table 5.1 shows the detailed list of variables used for calculation of the error. Based on the worst case model the tolerance value for B_1 equals $\pm 13.25 \mu\text{m}$.

Step 2: Layer 1 \rightarrow Layer 3

This step relates the alignment marks on Layer 1 and the Layer 3 Invar structures. Variables A_3 , B_3 , C_3 and D_3 represent a complete loop for the mean dimension from the base layer to the Invar layer and back to the base layer as shown in Table 5.2. The alignment error is same as Step 1, introduced due to the manual alignment process. On solving for B_3 using the loop equation we get $\pm 13.25 \mu\text{m}$.

Step 3: Layer 2 \rightarrow Layer 3

This step locates structures of layer 2 to structures on layer 3. Table 5.3 lists the variable for step 3. A_2 , C_2 , D_2 , E_2 , F_2 and G_2 are the known variables. The value for H_2 is calculated based on the worst case sum from step 1 and step 2 ($H_2 = B_1 + B_3$; $13.25 \mu\text{m} + 13.25 \mu\text{m}$; $26.50 \mu\text{m}$). The value of D_2 is the sum of the offset (known offset of $\pm 10 \mu\text{m}$; this gap was introduced into the design of the X-ray mask in between the two layers to provide for good contact) and the tolerance (unknown). Based on the loop equation for Step 3 the tolerance is calculated as $\pm 33\mu\text{m}$.

In the second generation the alignment layer was merged into the first structural layer. The schematic representation of the second generation process is shown in Figure 5.2. The base layer consisted of the alignment markers and also the Invar layer. Variables A_1 , B_1 , C_1 , D_1 , E_1 , F_1 , G_1 and H_1 represent the mean dimensions of the distances of the

Table 5.1 Variables used in Step 1.

Variable Name	Mean Dimension (μm)	Tolerance (μm)	Known/Unknown	Distance
A ₁	227.27	+ 1.625	Known	Center of cross to the edge of cross (Layer 1)
B ₁	NA	x	Unknown	Distance to the edge of cross on layer 2
C ₁	227.27	-1.625	Known	Edge of cross to the center of structure on layer 2
D ₁	0	± 10	Given $\pm 10 \mu\text{m}$	Alignment error

complete loop from the base layer to the layer of nickel to the base layer.

Here H₁ represents the error involved during alignment. In the second generation process the XRLM-1 beamline at CAMD was used. This beamline had a built-in alignment system with tolerance of $\pm 2 \mu\text{m}$. Table 5.4 gives the list of the errors in each of the process steps. The net total error for the second generation method was determined to be $\pm 8.5 \mu\text{m}$. The tolerance stack analysis can be performed in both the X and the Y directions.

Table 5.2 Variables used in Step 2.

Variable Name	Mean Dimension (μm)	Tolerance (μm)	Known/Unknown	Distance
A ₃	227.27	+ 1.625	Known	Center of cross to the edge of cross (Layer 1)
B ₃	NA	x	Unknown	Distance to the edge of cross on layer 3
C ₃	227.27	-1.625	Known	Edge of cross to the center of structure on layer 3
D ₃	0	± 10	Given $\pm 10 \mu\text{m}$	Alignment error

Table 5.3 Variables used in Step 3.

Variable Name	Mean Dimension (μm)	Tolerance (μm)	Known/Unknown	Distance
A_2	227.27	+ 1.625	Known	Distance from center of cross to the edge of cross on layer 2
B_2	6729.53	+0.00	Known	Edge of cross to the edge of layer 2 structure
C_2	1000	+1.625	Known	Edge of layer 2 structure to centroid of layer 2 structure
D_2	± 10	x	Known offset but unknown tolerance	Centroid of layer 2 to centroid of layer 3
E_2	1000	-1.625	Known	Centroid of layer 3 to edge of layer 3 structure
F_2	6729.53	+0.00	Known	Edge of layer 3 structure to edge of layer 3 cross
G_2	227.27	-1.625	Known	Edge of cross to center of cross on layer 3
H_2	NA	26.50	Known	Offset layer 2 to layer 3

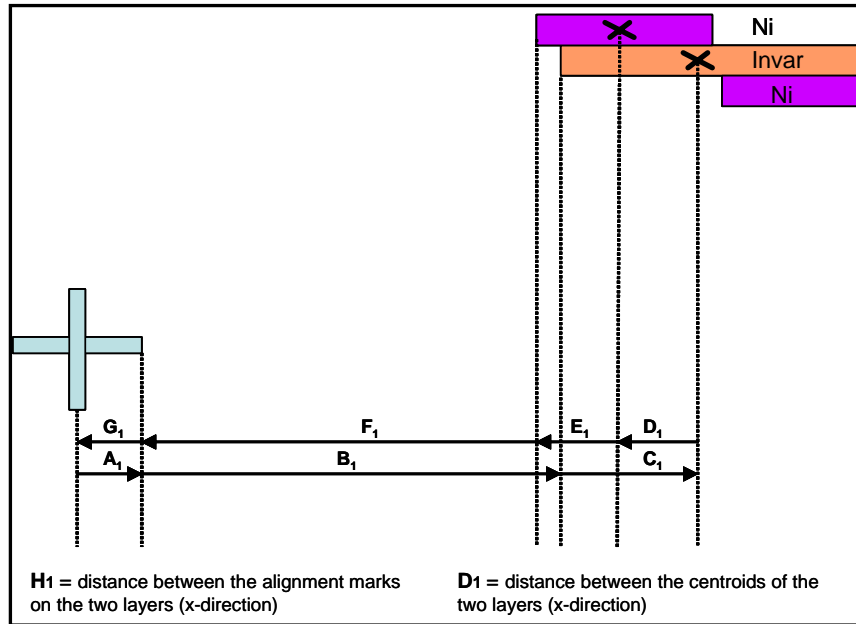


Figure: 5.2 Tolerance stack analysis for the second generation process.

Table 5.4 Variables used in second generation process.

Variable Name	Mean Dimension (μm)	Tolerance (μm)	Known/Unknown	Distance
A ₁	227.27	+ 1.625	Known	Distance from center of cross to the edge of cross on layer 1
B ₁	6729.53	+0.00	Known	Edge of cross to the edge of layer 1 structure
C ₁	1000	+1.625	Known	Edge of layer 1 structure to centroid of layer 2 structure
D ₁	± 10	x	Known offset but unknown tolerance	Centroid of layer 2 to centroid of layer 1
E ₁	1000	-1.625	Known	Centroid of layer 1 to edge of layer 1 structure
F ₁	6729.53	-0.00	Known	Edge of layer 1 structure to edge of layer 1 cross
G ₁	227.27	-1.625	Known	Edge of cross to center of cross on layer 1
H ₁	0	± 2	Known	Alignment error ($\pm 2 \mu\text{m}$)

5.3 FABRICATION PROCESS FOR THE IMPROVED METHOD (Second Generation)

5.3.1: SUBSTRATE PREPARATION

Titanium was chosen as the substrate for the prototype fabrication process. Titanium is conductive and when oxidized binds well with PMMA. It thus acts as a good base for further microfabrication processes. A 1000 mm X 300 mm titanium sheet with 0.89 mm thickness was cut into circular disks of 101.6 mm diameter.

The Ti wafer was immersed in 15% HF solution for two minutes. This process eliminated the natural oxide layer and also helped in cleaning any dirt on the surface. This was followed by a DI water rinse. The cleaned wafers were next oxidized. The recipe for titanium oxidation solution is given in Table E.1 (Appendix E). Solutions were made by adding measured quantities of sodium hydroxide and DI water followed by

heating to 65°C. Since H₂O₂ is very unstable at high temperature, it was added just a couple of minutes before immersion of the titanium wafers. The wafers were held in the solution for 15-20 minutes until the surface became completely oxidized. The wafers were rinsed in DI water, and dried completely to ensure a uniform oxide layer throughout the surface.

5.3.2: PMMA BONDING

A positive X-Ray resist was bonded to the oxidized titanium wafers. PMMA disks were annealed at 88°C for 30 minutes and slowly cooled to room temperature over one hour. This helped the bonding process and subsequent development of the samples. Bonding glue was prepared as shown in Table E.2 (Appendix E).

This recipe made approximately five grams of solution. Polymerized MMA / Methyl Methacrylate (PMMA /MMA), Benzyl Peroxide (BPO) and Methacryloxypropyl-trimethoxysilane (MEMO) were first added. The mixture was stirred to ensure all of the BPO was dissolved completely and it was placed in vacuum to ensure that all the bubbles were eliminated. Dimethyl Aniline (DMA) was added last. After the solution was mixed properly and vacuumed, it was ensured that there were no bubbles in the solution. Adhesive was siphoned into a 10 ml syringe. The solution was dispensed on the oxidized wafers, and PMMA disks were carefully placed on the wafers and taped on the sides. This restricted the movement of the resist during bonding.

The bonded wafers were placed under a hydraulic press. It was found that for the PMMA to bond well to the wafers a pressure of 2 bars was required, pressure greater or less, caused the PMMA to detach from the wafer during the subsequent processes. The bonded resist was placed under the press for 8 hours. After curing, the sample was fly cut

to the required thickness (500 μm). The rotational speed of the tool bit was maintained at 50 rpm. As PMMA is a soft material, 100 μm was fly cut during the initial cut and the final cut was made with 20 μm . After fly cutting the PMMA was ready for exposure.

5.3.3: X-RAY EXPOSURE AND DEVELOPMENT

The PMMA was exposed at CAMD (Center for Advanced Microstructures and Devices), at LSU. Synchrotron radiation provides a collimated source of X-Rays. The exposure-dosage was calculated with different bottom doses and an optimum dosage of 2500, was determined based on the development cycle.

The XRLM-1 beamline was used for the exposures due to its capability of aligned exposure option. The operating beam energy was 1.3 GeV. In the first exposure of the sample, the alignment marks were patterned along with the recurve structure.

Development of the exposed sample was done using GG Developer solution and GG rinse solution. The composition of the solution is given in Table E.3 and E.4 (Appendix E). The sample was developed using a 20 - 40 cycle; 20 minutes in the developer and 40 minutes in the rinse solution for each 100 μm 's of height.

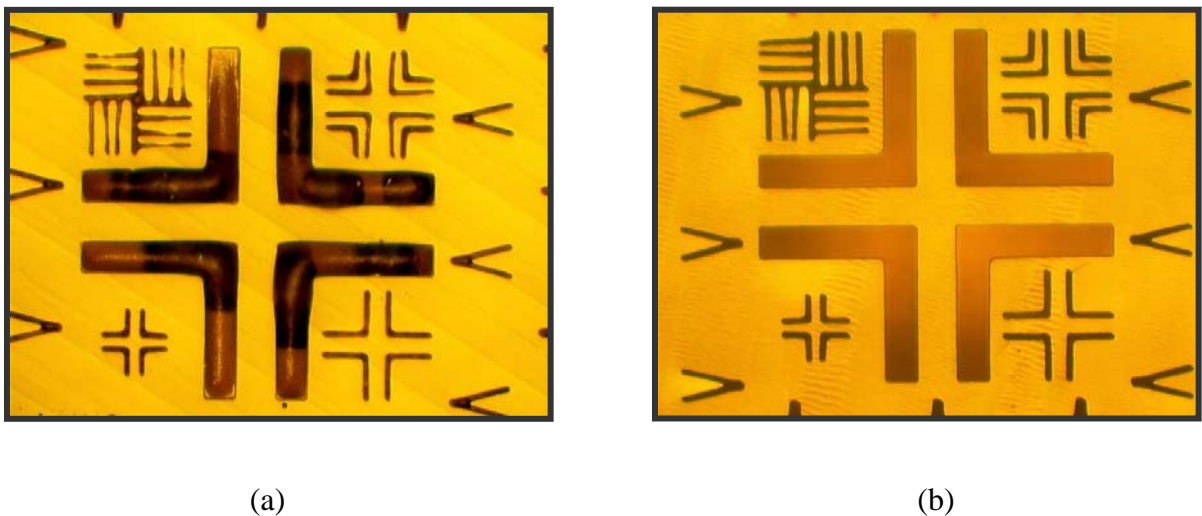


Figure 5.3: Alignment marks in the first layer: (a) After exposure; (b) Developed (Picture depicting the survival of the alignment marks during development process).

Care was taken to make sure the alignment marks were protected (the alignment marks were taped) during the development cycles. Figure 5.3 shows the alignment marks before and after development. This cycle was followed by a long rinse in DI water (15-20 minutes). The sample was now ready for electroplating.

5.3.4: INVAR ELECTRODEPOSITION

The development of the first layer (Figure 5.4) was followed by Invar electrodeposition. The electroplating solution was prepared and the sample was plated as described in detail in Chapter 6. Plating was continued for 15 days to obtain an overplated sample. The pH of the bath was sampled every 12 hours, and was maintained at a pH level of 2 by using sulfamic acid. The temperature of the bath was kept constant to within $\pm 1^{\circ}\text{C}$ at 40°C . The temperature of the bath played an important role in maintaining the ratio of Ni to Fe in the deposit. The samples were rinsed in DI water and air-dried before polishing and lapping.

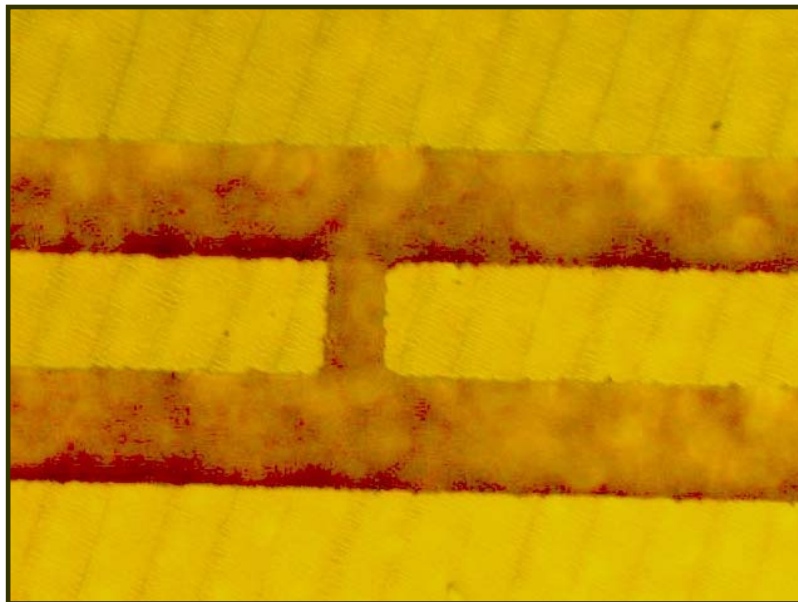


Figure 5.4: Exposed and developed PMMA- First layer.

5.3.5: LAPPING AND POLISHING

Invar was soft metal to work with as compared to nickel (Vickers hardness value with 50 g weight: 257, (Sharpe and McAleavey; 1998)). The sample posts were found to grind down more quickly than nickel, when applying the same amount of force during lapping.

The electroplated samples were overplated. A LM 115 Hyprez lapping machine (Engis Corp., Wheeling, IL) was used for polishing and lapping the electroplated samples to a smooth finish. A composite iron lap plate was used to combine both lapping and polishing in one step. The flatness of the lap plate was maintained by using a diamond conditioning ring. It was found that for every twenty minutes of lapping, 2-3 minutes of conditioning were necessary to ensure uniform flatness (1-2 μm across). Slurries (oil and water based; Engis Corp., Wheeling, IL) were used to lap the sample. A range of slurries from 15 μm to 1 μm (Appendix – Table E.5) followed by a 1 μm diamond paste were used to lap the sample to a mirror finish. Figure 5.5 shows the Invar lapped to a mirror finish.

5.3.6: PMMA CASTING

After the sample was polished and lapped, it was exposed a second time for the next layer. Before the X-ray exposure was carried out for second layer, PMMA was cast on top. This provided a protective, non-conductive layer, over the Invar. The plating of nickel in the next step, would then build up from the electroplating base and the side wall of the electroplated Invar. A 30 μm thick shim was placed around the perimeter of the first layer. The PMMA bonding glue was prepared and poured in the center of the pattern. Weights were placed on the sample with a glass plate in between to ensure

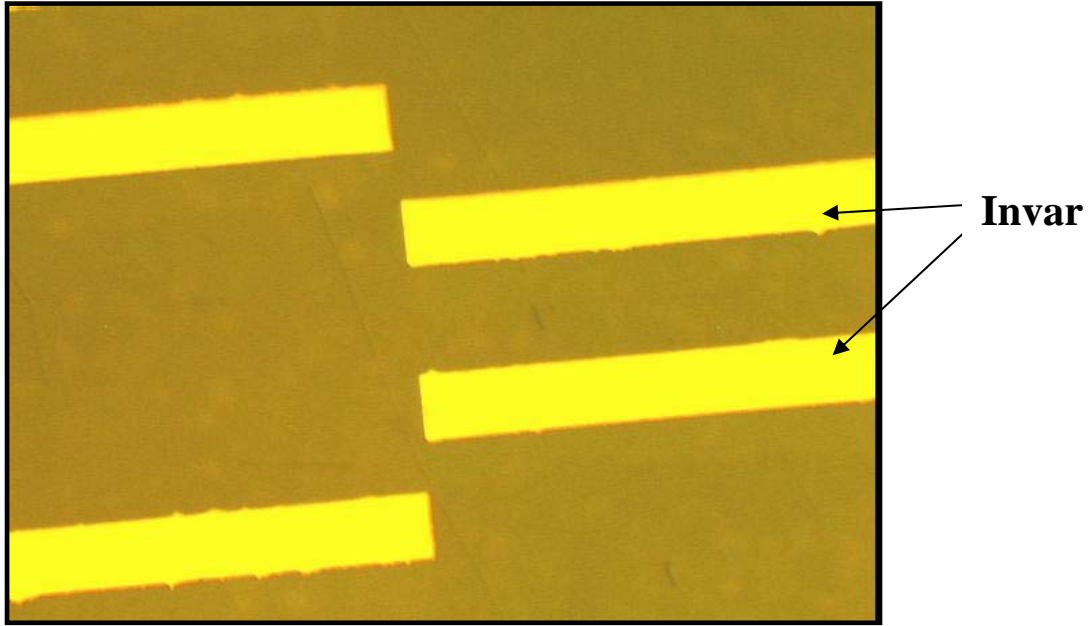


Figure 5.5: Invar plated and polished.

flatness of the cast. A pressure of 28.24 KPa was applied with the bonding press. The setup was kept under pressure for 8 hours to ensure complete curing of the PMMA glue.

5.3.7: ALIGNED EXPOSURE AND DEVELOPMENT

The sample was exposed on the XRLM-1 beamline (Jenoptik DEX02, Aligner System, JENOPTIK Laser, OPTIK, Systeme GmbH, Jena, Germany). The sample was aligned with the second layer X-ray mask. This was a critical step in the microfabrication cycle. Proper alignment was a key to having the halves of the recurve in position to function as designed. A 10 μm overlap was provided in the X-Ray mask pattern to account for potential misalignment. A good aligned exposure was performed on the beamline; machine error with the Jenoptik was within $\pm 2 \mu\text{m}$. The offset of the sample after alignment was found to be within 1-2 μm with reference to the optical system at the user's end. The sample was exposed with a bottom dose of 3000 mJ/cm^3 with ring energy of 1.3 GeV.

The exposed sample was developed using the same procedure as described in Section 5.2.3. The developed sample was placed in a DI water rinse for 30 minutes for a final rinse.

5.3.8: ELECTROPLATING (Ni)

During the electroplating for nickel the deposit grew along the walls of Invar on one side and from the conductive base of titanium, if nickel were to be plated first then, the growth of Invar in both the directions would have led to a different composition ratio of iron to nickel.

Nickel was electrodeposited in the developed second layer PMMA patterns. A nickel sulfamate-based electroplating solution was used. Nickel pellets in a titanium basket were the anode. The titanium basket was wrapped in a cotton filter (5 μm pore size) cloth to prevent residue from entering the plating solution. The plating solution was mixed and filtered after mixing. The nickel sulfamate in the solution acted as a stress reducer. Boric acid acted as a buffering agent to minimize the pH rise of the solution while electroplating. Lauryl sulfate served as a wetting agent reducing the surface tension of the solution, which enabled penetration into deep recesses in the microstructures and also contributed to low stress plating. The pH of the bath was made up to 3.8 using sulfamic acid. The solution was constantly filtered during the electrodeposition process by connecting the bath to a filter pump. The temperature of the solution was kept constant by a water bath, operated at a temperature of 56°C. A current density of 15 mA/cm² was used; the electroplating process took 30 hours to ensure over-plating. Polishing was done as described in section 5.2.5.

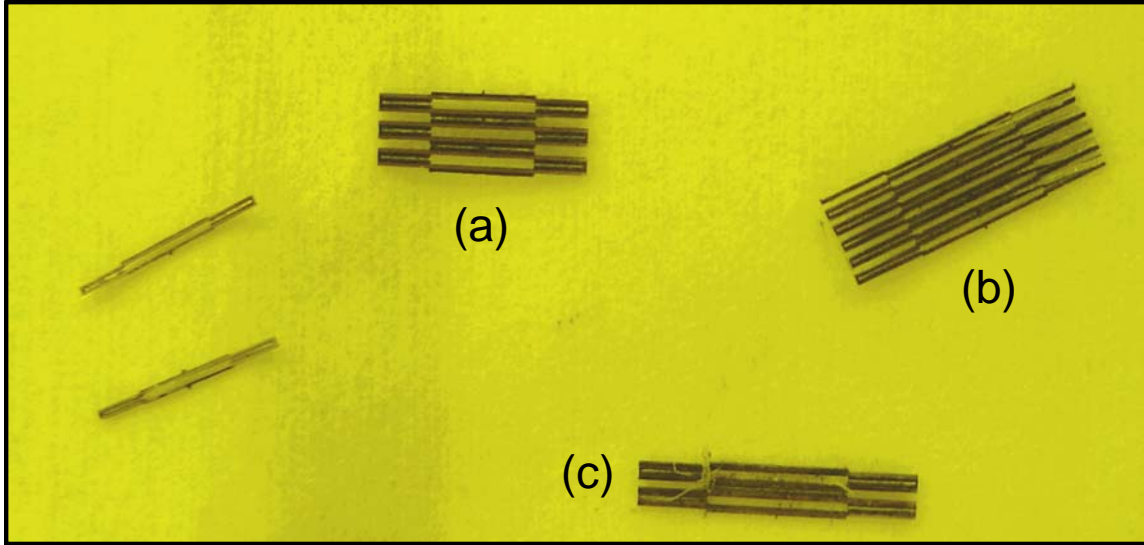


Figure 5.6: Released structures. The figure shows 2 X 2, 4 X 2, 6 X 2 and 11 X 2 recurve array structures (close-up view).

5.2.9: ETCHING AND RELEASE OF THE RECURVE STRUCTURES

Etching was used to release the free-standing recurve pattern. Before the devices were released the substrate was placed in acetone in an ultrasound bath to remove all of the PMMA. A commercial etching solution (5% HF, Transene, Inc. MA) was used to etch the titanium. The etching solution was non-reactive to iron and nickel and reactive to only titanium.

Table 5.5 Dimensions of the released bimorph array structures.

(No.) - (Designation Table 3.1)	Array Size	Length (μm)	Width(μm)	Height(μm)
(a) - (A ₂)	6 x 2	8000	200	500
(b) - (B ₁)	11 x 2	12000	100	500
(c) - (B ₂)	4 x 2	12000	200	500
(d) - (C ₂)	6 x 2	16000	200	500

The low concentration of HF took around twenty minutes to release the recurves completely. The titanium etching was an exothermic process. The recurve structures were handled very carefully. There were twelve recurve array structures on the wafer. Eleven were released successfully and one of them disintegrated. The recurve pattern was released successfully from the electroplating base. Figure 5.6 shows the released arrays of bimorphs and Table 5.5 gives the dimensions of each array (Table 3.1 gives the list of recurve arrays with dimensions. Note that each array consists of two sets of arrays when released). Figure 5.7 shows a released bimorph structure with array size (6 X 2).

5.3 SUMMARY

The recurve array was fabricated based on the improved method. This process led to a significant reduction in error during alignment. Starting from substrate preparation to the final release of the structures the process was a success, though there was not a

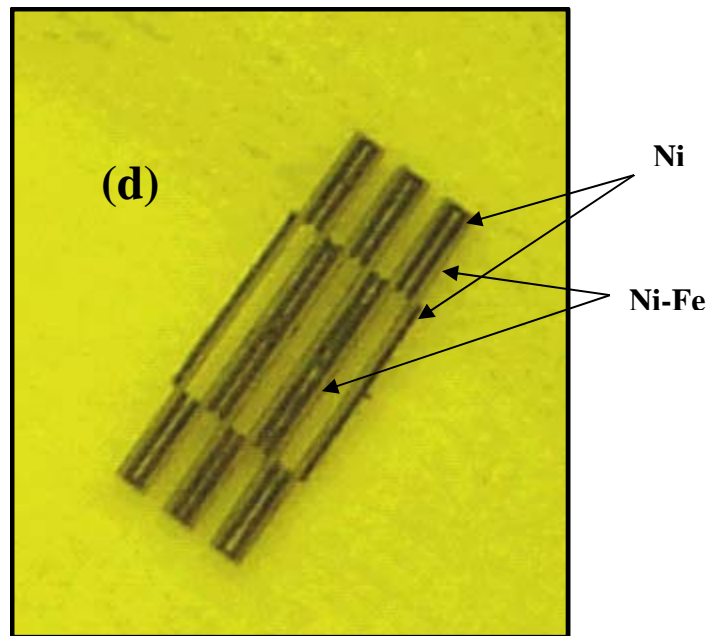


Figure 5.7: Bimorph structure. The bimetallic beams are clearly seen in the 6 X 2 array ($L = 12000 \mu\text{m}$, $w = 200 \mu\text{m}$ and $h = 500 \mu\text{m}$).

significant time difference in both the methods, the improved method led to a reduction in the number of steps and less chances of error associated with each step. The process parameters were better defined as the reduction in number of steps led to decrease in machine and handling error associated with each step. This method proved beneficial in reducing the number of times the X-ray mask had to be aligned. Fabrication steps were carried out step by step and the final structures were successfully released from the substrate.

6. INVAR PROPERTIES AND ELECTRODEPOSITION

6.1 INTRODUCTION

Electroplating is a process for metal and/or metal alloy deposition by electrolysis from a salt or aqueous solution. A metal salt dissolved in a polar solvent is present in an ionic form (Romankiw and Sullivan, 1997). In this chapter electrodeposition of Invar, an alloy of Fe and Ni in the ratio of 64:36, is explained in detail. Electrodeposition of Fe-Ni alloys is of significance because of the anomalous co-deposition phenomenon (Marsh, 1938). At this composition the magnetic effects balance the thermal effects restricting its expansion. Attempts were made to electroplate Invar (Datta, 2001) but the composition ratio could not be maintained along the depth of the post. The electroplating bath was modified and a pulse plating approach was applied (Namburi, 2002). The composition of Invar was more uniform but it still needed to improve. The electrodeposition process followed is described in detail. The resulting posts obtained were investigated along the depth for the desired composition ratio and tested for CTE.

6.2 INVAR

Since its discovery in 1897 by Guillaume, Invar has stimulated many experimental and theoretical studies (Schilfgaard, 1999). Low thermal expansion metals such as Invar are potentially useful for MEMS applications due to their dimensional stability over a wide range of temperatures. Invar is a face centered cubic alloy of iron and nickel in the ratio of 64:36.

Betteridge (1977) plotted (Figure 6.1) the CTE for bulk nickel alloys as a function of temperature. The thermal expansion coefficient for Invar is the lowest over the medium

Nickel and Nickel Alloys

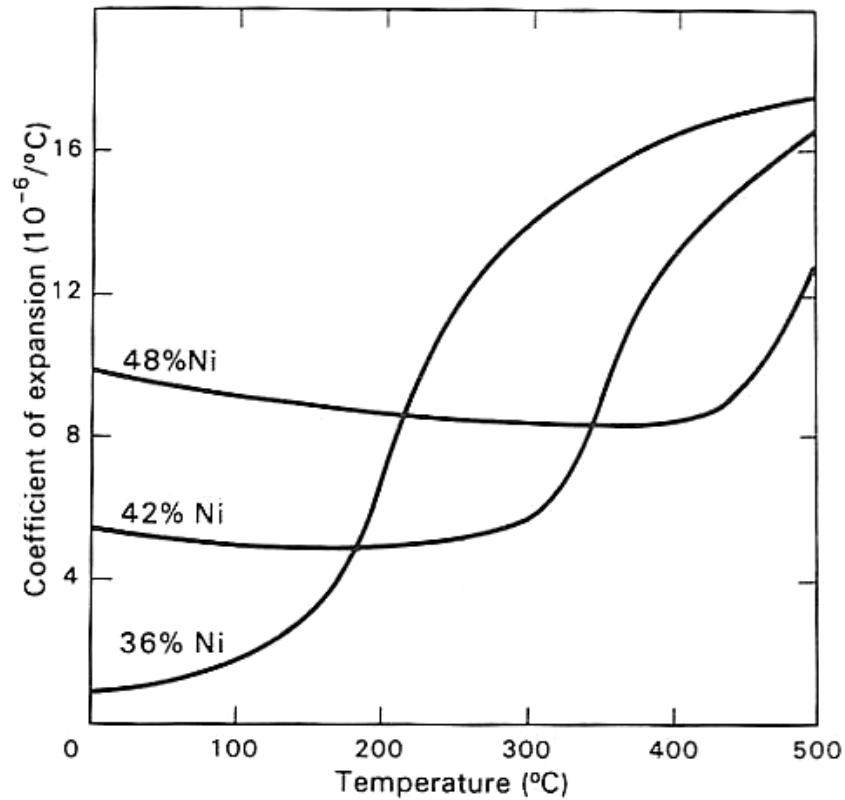


Figure 6.1 Expansion coefficient of nickel–iron alloys with varying percent of nickel (Betteridge, 1977).

temperature range (0 to 100 $^{\circ}\text{C}$), but it increases with a steep slope at higher temperatures from around 160 $^{\circ}\text{C}$ to 250 $^{\circ}\text{C}$. Alloys with higher nickel content have flatter slopes at high temperatures than Invar. The lowest CTE value for Invar is based on the magnetic properties of the alloy. There is a balance between the thermal expansion and contraction due to magnetostriction (Yang and Goldstein, 1997).

The Curie point is the temperature above which a ferromagnet loses its ability to possess a net (spontaneous) magnetization in the absence of an external magnetic field (Yang and Goldstein, 1997). At temperatures below the Curie point, magnetic moments in ferromagnetic materials are partially aligned within magnetic domains. As the Curie

point is approached, thermal fluctuations increasingly destroy this alignment, until the net magnetization becomes zero at and above the Curie point. This causes the coefficient of thermal expansion (CTE) to vary. The value of CTE below the Curie temperature is lower than that for higher temperatures. Thus the amount of deflection produced, which is directly proportional to the difference in CTE's of the bimetallic elements, is greater below the Curie temperature.

The Curie point is an important factor for Invar, as above the Curie point, Invar ceases to be magnetic. Moruzzi (1992) inferred the magnetic behavior of Invar from the theory of Debye-Gruneisen. This theory is based on the thermal evolution of the free-energy in the first principle of electronic structure calculation. Kwon and Kim (1992) studied the elastic properties of ferromagnetic systems. The co-relation energy was found to govern the elastic behavior near the Curie temperature, which is related to the electron-strain interaction in the ferromagnetic Invar alloy. Experiments by Junma et al. (2000), found that yield stress decreased with an increase in temperature from 20°C to 180°C, then fluctuated around 120-130 MPa.

Figure 6.2 gives the plot of CTE with change in percent of nickel and iron in an iron-nickel alloy and the corresponding variation in Curie temperature. As the amount of Ni increases in an iron-nickel alloy, the Curie temperature increases. The value of CTE is found to decrease with increase in Ni content until it reaches 36%. With further increase in Ni % the CTE value for the alloy increases. At this value of 36% Ni and 64% Fe (or Invar), the alloy exhibits the lowest CTE value. For the given application, achieving the lowest possible CTE for the alloy was the primary issue, in order to have the maximum deflection of the bimorph.

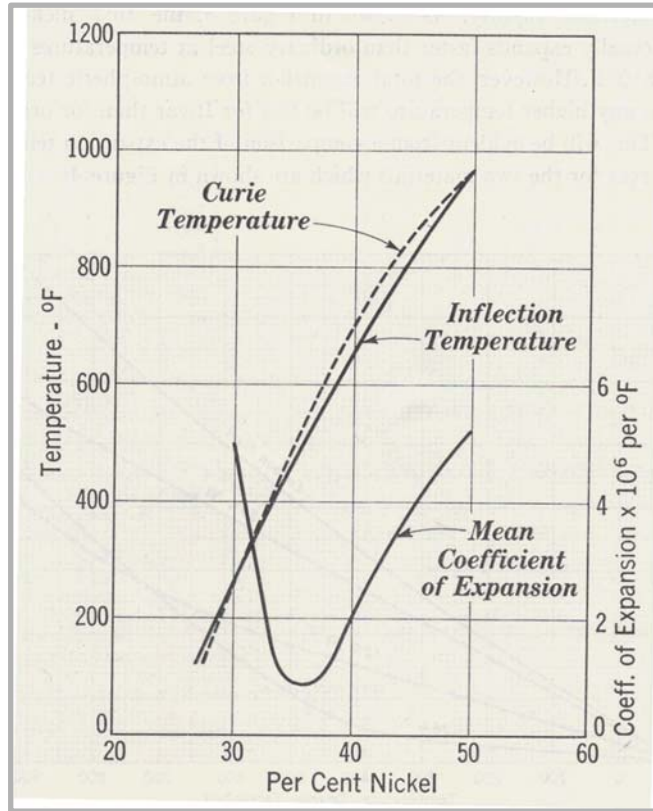


Figure 6.2 Curie temperature with increase in coefficient of thermal expansion and percent of nickel (Marsh, 1938).

6.3 INVESTIGATION OF NICKEL-IRON ALLOYS FOR MEMS

As the temperature increases, the size of the grains in Invar increases. This leads to a decrease in the physical and thermomechanical properties of Invar. Addition of elements to Invar has been found to act as a binding agent and stop the grain growth at higher temperatures (Junma et al., 2000). Cobalt can be added to the alloy to maintain the low coefficient value and at the same time it helps to increase the Curie temperature. This allows the CTE value to be maintained through a higher and wider range of temperature. Therefore cobalt increases the working temperature for the alloy.

Nickel percent of the alloy can be increased from 36% to 42%. Though this has an effect on the CTE of the alloy, it helps in maintaining a uniform CTE over a wider

temperature range. The Curie temperature also increases with nickel content as shown in Figure 6.1. More applications for Ni-Fe alloys can be investigated that require a uniform CTE value over a given temperature range.

6.4 ELECTRODEPOSITION

An electroplating process was developed to deposit the Invar-like alloy into high aspect ratio molds. In the process of electrodeposition for iron-nickel alloys, the iron content increases to a maximum and then decreases with an increase in current density (Grimmett, 1993). This behavior is characteristic of anomalous co-deposition. Electrodeposited alloys in the range ($\geq 60\%$ Fe and $\leq 72\%$ Fe) lie in the intermediate phase of mixed fcc and bcc structures. In the case of fcc alloys ($\leq 60\%$ Fe), the grain size decreases with increase in iron content, while for bcc alloys ($\geq 72\%$ Fe) the grain size increases with iron content.

The key element in the electrodeposition process was adapted from the technique developed by Namburi (2002). He first developed a pulse plating process for Ni-W alloy, and then modified the process to get the desired composition ratio for Invar.

The plating bath was prepared from reagent grade chemicals and distilled water. A sulfamate/sulfate bath was selected based on the previous work done by Namburi. Sodium Lauryl sulfate was added as a surfactant, ascorbic acid was added to prevent oxidation of ferrous ions, and saccharin acted as a stress reducer. Chloride salts used in the first generation process in the electroplating bath were replaced by sulfate salts and more iron salt was added to achieve composition of Invar. The composition of the bath used is given in Table 6.1. The bath was operated at 40°C and a pH of 2, which was adjusted periodically with sulfamic acid, every 24 hours. Electrodeposition was carried

out under controlled hydrodynamic conditions. A piece of platinized titanium was used as the anode. Pulse plating was performed at a duty cycle of 0.25 ('On' time of 10 seconds and 'Off' time of 30 seconds) and also with a duty cycle of 0.2 ('On' time of 10 seconds and 'Off' time of 40 seconds) at 8.5 mA/cm². It was found that the composition of the deposit was more uniform in the latter case.

Pulsing helped in the growth of uniform deposits in the recess. The plating resulted in successful growth of shiny and reduced stressed Ni-Fe micro posts. An SEM image of the Ni-Fe micro posts is shown in Figure 6.3.

The percent composition of iron in the deposit was sensitive to the composition of iron in the solution. A deposit of 58-wt % Fe was obtained with the 0.147 M FeSO₄ and a value of 64 % Fe was obtained with 0.155 M FeSO₄ (Figures 6.3(a) and (b)). The 64-wt % Fe is significant since it is the composition where the lowest CTE occurs in bulk material.

6.5 PERFORMANCE MEASUREMENT OF INVAR ELECTRODEPOSITION

6.5.1 TEST SAMPLE PREPARATION AND RESULTS

A copper plate was taken as an electroplating base for the preparation of the test samples. PMMA (500 μm) was bonded using the PMMA glue described in Chapter 5.

Table 6.1 Composition of Ni-Fe Electroplating Bath

Chemical	Molar Concentration
Nickel Sulfamate	0.72 M
Ferrous Sulfate	0.155 M
Boric Acid	0.5 M
Sodium Lauryl Sulfate	0.001 M
Ascorbic Acid	0.0011 M
Saccharin	0.008 M

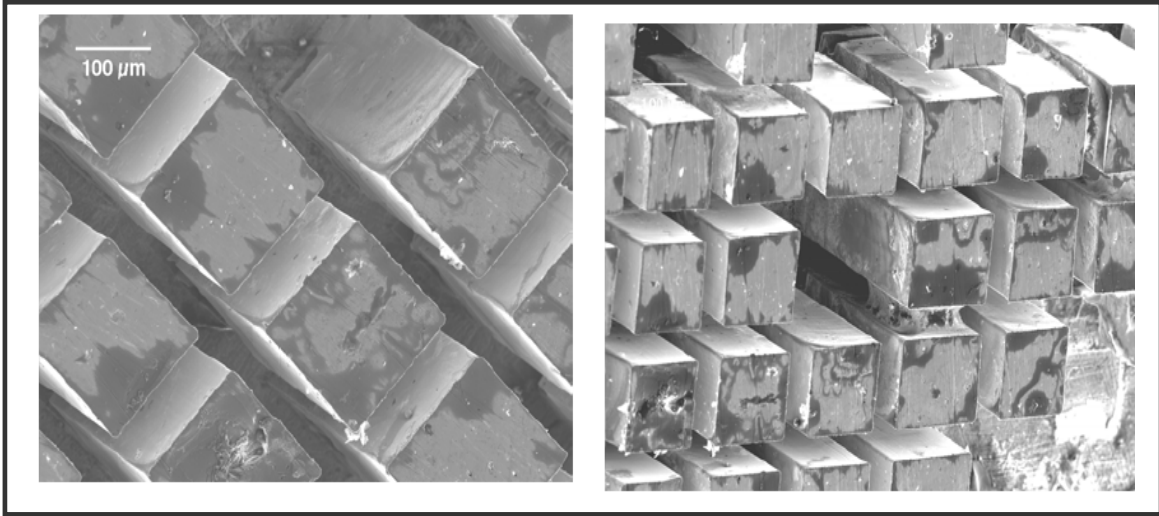


Figure 6.3(a & b) Stress-free Invar posts 150 μm X 150 μm and 250 μm deep obtained by pulse plating (Namburi, 2002)

The sample was exposed using a titanium mesh at the XRLM-3 beam line. The resist was developed to produce posts with 150 μm x 150 μm dimensions. Invar was electroplated as described in Section 6.4.

The sample was overplated, polished, and lapped. Samples were prepared and then cut to reveal the cross-section. The cut piece of the sample with the copper substrate and the posts, was set in an epoxy-based resin and left over night to cure. The mold was polished to reveal the structures and finely lapped. Wavelength Dispersive X-ray Spectrometer (WDS) analysis (spot size 1 μm) was performed to ascertain the composition of the Ni-Fe. Figures 6.4 (a) and (b) show the percentage of Ni-Fe along a height of 150 μm . The measurements were taken with 27 equally spaced intervals of 5.56 μm .

Figure 6.4(a) shows the atomic proportion of Ni and Fe from the bottom of the post to the top. The composition ratio of Ni to Fe is fairly uniform with an average Ni % of 36.64 and 63.35 % of Fe. Pulse plating approach with longer ‘OFF’ time, helped to

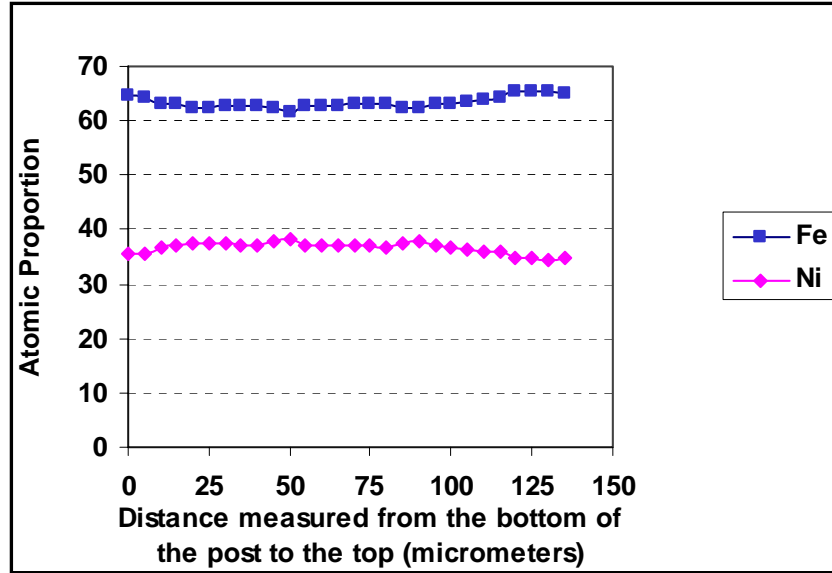


Figure 6.4(a) Atomic proportion of Ni and Fe in Invar (500 μm post).

obtain a uniform composition ratio. The alloy composition was found to be more uniform by applying duty cycle of 0.2 than compared to 0.25.

Figure 6.5 exhibits the atomic proportion of Ni and Fe obtained by square-wave current (Datta, 2001). The ratio of Ni and Fe is less uniform and out of proportion with

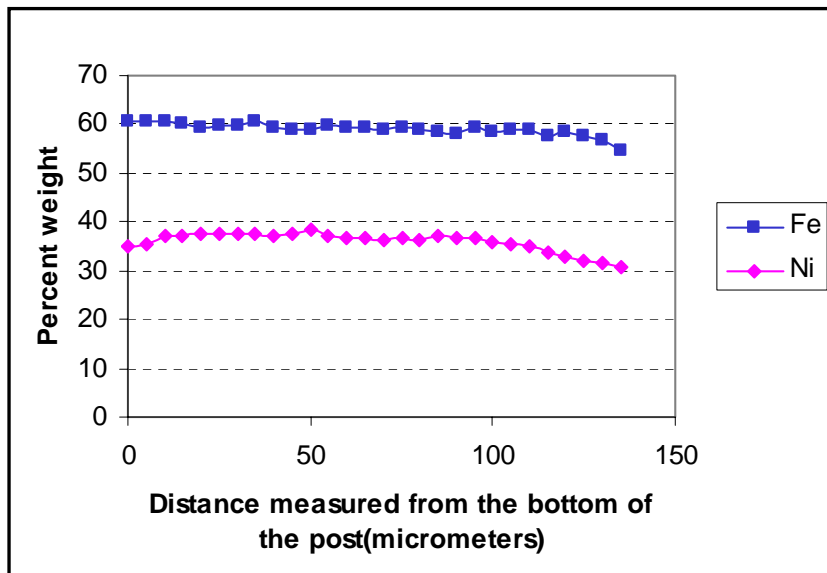


Figure 6.4(b) Weight composition of Ni and Fe in the sample Invar posts.

the desired results. This deviation is attributed to the mass transport effects that dominated due to high aspect ratio of the electroplated samples. There was insufficient time for the gases liberated due to side reactions to escape and the alloy to be plated.

6.5.2: CTE MEASUREMENTS

The electroplated samples were sent for CTE measurement. The tests were performed at Stork Technimet (New Berlin, WI). The test sample consisted of Invar-like posts with copper as an electroplating base. A 0.05 N loaded probe was used to measure the value of CTE for the post. A thermogram was plotted for temperatures between 25°C to 300°C, as the temperature sensor was to operate in this temperature zone. The heating rate applied was 5 °C/min. The average CTE value obtained for Invar-like alloy is given in Table 6.2. The measured CTE value was found to decrease with an increase in

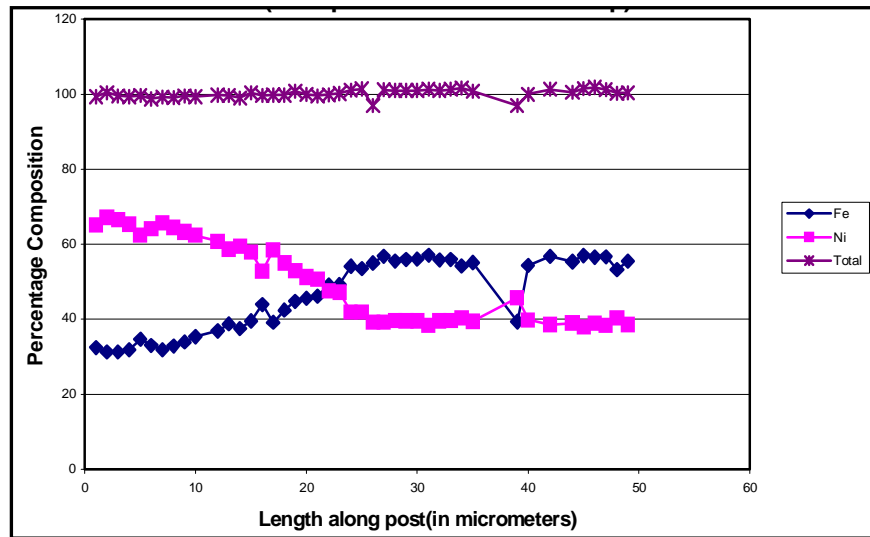


Figure 6.5: Atomic proportion of Ni and Fe (Datta, 2001).

temperature. Only a few samples have been plated, and tested, so the process is not completely understood. Annealing could be a cause for the deviation of the CTE value.

6.5.3 ADVANTAGES OF PULSE PLATING

The pulse plating technique was found to be effective for electroplating Invar. The composition of Invar was more uniform throughout the length of the post. In the first generation process the electroplated Invar-like alloy had a non-uniform composition ratio of Fe to Ni (Figure 6.4(a) as compared to Figure 6.5). This was attributed mainly due to the plating approach. In this approach, the hydrogen gas that is released as a side reaction does not find enough time to diffuse or seep out of the deep micro-posts. Whereas in a pulse plating approach, a longer 'OFF TIME' is set, this allows the hydrogen gas to escape and the electrodeposition process to be more uniform. This helps the metal ions to be replenished in the plating solution in the recesses.

In a pulsed plating approach, the pH near the cathode is increased because the short pulses of high current density attract hydrogen ions which move much faster in the electrolyte than the OH⁻ ions trying to escape (Puipe, 1986). During electrodeposition this gets trapped into the alloy or adsorbed on the surface of the micro-posts. It can seriously reduce the ductility and load-bearing capacity, by way of cracking and brittle failures at stresses below the yield stress of susceptible materials. In the case of direct current plating this problem is more serious than pulse plating.

Pulse plating also helps in reducing the stress caused during plating. The electroplated posts were not brittle and had very little to no damage due to hydrogen embrittlement (see Figure 6.3 as compared to Figure 6.6). In dc-plating, constant current

Table 6.2 CTE of Invar (Stork Technimet, Inc., WI).

No.	Temperature Range (°C)	Invar Sample
1	30-75	17.8
2	115-200	13.1
3	265-300	6.24

is used, and the rate of arrival of metal ions depends on their diffusion coefficient (electrode- to- part spacing and agitation). With pulse-current, modulated current waveforms are used to get a better leveling of the deposit, and to minimize the porosity and contamination (Puipe, 1986).

6.6 SUMMARY

Invar, due to its low CTE value has a growing demand in many industrial applications. Invar is a 36% nickel-64% Fe alloy with a very low coefficient of thermal expansion, near zero below temperatures up to of 300°C. Above 300°C the yield strength decreases rapidly. This means that during solidification and cool-down of electro-deposited Invar no elastic energy originating from thermal stresses can be stored in the material, because down to 300°C the matrix is too soft to store a significant amount

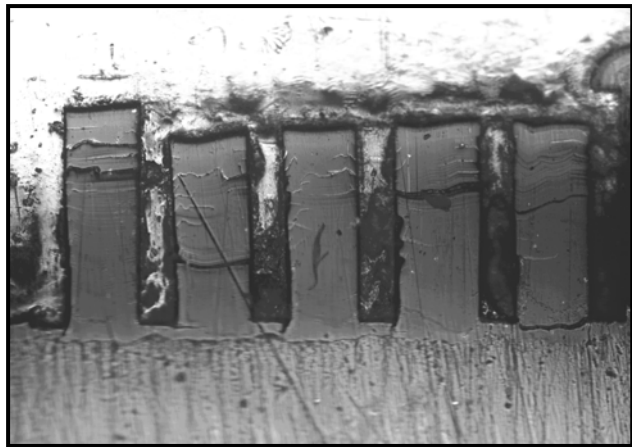


Figure 6.6: Electroplated post of Invar by square-wave plating, (Datta, 2001).

of elastic energy. Below this temperature the thermal expansion coefficient is low enough to avoid the buildup of further residual stresses.

Electrodeposition of low CTE Invar was successfully achieved. This was done by varying the percentage of ferrous sulfate and adopting a pulse plating cycle approach rather than direct plating. The initial test samples consisted of 150 μm X 150 μm posts, 500 μm in height. SEM analysis validated the percent ratio of Ni: Fe from bottom of the post to the top. The ratio was consistent with the desired ratio of Ni: Fe with 36:64.

In order to increase the temperature workability range for Ni-Fe alloys, the percent of nickel can be increased at the same time maintaining the CTE value within the desired limits. For higher uniform temperature workability the percent of nickel can be increased to 48 % from 36 %, but at the same time sacrificing the low CTE value associated with Invar. Cobalt can be added to increase the working temperature of the alloy. More applications can be investigated to in this regard.

7. EXPERIMENTAL RESULTS

A series of tests were performed on the recurve structures obtained from the release of the structures to experimentally measure the deflection characteristics with a rise in temperature.

7.1 INTRODUCTION TO THE DYNAMIC MECHANICAL ANALYZER (DMA)

The deflection of the released recurve structures were experimentally determined using a DMA (Q 800 Series Model, TA Instruments, New Castle, DE). It can be used to measure the mechanical properties of materials as a function of time. It provides different loading modes including dual cantilever, 3-point bending, tension, compression, and shear. The temperature can be varied from $-150\text{ }^{\circ}\text{C}$ to $600\text{ }^{\circ}\text{C}$. The deflection is measured with the help of a force transducer (18 N to 0.00001 N) by optical means. The sensitivity of the measurement of deflection values vary from $\pm 0.5\text{ }\mu\text{m}$ to $10,000\text{ }\mu\text{m}$. The device also provides for various heating rates from 0.1 to $10\text{ }^{\circ}\text{C}/\text{min}$.



Figure 7.1: Dynamic Mechanical Analyzer (Q 800 Series Model, TA Instruments, New Castle, DE).

7.2 EXPERIMENTAL SETUP

The experimental setup is shown in Figure 7.1. A 3-point bending clamp was used to measure the deflection produced. The test device with dimensions 8000 μm length and cross-sectional area (200 μm x 500 μm) was loaded. The sample dimensions were input to the device and adjusted in order for the force tip to be in contact. The clamp with the fixture was insulated and heated in a furnace. The jig used for the test procedure is shown in Figure 7.2.

The device was loaded at room temperature and heated from 25 $^{\circ}\text{C}$ to 300 $^{\circ}\text{C}$ since that was the working range of the temperature sensor. The input temperature function is shown in Figure 7.3.

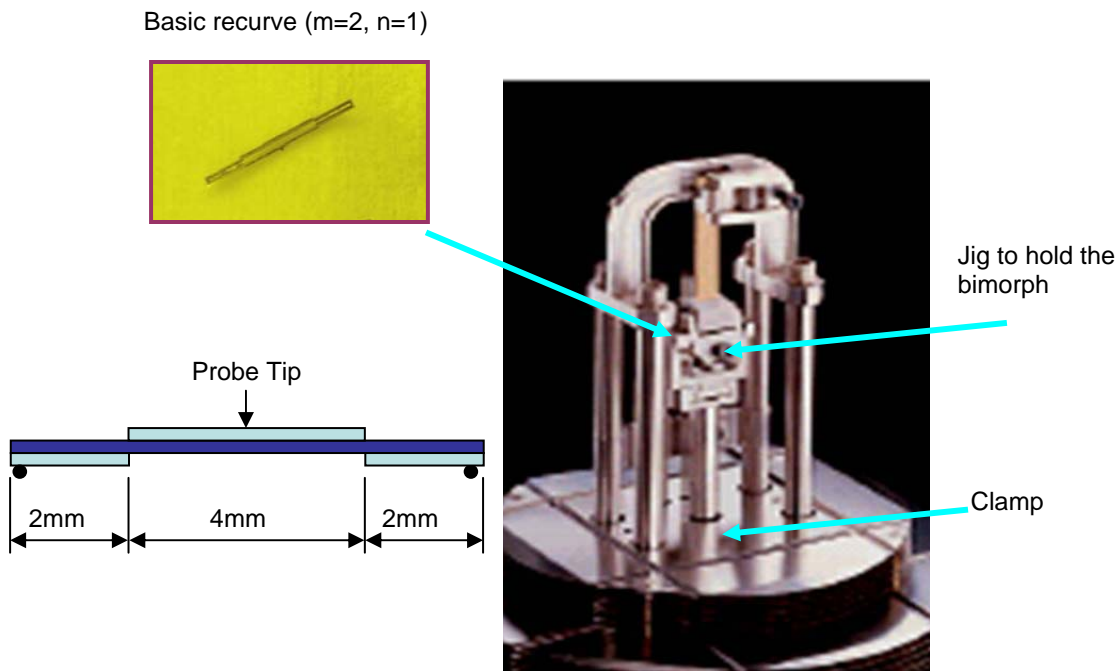


Figure: 7.2 3-point bending clamp.

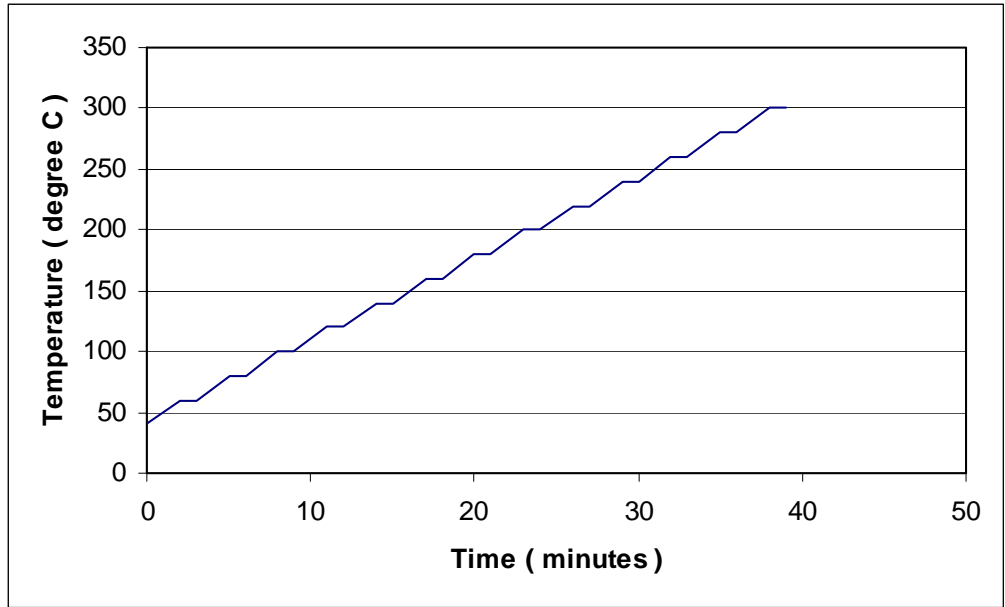


Figure 7.3: Plot of time vs. input temperature (DMA).

The sample was heated to the maximum temperature of 300°C over a period of 0.67 hours and the deflection values were determined. Two samples with the same nominal dimensions of length, width and height were tested in this temperature range. The temperature was increased with ramp input of 20°C rise over 2 minutes and then held constant at that temperature for 1 minute.

7.3 TEST RESULTS AND DISCUSSIONS

Samples 1 and 2 were heated to a maximum temperature of 300°C. The temperature was held constant for 1 min at the base of the ramp input in Figure 7.3. The raw data values for deflection obtained for Samples 1 and 2 are shown in Appendix F. A representative raw data plot for deflection values obtained for Sample 1 is shown in Figure 7.4. At each temperature there are 18 negative values of deflection. In order to obtain a unique deflection value at a particular temperature the raw data has to be processed. The entire data was made positive for a positive value of deflection. Now, for

each value of temperature, one may either take the final value of deflection at a particular temperature or the maximum value or may even take the average of all the deflection values. Looking at the table of raw data in Appendix F, it is clear that the final value of deflection is not a good choice, because in certain cases the final value is less than the preceding value for deflection for a lower temperature. For instance, the final value of deflection ($36.75 \mu\text{m}$) for a temperature of 160°C is less than the value at 120°C ($42.68 \mu\text{m}$). On the other hand one may decide to choose the maximum value of deflection at a particular temperature as a representative value of deflection at that temperature. However taking the average value of all the deflection values at a particular temperature gives us an unbiased result. The average of these readings were taken and plotted as shown in Figure 7.5 and Figure 7.6.

The values for deflection were found to increase linearly with temperature to a

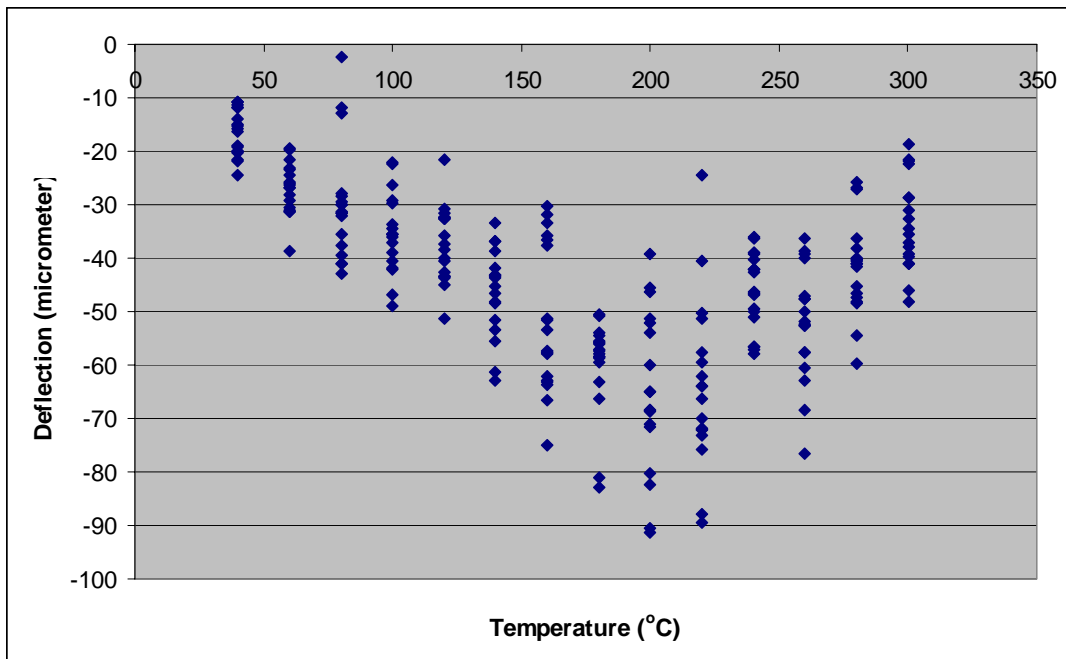


Figure 7.4 Representative raw data plot for Sample 1.

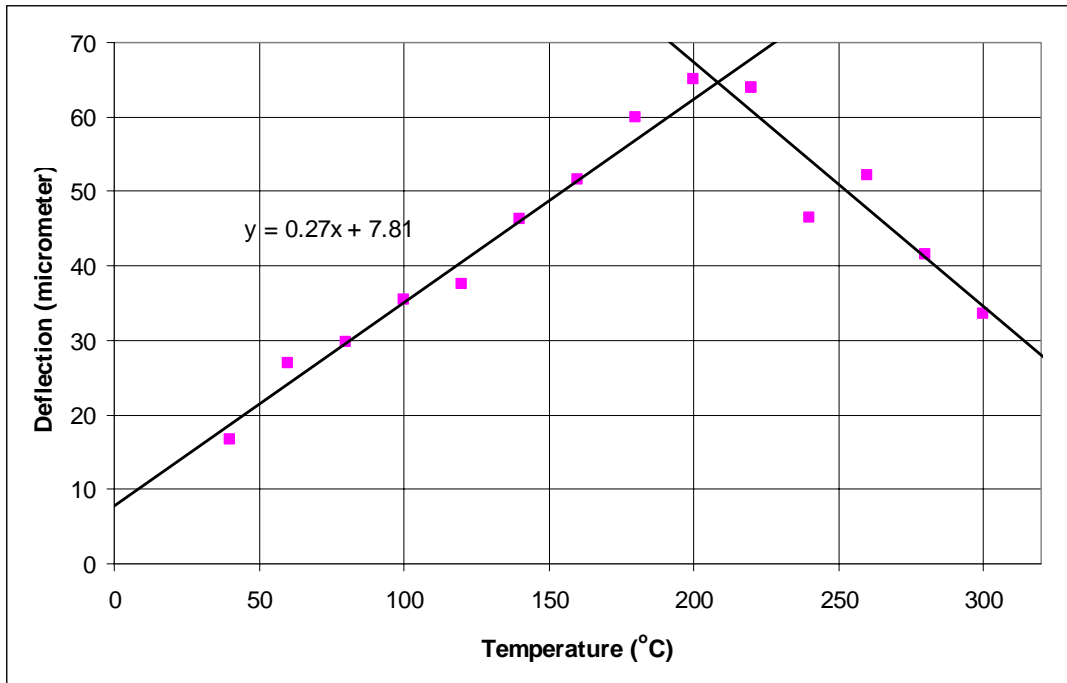


Figure 7.5 Plot of average temperature versus deflection (Sample 1).

value of 210 °C and then decrease with temperature. The maximum deflection obtained was 64 μm. For Sample 2, the maximum deflection of 59 μm, was found at 200 °C. In both the tests, the value of deflection increased from 40 °C and stopped between 200°C – 220 °C.

After collecting the data up to 300°C, the samples were cooled gradually in the furnace to room temperature over a period of 2 hours. The samples (bimorph) were still rigid and the beams were found to be intact, but they had undergone plastic deformation. The deformation of the sample is not completely understood but can be investigated with further research into the intrinsic structural analysis of the deformed sample.

The deflection values noted not only depend on the difference in CTE values of nickel and Invar over the range of temperature but they are a net effect of many factors including the constraints imposed by the layout of the recurve structure, the fabrication steps involved, and the temperature variation existing inside the furnace.

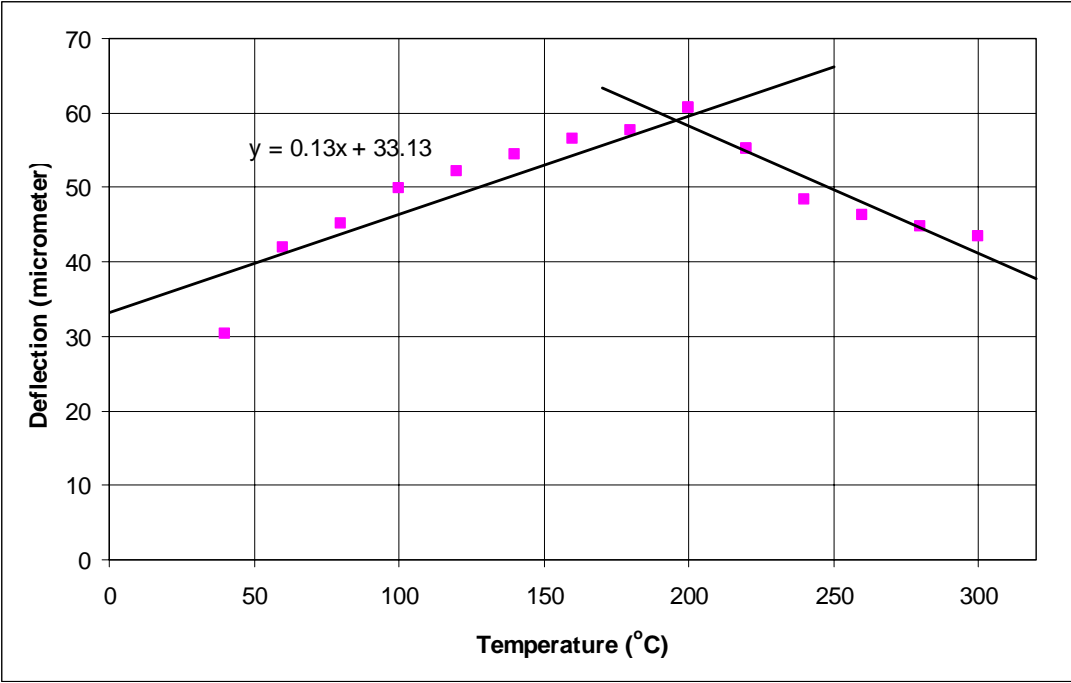


Figure 7.6 Plot of temperature versus deflection (Sample 2).

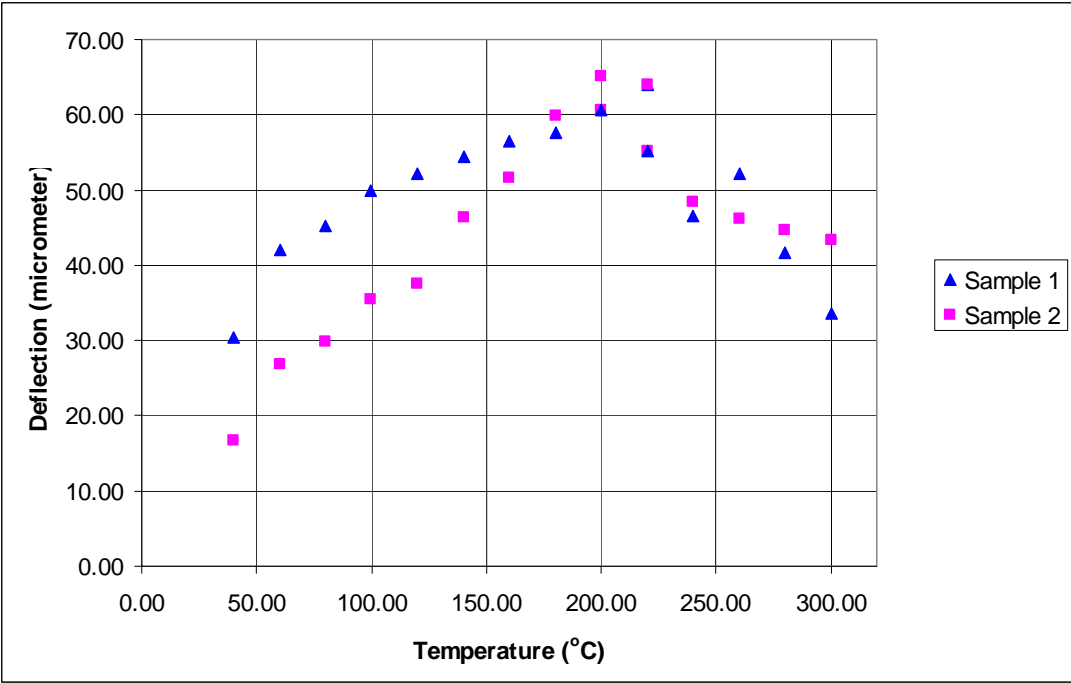


Figure 7.7 Comparative plots for Sample 1 and Sample 2.

Figure 7.7 gives a comparative plot for both of the test results. The slope of deflection values obtained for Sample 2 is similar to those obtained for Sample 1. Both the curves take a downward slope after reaching the high temperature range (between 200°C – 300°C). The deflection of the bimetallic is proportional to the difference in CTE values, based on Equation (36). It appears that the difference in CTE values increases with temperature until a range of 200°C – 220°C , but with further rise in temperature there is a negative slope. There is a linear trend of the slope in the negative direction, which shows that in the higher temperature range the deflection is proportional to the negative of the difference in CTE values. In other words the CTE of Invar is larger than the CTE value of Ni. This justification can be validated based on CTE values of Ni at higher temperatures ($14.4 \times 10^{-6}/^{\circ}\text{C}$, Table B.2, Appendix B). Testing of more samples would give a better picture of the transition of the deflection with temperature and thereby to get an improved curve based on the deflection values to determine the calibration curve for the temperature sensor. Investigation of the variation in CTE values of electroplated Ni and Invar with increasing temperature may help in a comprehensive analysis of the above mentioned behavior.

7.4 COMPARISON OF ANALYTICAL, NUMERICAL AND EXPERIMENTAL RESULTS

Figure 7.8 shows a comparative plot of the deflection obtained at various temperatures in the range from 40°C to 300°C . There is an increasing trend with temperature for all the results obtained to a temperature rise of 300°C except for the experimental results for samples 1 and 2, show a marked decrease in deflection with temperatures above 210°C .

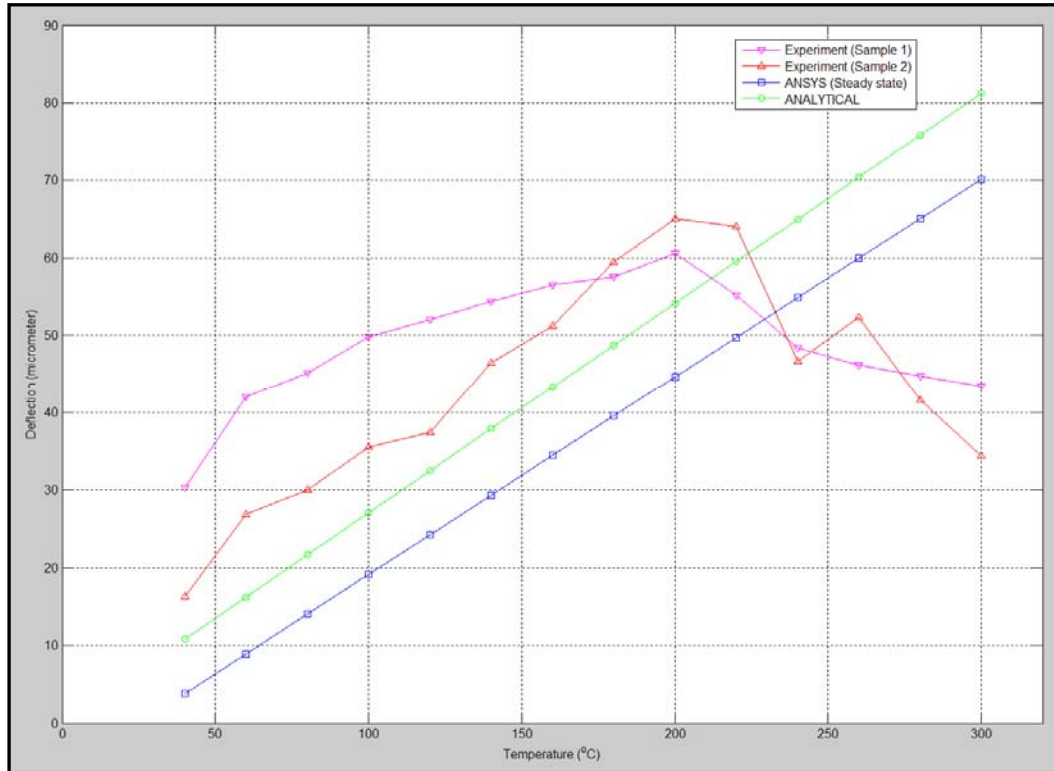


Figure 7.8 Comparative plots for sensor deflection.

The analytical and numerical steady state analysis results show an increasing linear trend, from 40°C to 300°C. For these analyses the thermo-mechanical properties were assumed to be invariant with temperature.

The results plotted have similar slopes with a mean difference of 6 µm in the deflection. For the analytical calculations, the recurve was based on a continuous model and an error of 3% was introduced in the equation derivation. Bulk material values were taken as input for the thermo-mechanical properties.

Experimental results were comparable to a temperature range of around 195°C to 220 °C, after this temperature the experimental results no longer show the increasing trend. The deflection value decreases after a further temperature rise to 300°C. The

deviation of the experimental results from the analytical and numerical results can be explained based on the net effect of a number of factors.

The X-ray mask for the device was made with 10 μm overlap between the two layers. In the analytical and numerical model these were assumed to be as connected side by side. There may have been deviation from the actual dimensions of the device as shown in Figure 7.9.

The recurve array structure was fabricated by a series of steps. The actual dimensions of the recurve after release were based on the net error introduced in these processes (mainly those introduced by X-ray exposure which has a maximum tolerance of $\pm 1.63 \mu\text{m}$).

The deflection of the sample is primarily based on the difference in CTE values, the greater the difference, the greater the net deflection. These are dependent on temperature, but for analytical and numerical calculations were considered as constant.

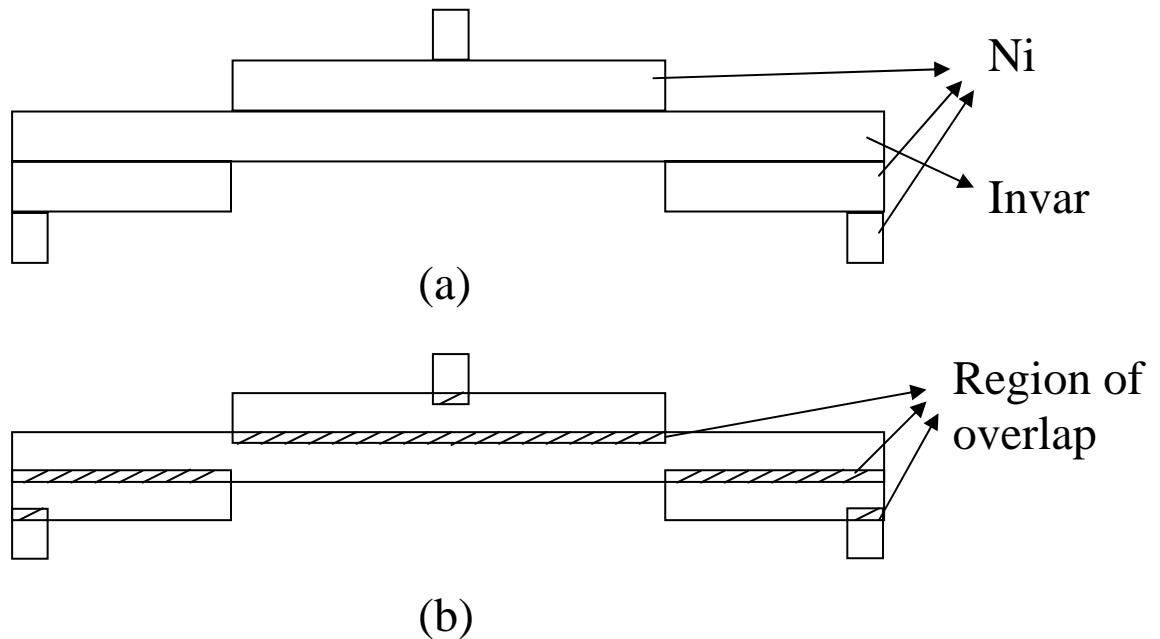


Figure 7.9 Schematic of a 2 x 2 bimorph array: (a) as considered for analytical and numerical analysis, and (b) as per design on the mask.

The deflection of the device was found to increase and after a temperature of around 220 °C, it decreased with temperature. This has been attributed to the Curie effect (Section 6.2). The low expansion property of Invar ceases to exist and the difference in CTE decreases, resulting in the decreasing values of deflection and with further increase in temperature the CTE of Invar is dominant over nickel leading to the negative deflection observed. The deflection value in the higher temperature range is not completely understood due to lack of data for electroplated Ni and Invar at such temperatures.

A region of overlap is introduced in the design of the recurve array. This region imposes a structural constraint on the device in all the three axes. In this region of overlap the thermomechanical properties are difficult to predict. However, in the analytical model, the contact surface is limited to the cross-sectional area between the two bimetallic strips.

A region of overlap is introduced in the design of the recurve array. This region imposes a structural constraint on the device in all the three axes. In this region of overlap the thermomechanical properties are difficult to predict. However, in the analytical model, the contact surface is limited to the cross-sectional area between the two bimetallic strips.

7.5 SUMMARY

The recurve structures fabricated by the second generation process were tested for thermomechanical properties by using DMA. These were heated from room temperature to 300°C. Two samples were tested and deflection values were plotted with temperature. The deflection values increased from room temperature to 200°C and then in the range

between 200°C – 300°C, the deflection values decreased. In both the samples similar trend in slope was observed. The deviation in slope at higher temperature range was probably due to the higher CTE values of Invar than nickel. It is recommended to test more samples to get a better idea of this behavior.

Analytical and numerical results were found to have similar slopes with a mean difference of 6 μm in the deflection. The deflection values from the experimental results show a negative trend in slope at higher temperature range (200°C – 300°C). The deviation can be attributed to the overall effect of a number of factors including alignment error due to X-ray exposure, a region of overlap provided in the design of the X-ray mask, variation of the thermomechanical properties with temperature and other machine and handling errors.

8. CONCLUSIONS AND RECOMMENDATIONS

Thermal actuators based on bi-metallic effect have been used for a variety of microsystem applications. In this thesis thermal recurve elements were successfully fabricated and tested for deflection. Analytical and numerical simulations were performed and the results were compared to the experimental methods. The results obtained are discussed in the sections below.

8.1 SUMMARY OF RESULTS

The results in this study may be summarized as follows;

In this thesis, the idea of using a bimetallic strip in the form of recurve architecture as a temperature sensor (or temperature measuring device) for downhole monitoring was investigated. The first phase of work demonstrated the feasibility of a thermomechanical actuator as a temperature sensor for maximum temperature measurements. A detailed plan was outlined for the concept, design and fabrication of the temperature sensor. Prototypes of the device were microfabricated and tested for thermomechanical properties. Further work can be extended to discrete/continuous monitoring.

Analytical system models were developed to perform parametric analysis. Models developed by Timoshenko for a bimetallic strip were used to determine the radius of curvature. Length of the bimetallic beam was plotted against the temperature rise to get the deflection produced. All of the parameters (length, temperature and deflection) were combined into a single plot to determine the deflection for any length of the beam for any given rise in temperature. The maximum deflection obtained for recurve of length 8000 μm with cross-section area (500 μm X 100 μm) was 54.17 μm at 200°C. The blocking

force was estimated to be 0.2 N. Analytical and numerical (ANSYS, Version 5.7, ANSYS, Inc., Canonsburg, PA) solutions were comparable at various temperature inputs to the system.

Self-weight analysis was performed to ensure that the recurve array was stable enough to support the recurve array structure. The maximum deflection obtained was 1.25 μm . The value of stress obtained (279 MPa) was below the yield stress value of nickel (810 MPa). The value of time constant was estimated to be 1.44 seconds.

A new and improved idea for reducing the alignment error for the bimetallic layers of the recurve was developed. The error associated in the first generation process by manual alignment was $\pm 10 \mu\text{m}$. There were two alignment processes and thus the net error was $\pm 33 \mu\text{m}$. The second generation process incorporated both the pattern and the markers in one X-Ray mask. PMMA was completely developed (aspect ratio : 1:50) to generate the alignment markers that played an important role in reducing error, though there was some error introduced due to high aspect ratio markers (2.75 μm), which introduced slope in the developed walls of PMMA(Chapter 5). These alignment patterns were handled carefully during subsequent steps of plating and polishing. It was established that these remained stable and were found not to buckle during the entire set of processes that followed. The net error for this process was 8.5 μm s.

The second generation process followed a well-defined microfabrication cycle and the process was a success. The recurve array was effectively etched out and tested for thermo-mechanical properties.

Electroplating of Invar (Ni 36% & Fe 64%) was successfully achieved. The plating cycle was observed for various duty cycles and a duty cycle of 10:40 was

developed to produce the desired results. Stress produced during plating was reduced by adding a sufficient amount of saccharin to the plating bath and by applying a pulse plating approach. Both the plating sequences of nickel and Invar were successfully executed.

Thermomechanical testing was performed by using DMA (Dynamic Mechanical Analyzer; Q 800 Series, TA Instruments, Houston, TX). The recurve pattern was tested for temperatures ranging from 40 °C to 300 °C. Temperature was increased in steps of 20 °C and then kept isothermal for one minute during each step (heating rate: 10 °C /min). The maximum deflection of 65.08 μm was obtained at 200 °C.

The Curie effect of Invar was demonstrated in the experimental results. This effect causes variation in the value of CTE. The CTE value of Invar increases with temperature until it reaches the Curie point, after that there is a steep increase in slope. The bimetallic beams were made of nickel and Invar. The amount of deflection was directly proportional to the difference in CTE's of the constituent elements. At temperatures above Curie point this difference was reduced. The deflection curve obtained from the DMA analysis for the recurve confirmed this principle for temperatures above 200 °C .

The plot of temperature versus deflection was compared for analytical, numerical and experimental results. The value of deflection increased with temperature. Up to a temperature of 210°C, after that the plot of experimental results showed deviation in values. It was established that this deviation was due to the Curie effect. In experimental and numerical simulations the Curie effect was not considered.

8.2 RECOMMENDATIONS TO THE FUTURE WORK

As the applications of microelectromechanical systems extend to high temperatures, there is an increasing need for characterization of thermomechanical properties. Limitations were imposed on the models based on the data collected for thermomechanical properties. These values were obtained from the bulk value of materials. The properties include Young's modulus, yield strength, and thermal expansion coefficient as a function of temperature. The accuracy of these devices depends on the accuracy of determination of temperature related properties of the materials

Properties of plated Invar can be increased by cold working and also by annealing which helps in reduced stress and higher tensile strength (Marsh, 1938). Elements can be added to the plating solution in order to improve the thermomechanical properties while maintaining the CTE. Cobalt when added would help in maintaining the Curie temperature over a low value of CTE (Marsh, 1938).

In the present X-ray mask the design features with $m=2$ (recurve layers in parallel) were incorporated into the pattern. As a step further other patterns with $m>2$ can be made and tested for thermomechanical properties. Thicker strips, with $t>100$ were found to be rigid. A better mask pattern can be developed with all the strips with equal thickness value. This would help in reducing the stress on the adjacent layer during plating and subsequently polishing the sample.

Invar has a low coefficient of thermal expansion over many other materials at cryogenic temperatures. So it can be used for a wide range of applications with low

temperature or near zero applicability. This would require redesigning the basic recurve to take into account the deflection produced at such temperatures.

REFERENCES

Agarwal, B., Broutman, L., "Analysis and performance of fiber composites", (1990), Second Edition, John Wiley and Sons, Inc.

Barnes, J.R., Stephenson, R.J., Welland, M.E., Geber, C., Gimzewski, J.K., "Photothermal spectroscopy with femtojoule sensitivity using a micromechanical device", (1994), *Nature*, 372:79-81.

Berner, A., "Electrodeposition of alloys", (1963), Volume II, Academic Press, Publishers.

Betteridge, W., "Nickel and its alloys", (1977), Industrial Metals Series, MacDonald and Evans Publishers.

Boley, B.A., Jerome, H.W., "Theory of thermal stresses", (1960), Krieger Publishing Company Malabar, Florida.

Busch-Vishniac, I.J., "Electromechanical sensors and actuators", (1998), Mechanical Engineering Series (Berlin, Germany), Springer Verlag, 207-247.

Chu, W.H., Mehregany, M., Mullen, R.L., "Analysis of tip deflection and force of a bimetallic cantilever microactuator", (1993), *Journal of Micromechanics and Microengineering*, 3:4-7.

Chu, W.H., Mehregany, M., "Microfabricated tweezers with a large gripping force and a large range of motion" (1994), *Proc. of Solid State Sensors and Actuators Workshop*, Hilton Head, SC, 100-107.

Datta, P., "Design and fabrication of a thermomechanical micro-actuator", (2001), Master's Thesis, LSU, Department of Mechanical Engineering.

Datta, P., Sathe, M., Namburi, L., Murphy, M.C., Podlaha, E., Acharya, S., "Design and fabrication of a thermo-mechanical micro-actuator for high temperature applications", (2001), presented at HARMST 2001, Fourth International Workshop on High-Aspect Ratio Micro-Structure Technology, June 17-9, Baden-Baden, Germany.

Datta, P., Sathe, M., Namburi, L., Podlaha, E.J., Acharya, S., Murphy, M.C., "Microfabricated bimetallic actuator", (2003) in *MEMS Components and Applications for Industry, Automobiles, Aerospace, and Communication II*, ed. S.W. Janson, Society of Photo-optical Instrumentation Engineers (SPIE), 83-94

David, L., Grimmett, M., Schwartz, A., Nobe, K., "A comparison of DC and pulsed Fe-Ni alloy deposits", (1993), *Journal of Electrochemistry*, 140(4):973-978.

Desta, Y.M., Murphy, M.C., Goldie, J., Kiley, J., Howatt, R., "Fabrication of micromachined resonating cylinder gyroscopes", (2001), presented at HARMST 2001,

Fourth International Workshop on High-Aspect Ratio Micro-Structure Technology, Baden-Baden, Germany, June 2001.

DiBari, G.A., "Nickel plating", (1997), *Plat. Surf. Finish.* 84, 8.

Donald, J.S., Reid, J.R., "Joule heating simulation of poly-silicon thermal microactuators", (1998), *Modeling and Simulation of Microsystems*, AFOSR (Air Force Research Laboratory, MA), 1-2.

Ervin, J. D., Brei, D., "Recurve piezoelectric-strain-amplifying actuator architecture." (1998), *IEEE Transactions on Mechatronics*, 3(4):293-301.

Faupel, J.H., Fisher, F.E., "Engineering design: A synthesis of stress analysis and material engineering", (1981), Second Edition Ed., Wiley and Sons, New York.

Figiola, R.S., Beasley, D.E., "Theory and measurement for mechanical measurements", (2000), John Wiley and Sons, Inc., New York.

Fritz, T., Leuerer, T., Krueger, C., Mokwa, W., Schnakenberg, U., "Mechanical properties of electroplated nickel", (2000), *Technical Digest Micro. Materials*, 3rd International Conference and Exhibition, Berlin, Germany, April 17-19, 752-55.

Fukuda, T., Menz, W., "Handbook of sensors and actuators", (1998), *Micro Mechanical Systems, Principles and Technology*, Elsevier.

Gere, J.M., Timoshenko, S.P., "Mechanics of materials", (1997), Fourth Edition, PWS Publishing Company, Chapman and Hall, London.

Goldstein, R.J., Chen, P. H., Chiang, H. D., "Handbook of heat transfer", Third Edition (1998), Editor: Rohsenow; W.M., Choi; Y. J. and Hartnett; J. P., 16.1-16.71.

Guckel, H., Klein, J., Christenson, T., Skrobis, K., Laudon, M., Lovell, E., "Thermo-magnetic metal flexure actuators", (1992), *Technical Digest, 1992 Solid-State Sensor and Actuator Workshop*, Hilton Head, SC, 73-75.

Guyer, Eric C. (Ed), "Handbook of applied thermal design", (1989), NY: McGraw-Hill

Harald, S., Alan, G.R., Brunnschweiler, A., "Fabrication and test of thermal vertical bi-morph actuators for movement in the wafer plane", (2001), *Journal of Micromechanics and Microengineering*, 11:306-310.

Hirano; T. and Fan; L.S., "Micromachining and macrofabrication process technology II", (1996), *The International Society for Optical Engineering (SPIE)*, 2879:252-259.

Hirano, T., and Fan, L.S., "Invar electrodeposition for MEMS applications", (1994), *Proceedings of the International Society for Optical Engineering (SPIE)*, 2879:252-259.

Holman, J.P., "Experimental methods for engineering", (2001), Seventh Edition, M C Graw Hill Publishers.

Izotov, V.I., Rusanenko, V.V., "Structure and properties of Fe-Ni-36 % Ni Invar after intense shear deformation", (1996), The Physics of Metals and Metallography, 87(3): 289-296.

Jerman, H., Terry, S., "Microfabrication and micromachining", (1997), 2, Handbook of Microlithography, Micromachining and Microfabrication, SPIE Optical Engineering Press, Editor: Choudhary. R.P., 379-427.

Jung, M., Choi, S.S., "Fabrication of bi-metallic cantilevers and its characterization", (1999), Surface Review and Letters, 6(9):1195-1199.

Junma, N., Guanxin, L., Kewei, X., "Yielding behavior of low expansion Invar alloy at elevated temperature", (2000), Journal of Materials Processing Technology:114(1):36-40.

Kamil, A.V., "The physics of submicron lithography", (1992), Micro-Devices, Physics and Fabrication Technologies, Plenum Press.

Lyshevski, S.E., "Electromechanical systems, electric machines and applied mechatronics", (2000), CRC Press.

Lyshevski, S.E., "Nano and micro-mechanical systems – fundamentals of nano and micro-engineering", (2001), CRC Press.

Madou, M., "Fundamentals of microfabrication", (1997), CRC Press, Boca Raton, FL., USA.

Manalis, S. R., Minne, S.C., Quate, C.F., " Two dimensional micromechanical bimorph arrays for detection of thermal radiation", (1997), Applied Physics Letters, 70(24):3311-3313.

Marsh, J.S., "The alloys of iron and nickel", Special Purpose alloys, McGraw Hill Book, Co., (1938), 1:45-55.

Moruzzi, V.L., "Theory of Invar", (1992), Solid State Communications, 83(9):739-743.

Namburi, L., "Electrodeposition of NiW alloys into deep recesses", (2002), Master's Thesis, LSU, Department of Chemical Engineering.

Puippe, J.C., "Theory and practice of pulse plating", (1986), American Electroplaters and Surface Finishers Society (AESF), Orlando, 50-55.

Romankiw, L.T., O'Sullivan, E.J.M., "Plating techniques", (1997), Microlithography, Micromachining and Microfabrication, 2:199-287.

Reithmuller, W., Benecke, W., “Thermally excited silicon microactuators”, (1988), IEEE transactions on Electron Devices, 35(6):758-763.

Schilfgaard, M.V., Abriksov, I.A., Johansson, B., “Origin of the Invar effect in iron–nickel alloys”, (1999), Nature 400:46-49.

Sharpe, W.N., McAleavey, A., “Tensile properties of LIGA nickel”, (1998), Proceedings of SPIE, Conference on Materials and Device Characterization in Micromachining, 3875: 130-137.

Song, Tae., Chul, K.K., “Elastic properties of ferromagnetic Invars”, (1992) Solid State communications, 83(5):391-394.

Sun, X.Q., Farmer, K.R., Carr, W.N., “A bistable microrelay based on two-segment multimorph cantilever actuators”, (1998), Journal of Micromechanics and Microengineering, 154-159.

Tada, H., Nieva, P., Zavracky, P., Miaoulis, I.N., Wong, P.Y., “Determining the high temperature properties of thin films using bi-layered cantilevers”, (1999), Materials Research Society Symposium; 546:39-44.

Takeshima, N., Fujita, H., “Ployimide bimorph actuators for a ciliary motion system”, (1991), Micromechanical sensors, Actuators and Systems, 203-209.

Technical information from www.micronas.com Dated: October 2003.

Technical information from www.vitar.com Dated: October 2003.

Technical information from www.allaboutcircuits.com Dated: October 2003

Technical Report (Nov 2001), Stork Technimet, Inc., (Report No: 0110-02661), New Berlin, WI.

Timoshenko, S.P., “Strength of materials”, (1955), Pt. 1, Third Edition, Mc Graw Hill Publishers, New York.

Timoshenko, S.P., “Theory of elasticity”, (1951), Mc Graw Hill Publishers, New York.

Timoshenko, S.P., “The collected papers”, (1953) McGraw Hill, New York.

The International Nickel Co., Inc “Nickel alloy steels”; Second edition, (1949), New York, N.Y, 40-50.

Wallrabe, U., Ruther, P., Schomburg, R.P., “Microsystems in medicine”, (1999), International Journal of Artificial organs, 21:137-146.

Webster, J.G., "Mechanical variables measurement, solid fluid and thermal", (2000), CRC Press, FL.

Yang, C.W., Goldstein, J. I., "Phase decomposition of Invar alloy - information from the study of meteorites" (1997), The Invar Effect: A Centennial Symposium, Edited by J. Wittenauer, The Minerals, Metals & Materials Society, 137-149.

Young, W., Budynas, R., "Roark's formulas' of stress and strain", (2002), Seventh Edition, McGraw-Hill, New York.

APPENDIX A

X-RAY MASK FABRICATION

A.1 GRAPHITE MASK

The process steps involved in making an X-Ray mask can be listed as:

1. **Cleaning:** Glass discs cut into 4" inch diameter circles are cleaned using acetone and IPA. Then they are dehydrated by placing in the oven at 90 degrees Celsius. Graphite (POCO graphite; density: 1.8g/cm^3) 200 microns thick are also cleaned using acetone and IPA and then dehydrated along with the glass discs.
2. **Bonding:** AZ 4620 resist (Hoechst Celanese Corp., Somerville, New Jersey) is spin coated on the glass disc at 2000 rpm for 20 seconds. It is then placed on a flat surface. Graphite disc is placed on the glass piece and then rolled on top to give a smooth bubble free adhesion with glass.
3. **Bake Cycle:** The sample is then baked by using the bake cycle shown below.

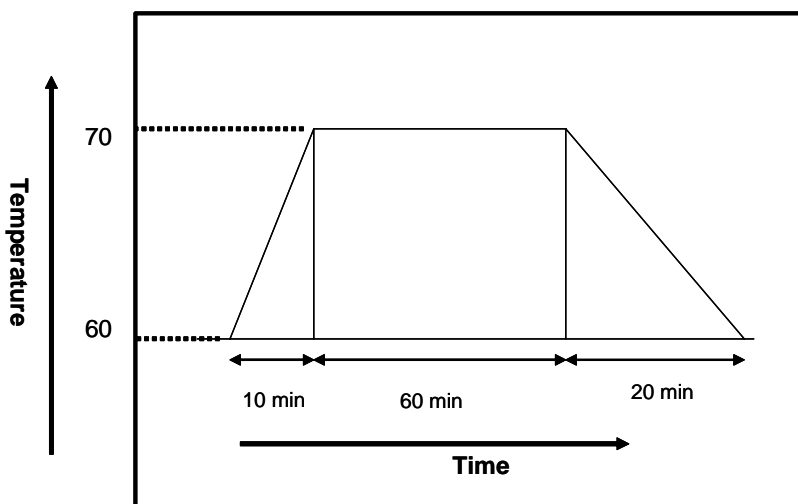


Figure A.1: Bake cycle of AZ 4620 resist

4. **Fly cut:** The sample is then fly cut to size it down to 150 micron-meters.
5. **De-bonding:** The sample is then de-bonded by placing it in acetone. Graphite separates out from glass. The graphite is then cleaned by acetone and IPA and then rinsed with DI water followed by dehydration bake.
6. **Soft bake:** SU-8 resist is spun coated on the graphite at 1250 rpm for 20 seconds. The sample is now ready for soft bake. Soft bake cycle is carried out as follows.

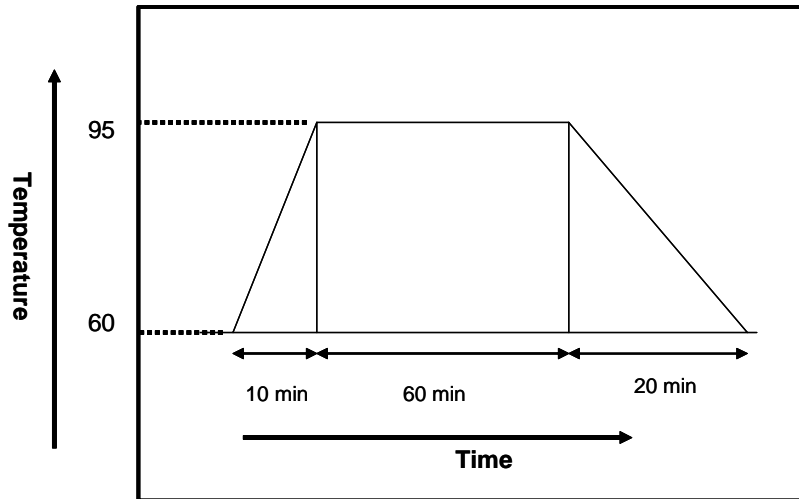


Figure A.2: Soft bake of SU-8

7. Exposure: After the soft bake the sample is exposed at intensity of 330 mJ/cm² using Oriol UV Exposure System.
8. Hard bake: The hard bake cycle is similar to the soft bake, with decrease in time to hold at 95 °C.

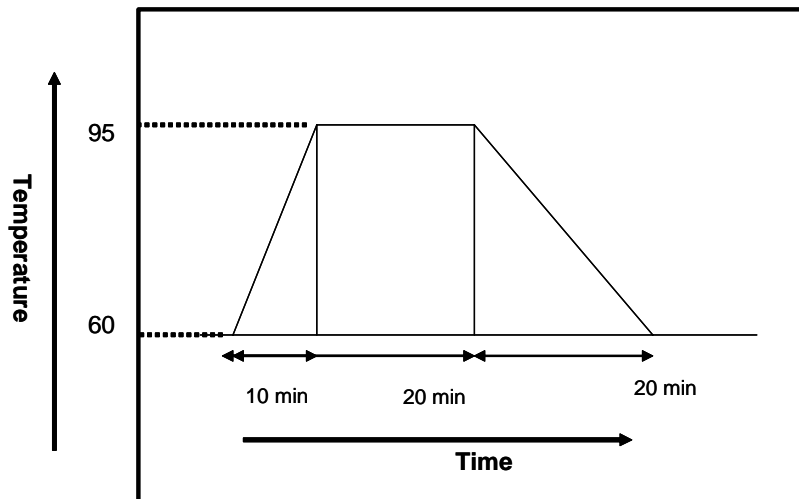


Figure A.3: Hard Bake SU-8

9. Developing cycle: SU-8 Developer (Microchem Corp., Newton, MA) is used for developing the pattern.
10. Gold electroplating: Gold is electroplated with a current density of 2mA/cm² after being cleaned in a plasma-asher.
11. The graphite mask is ready for X-ray exposure

A.2 KAPTON MASK

1. A kapton sheet is placed on Mylar and the stretching ring is attached to it. After resting for about 30 minutes with weights on it; the ring is stretched equally in all directions. It is baked in the oven at 86 °C for 30 minutes and cooled down slowly.
2. The ring is then stretched again and mounted on a standard NIST ring.
3. Chromium and gold layer is deposited on the kapton by e-beam.
4. SPR 220 (Microchem Corp., Newton, WI) is spun on Kapton; mounted on the ring at a speed of 1500 rpm for 40 seconds to get 10 microns of the resist. It is relaxed for 30 minutes.
5. Bake cycle follows the spinning cycle. The sample is baked in the oven at 100 °C for 25 minutes followed by a slow cool down process as shown in the figure below.

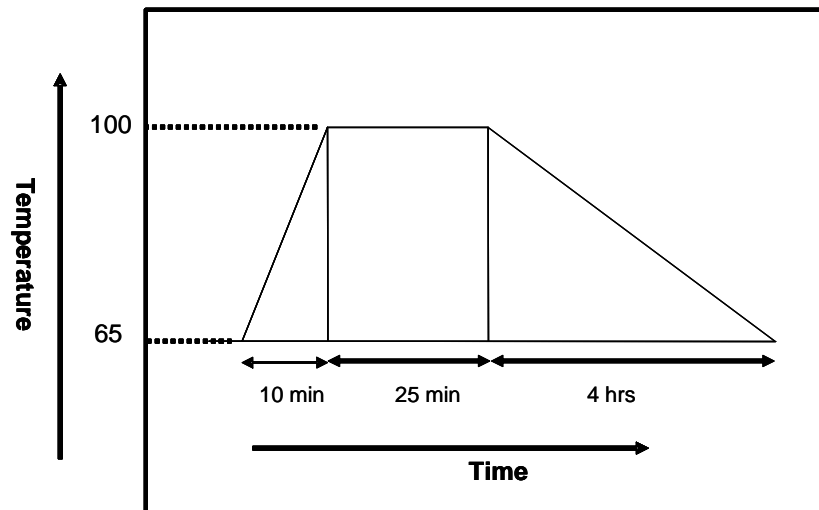


Figure A.4: Bake cycle for SPR 220

6. The pattern is exposed using Quintel Exposure station with a dose of 450 mJ/cm².
7. 2 baths of 50% MF-322 + 50% MF 321 developer are used for developing. The developer tray is mildly agitated during the development process. This is followed by a long rinse in distilled water.
8. Gold is electroplated with a current density of 2 mA/cm².

APPENDIX B

RECIPE AND DATA SHEETS

Table B.1: Nickel plating solution

Chemical	Chemical Formula	Amount g/l
Nickel Sulfamate	Ni (SO ₃ NH ₂) ₂ .4H ₂ O	450
Sodium Lauryl sulfate	C ₁₂ H ₁₂ O ₄ SNa	1.0
Boric acid	H ₃ BO ₃	37.5

Table B.2: Co-efficient of thermal expansion of nickel:

Temperature Range (°C)	Coefficient (K ⁻¹)
20-100	13.3 x 10 ⁻⁶
20-200	13.9
20-300	14.4
20-500	15.2
20-700	15.7
20-900	16.3

Table B.3: Thermal conductivity of Nickel

Temperature (°C)	Conductivity (W/m K)
25	92
100	83
300	64
500	62

Table B.4: Stress reducers for Ni-Fe Alloys

Method	Effect
Agitation	Ultrasonic agitation helps in reducing the stress produced during plating
Saccharin	Added in limited amount decreases stress, if exceeded reduces the percent deposition of Fe in the alloy
Addition of Iron salt	The value of stress increases about 2 kg/sq.-mm for each g/l increase of ferrous ions in the Sulfamate solution

(Reference: Table B.2, B.3 and B.4 – Betteridge; W, “Nickel and its alloys”, (1977), Industrial Metals Series, MacDonal and Evans Publishers)

Table B.5: Heat Capacity of various metals over a range of Temperature

Temperature (°C)	Iron	Cobalt	Nickel	Titanium	Copper
300	447	421.3	443.6	530.8	385.0
400	489	450.5	484.1	555.5	397.7
500	531	478.9	524	576.2	408.0
600	572	503.7	591	604.7	416.9
699.6	-	-	670	-	1
700	618	527.2 (a)	524	626.8	425.1
700	-	519.4 (b)	-	-	-
800	678	550.6	529	637	432.9
900	770	586.2	543	647.8	441.7
1000	1034	628	562	646.9	451.4
1042	1236	-	-	-	-
1100	829	-	-	-	464.3
1156	-	-	-	666.9 (a)	-
1156	-	-	-	617.9 (b)	-
1183	742 (a)	-	-	-	-
1183	607 (b)	-	-	-	-
1200	608	734	593	633.9	480.8
1394	-	1020	-	-	-
1300	-	-	-	-	506.5
1400	638	800	609	663.7	--

(Parker; E. R., “High temperature properties of metals”, (1951), American Society for Metals)

Table B.6 System planning and Corporation market survey (1999) with an estimate of 1996 product volume and a forecast of 2003(in millions of US \$)

MEMS device and applications	1996	2003
<i>Inertial measurement:</i> Accelerometer and rate gyros	350-540	700-1400
<i>Micro-fluidics:</i> Ink jet printers, mass flow sensors, bio-chip lab	400-500	3000-4450
<i>Optics:</i> optical switches, displays	25-40	440-950
<i>Pressure measurement:</i> Automotive, medical, industrial	390-760	1100-1250
<i>RF devices:</i> Cell phone components, devices for radar	None	40-120
<i>Other devices:</i> Micro relays, sensors, disk heads	510-1050	1230-2470

APPENDIX C

PERCENT COMPOSITION OF NICKEL AND IRON ALONG THE LENGTH OF THE POST

Table C.1 Element Weight percent of Electroplated Invar

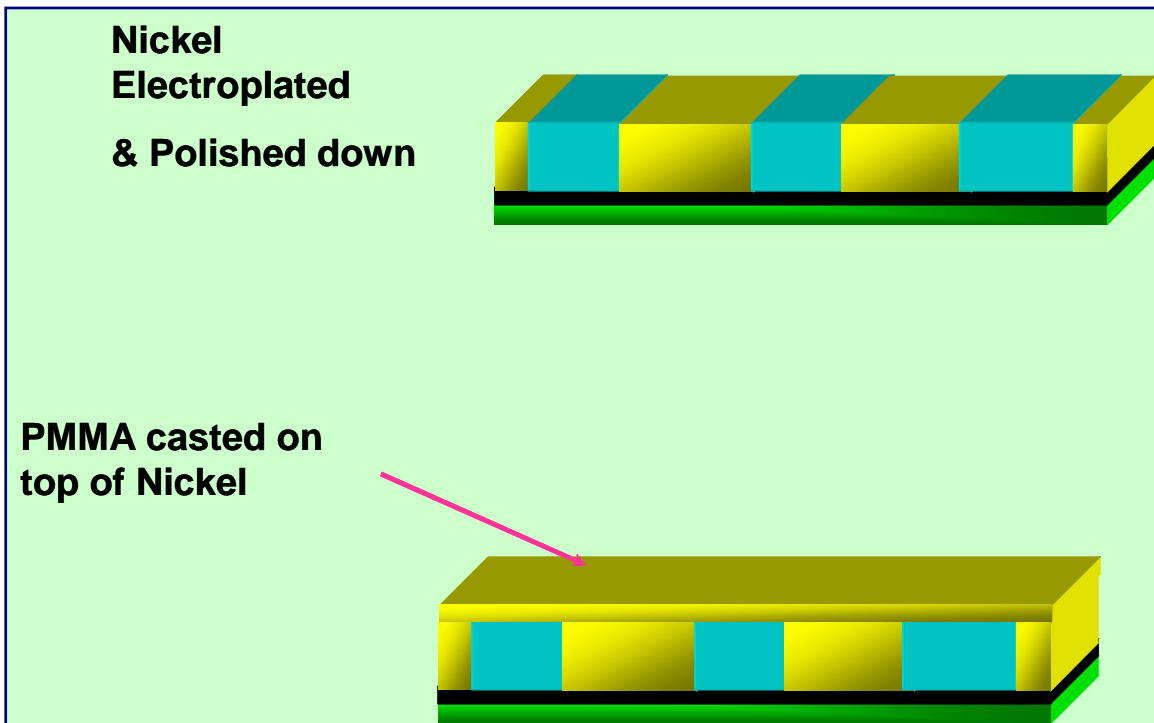
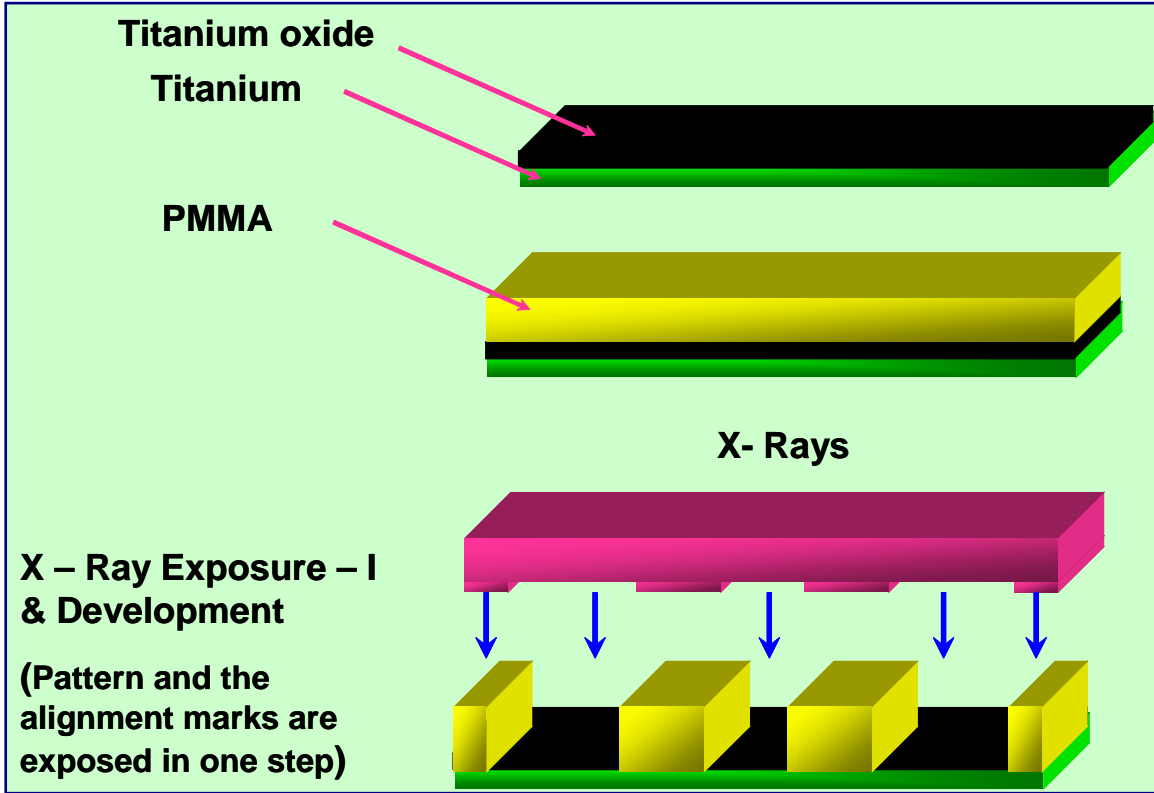
Element Weight Percent:				
Pt #	Distance	Fe	Ni	Total
All distances are measured from the bottom of the post to the top (μm)				
1	0	60.62	34.98	95.6
2	5	60.77	35.5	96.27
3	10	60.55	37.22	97.78
4	15	60.28	37.34	97.61
5	20	59.23	37.42	96.65
6	25	59.86	37.73	97.59
7	30	59.77	37.57	97.34
8	35	60.53	37.54	98.08
9	40	59.53	36.95	96.48
10	45	58.83	37.51	96.34
11	50	58.71	38.36	97.07
12	55	59.62	36.94	96.56
13	60	59.23	36.75	95.98
14	65	59.31	36.8	96.11
15	70	58.91	36.39	95.3
16	75	59.22	36.67	95.89
17	80	59.04	36.23	95.28
18	85	58.53	36.96	95.48
19	90	58.01	36.9	94.91
20	95	59.24	36.63	95.87
21	100	58.65	35.94	94.59
22	105	58.91	35.37	94.27
23	110	58.91	34.88	93.79
24	115	57.75	33.81	91.56
25	120	58.66	32.81	91.47
26	125	57.5	32.01	89.52
27	130	56.59	31.46	88.05
28	135	54.82	30.77	85.59
Average Value		58.985	35.90857	

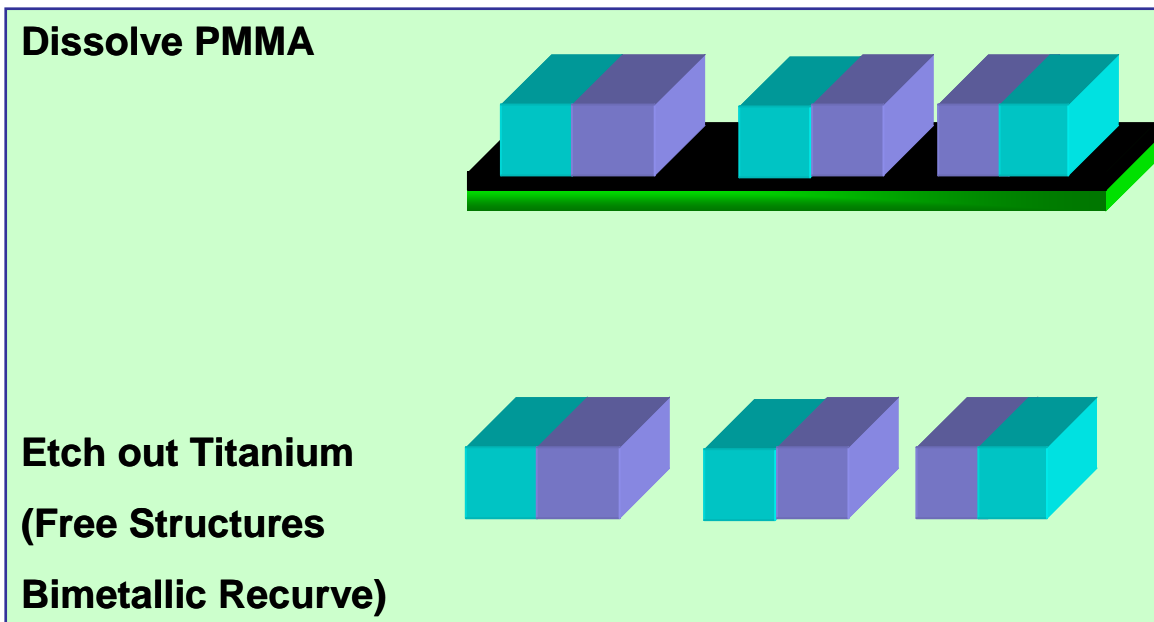
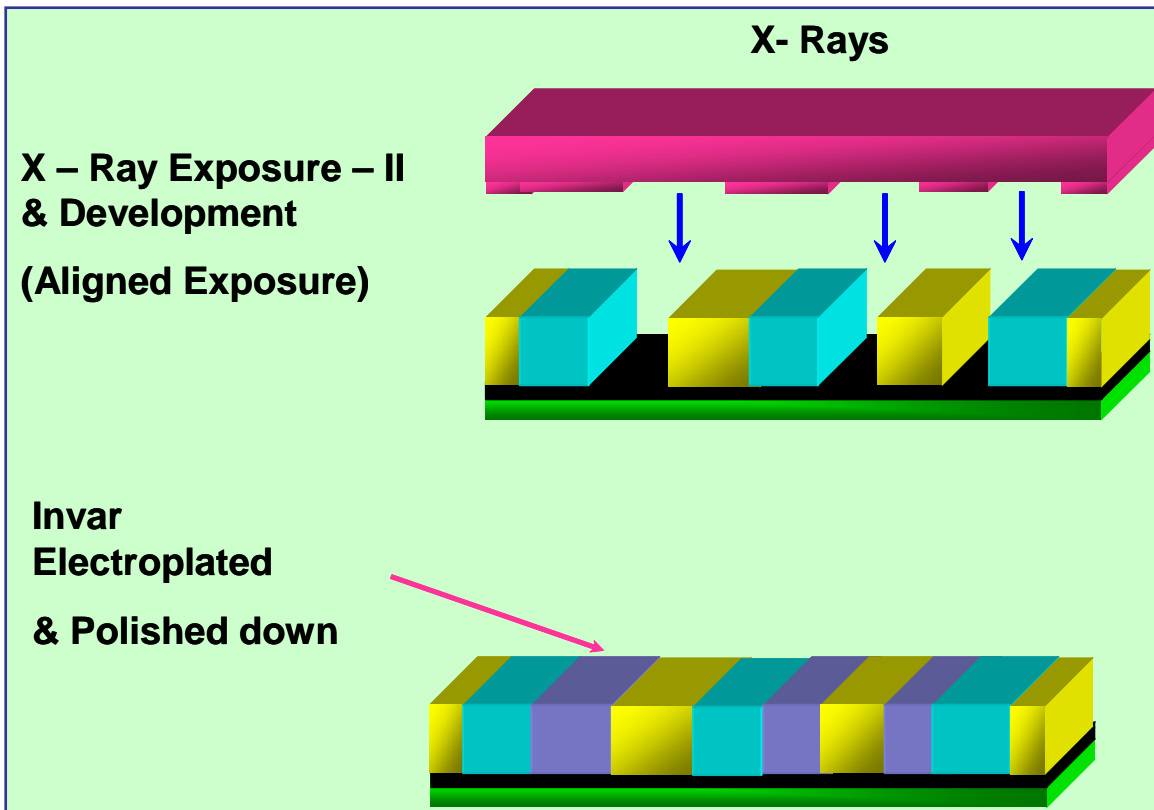
Table C.2 Atomic Proportions for Electroplated Invar

Atomic Proportions:				
Pt #	Distance	Fe	Ni	Total
All distances are measured from the bottom of the post to the top (μm)				
1	0	64.562	35.438	100
2	5	64.284	35.716	100
3	10	63.101	36.899	100
4	15	62.925	37.075	100
5	20	62.463	37.537	100
6	25	62.514	37.486	100
7	30	62.584	37.416	100
8	35	62.896	37.104	100
9	40	62.875	37.125	100
10	45	62.246	37.754	100
11	50	61.671	38.329	100
12	55	62.916	37.084	100
13	60	62.883	37.117	100
14	65	62.884	37.116	100
15	70	62.989	37.011	100
16	75	62.93	37.07	100
17	80	63.141	36.859	100
18	85	62.473	37.527	100
19	90	62.306	37.694	100
20	95	62.964	37.036	100
21	100	63.177	36.823	100
22	105	63.649	36.351	100
23	110	63.971	36.029	100
24	115	64.233	35.767	100
25	120	65.274	34.726	100
26	125	65.377	34.623	100
27	130	65.415	34.585	100
28	135	65.189	34.811	100
Average Value		63.3529	36.64671	100

APPENDIX – D

PROCESS SHEET FOR FABRICATION OF BI-MORPH RECURVE





APPENDIX E

RECIPE AND DATA SHEETS FOR FABRICATION OF DEVICE

Table E.1: Titanium oxidation solution

Chemical	Molarity
Sodium Hydroxide	0.5 M
Hydrogen Peroxide	0.2 M

Table E.2: PMMA Bonding glue composition

Chemical	Weight
85 % PMMA/MMA	5 g
BPO	0.075 g
MEMO	0.05 g
DMA	0.05 g

Table E.3: GG Developer solution

Solution	(ml)
2-(2-Butoxyethoxy) ethanol / diethyl glycol butyl ether	900
Morpholine	300
2-Aminoethanol	75
DI water	225
Total	1500

Table E.4: GG Rinse

Solution	(ml)
2-(2-Butoxyethoxy) ethanol / diethyl glycol butyl ether	1200
DI water	300
Total	1500

APPENDIX F

EXPERIMENTAL RESULTS

Table F.1 Raw data obtained from experimental results

Sample 1		Sample 2	
Temperature	Deflection	Temperature	Deflection
39.9969	-24.9307	40.0198	-20.1036
40.002	-39.6303	40.02	-24.4339
40.0074	-35.9406	40.0199	-21.8645
40.008	-38.2341	40.0192	-21.5713
40.011	-34.8867	40.019	-20.1272
40.011	-36.9961	40.0186	-18.9137
40.0128	-28.4609	40.0184	-20.2932
40.0131	-28.6306	40.0183	-15.7502
40.0138	-34.7595	40.0187	-15.1244
40.0148	-29.1387	40.0168	-14.0109
40.0149	-24.6371	40.0161	-11.8012
40.0158	-30.9677	40.016	-10.668
40.0184	-36.4687	40.0145	-10.8893
40.0201	-39.4387	40.0154	-19.1879
40.0221	-12.3507	40.0137	-11.8205
40.0229	-11.0067	40.0149	-16.2918
40.0287	-21.2358	40.0147	-11.2135
40.0345	-38.5002	40.0136	-15.1916
60.0235	-47.7198	60.0357	-30.6014
60.0245	-52.1996	60.0366	-26.26
60.0284	-41.0501	60.0376	-28.1324
60.0321	-32.5623	60.0379	-21.6115
60.0329	-36.6524	60.0386	-24.5959
60.0344	-39.6291	60.0392	-26.8398
60.0349	-53.8105	60.0405	-25.8227
60.0366	-34.1699	60.0405	-23.3895
60.038	-49.5256	60.0419	-26.0238
60.0385	-44.4703	60.043	-31.3533
60.0436	-44.1707	60.0439	-38.6906
60.0527	-32.8901	60.0446	-26.8953
60.0541	-49.1483	60.0457	-29.1484
60.0546	-27.6953	60.0468	-19.7045
60.0548	-39.5847	60.0475	-19.3438
60.0555	-37.0343	60.05	-23.2879
60.0615	-45.7474	60.051	-31.4053
60.0705	-47.8173	60.0512	-30.9543
79.9934	-30.8551	79.9947	-12.8417
79.9946	-39.0592	79.9965	-2.4026
79.9946	-32.7208	79.9987	-11.8924
79.9949	-46.1722	80	-30.0637
79.9978	-47.4042	80.0025	-37.5256

80	-27.3861	80.0038	-31.5775
80.0077	-34.6259	80.0074	-31.4045
80.0105	-36.1	80.0099	-39.4416
80.0106	-49.6501	80.0129	-29.8936
80.0155	-41.1335	80.0172	-27.7799
80.0258	-59.4736	80.0213	-32.1194
80.0278	-54.9851	80.0259	-29.4877
80.0317	-48.3631	80.0296	-28.3027
80.0355	-54.4132	80.034	-31.6852
80.0361	-47.5277	80.0394	-40.9375
80.0423	-54.3596	80.0434	-35.6305
80.0503	-56.6795	80.0469	-42.9982
80.0576	-52.5831	80.0473	-40.9908
99.9129	-52.2926	99.9269	-35.4906
99.9217	-41.5748	99.932	-39.0758
99.9312	-51.4073	99.9376	-34.4041
99.9437	-55.0667	99.942	-48.893
99.9609	-49.2096	99.9475	-26.2934
99.9694	-42.8685	99.9529	-35.5662
99.9723	-57.0076	99.962	-29.8354
99.978	-47.8642	99.9714	-29.1861
99.9795	-57.1544	99.9794	-35.9305
99.9904	-58.2865	99.9914	-35.4525
99.993	-44.3537	100.001	-22.427
100.0159	-46.189	100.011	-46.8178
100.0282	-55.0605	100.02	-22.1285
100.0315	-53.127	100.027	-33.7963
100.0324	-63.762	100.031	-37.1733
100.0362	-52.744	100.034	-42.0896
100.04	-48.2429	100.036	-40.649
100.0423	-21.2701	100.037	-41.8486
119.9992	-66.0168	120.002	-21.5001
120.0043	-55.6441	120.007	-32.2694
120.0068	-47.7166	120.01	-43.92
120.0106	-59.4435	120.013	-51.2998
120.0149	-46.4103	120.017	-43.4262
120.0152	-79.1047	120.019	-43.5852
120.0171	-68.0012	120.023	-37.4283
120.0277	-64.4514	120.028	-32.2707
120.0287	-45.2462	120.031	-39.9287
120.0305	-52.1433	120.035	-32.6801
120.0307	-28.2479	120.037	-38.5088
120.0413	-50.8658	120.039	-31.5668
120.047	-57.3188	120.041	-35.7453
120.0475	-37.8026	120.042	-44.8973
120.0527	-46.2257	120.045	-40.5664
120.0633	-55.2046	120.052	-30.774
120.0649	-35.4451	120.056	-32.5266
120.069	-42.7199	120.057	-42.6848
140.0199	-57.1882	140.027	-41.8382

140.0215	-50.5907	140.029	-61.3217
140.0284	-59.3554	140.031	-55.4193
140.033	-56.783	140.034	-48.4945
140.0355	-47.3437	140.035	-43.7438
140.0388	-60.6889	140.036	-62.7951
140.04	-41.7627	140.039	-48.0617
140.0406	-57.689	140.041	-33.2947
140.0429	-68.5392	140.042	-43.5063
140.0481	-42.0931	140.043	-53.491
140.0499	-54.9603	140.045	-43.2057
140.0521	-48.6544	140.046	-45.3506
140.0535	-60.1456	140.046	-46.5152
140.0554	-49.7908	140.045	-38.807
140.0577	-44.6338	140.046	-51.6225
140.0617	-46.0979	140.046	-43.1608
140.0636	-66.1033	140.049	-36.7389
140.077	-65.9229	140.051	-36.75
160.0465	-57.868	160.065	-57.972
160.0508	-47.5643	160.065	-62.8935
160.0533	-52.3509	160.066	-51.6891
160.0579	-40.0485	160.066	-33.5234
160.0582	-51.0305	160.067	-36.4539
160.0648	-51.8662	160.066	-57.7574
160.0656	-54.4824	160.068	-75.0567
160.0658	-69.5275	160.068	-57.4881
160.0687	-57.0524	160.069	-37.5998
160.0699	-66.092	160.07	-63.0424
160.0714	-55.4506	160.07	-31.7695
160.0717	-53.7582	160.07	-62.2311
160.0739	-57.5576	160.071	-35.8139
160.0769	-75.8268	160.072	-66.7084
160.0773	-72.7323	160.073	-51.2471
160.0855	-55.8477	160.075	-30.2535
160.0929	-49.4419	160.076	-53.4811
160.0962	-48.0599	160.077	-63.8006
180.0561	-66.1945	180.072	-58.7479
180.0589	-51.4132	180.072	-57.9688
180.0608	-66.6967	180.073	-56.1836
180.0695	-61.238	180.073	-54.0561
180.0712	-56.5376	180.073	-57.3057
180.0752	-60.3057	180.074	-66.2051
180.0779	-54.672	180.073	-83.0203
180.082	-70.815	180.075	-55.6301
180.0823	-50.7819	180.076	-54.4793
180.0831	-83.5542	180.075	-59.4625
180.0835	-52.3995	180.075	-63.2717
180.0843	-47.5558	180.076	-58.4754
180.0847	-47.6068	180.078	-50.5896
180.0848	-45.5116	180.079	-55.6865
180.0884	-49.2631	180.079	-57.0789

180.0895	-54.1588	180.08	-58.3623
180.0955	-65.4784	180.08	-81.042
180.1013	-52.1973	180.08	-50.7711
200.0737	-45.1318	200.088	-51.985
200.0747	-56.8609	200.088	-51.2062
200.0789	-62.2101	200.088	-68.6594
200.08	-52.0223	200.088	-68.5045
200.0824	-63.0068	200.088	-71.0705
200.0832	-62.8852	200.088	-64.9078
200.0863	-57.0641	200.088	-80.392
200.0879	-68.3448	200.088	-60.124
200.0892	-75.1417	200.088	-82.4559
200.0905	-86.9541	200.088	-65.0772
200.0911	-55.7933	200.087	-45.4939
200.0918	-58.2837	200.089	-68.3408
200.0927	-68.9638	200.088	-91.2373
200.0956	-51.2925	200.088	-46.4391
200.1009	-61.0644	200.087	-90.6072
200.101	-50.571	200.087	-71.4934
200.1017	-58.4429	200.083	-39.2984
200.1033	-57.2841	200.084	-54.0676
220.0762	-45.4038	220.096	-66.3329
220.0804	-56.326	220.097	-24.5395
220.0809	-53.8276	220.096	-73.0695
220.0851	-63.9426	220.097	-51.2772
220.0854	-42.3418	220.097	-75.7342
220.0874	-57.2271	220.096	-89.3568
220.0886	-77.1047	220.096	-40.4324
220.091	-64.1915	220.096	-87.8268
220.091	-68.7151	220.095	-72.2338
220.0929	-48.8061	220.095	-59.509
220.0948	-40.7066	220.095	-57.623
220.0971	-51.3368	220.094	-50.1494
220.0971	-71.5115	220.093	-63.894
220.0982	-64.4794	220.093	-64.0283
220.1008	-37.949	220.092	-71.7637
220.1014	-47.3945	220.089	-72.2186
220.1089	-63.9186	220.088	-62.1914
220.1141	-37.7947	220.088	-69.943
240.0834	-49.4563	240.106	-38.8597
240.0893	-43.5639	240.105	-40.2418
240.0909	-50.5499	240.105	-46.8078
240.0929	-44.1156	240.104	-56.5455
240.0929	-42.2328	240.105	-56.5063
240.0947	-52.7881	240.104	-42.119
240.0971	-53.2792	240.104	-49.5859
240.098	-46.2875	240.104	-46.2531
240.1002	-58.1695	240.103	-57.9305
240.1009	-45.7319	240.103	-50.043
240.1027	-50.9082	240.102	-42.5283

240.1049	-48.2802	240.101	-51.0213
240.1055	-42.7527	240.101	-36.3875
240.1113	-53.2845	240.099	-36.1344
240.1118	-46.7487	240.097	-57.1291
240.114	-48.9746	240.094	-42.1895
240.1142	-36.1124	240.092	-39.1357
240.1308	-57.777	240.09	-46.674
260.0856	-59.0814	260.108	-47.2218
260.0885	-41.4937	260.108	-52.5385
260.0887	-49.9899	260.108	-36.4463
260.0926	-36.8676	260.108	-62.8736
260.0926	-48.4337	260.108	-50.0148
260.094	-50.7126	260.106	-68.3617
260.0946	-57.949	260.107	-38.6316
260.0954	-38.1531	260.104	-52.3467
260.0997	-35.8422	260.104	-47.649
260.1013	-44.8439	260.103	-51.8641
260.102	-39.8499	260.103	-57.6443
260.1033	-45.6526	260.101	-60.5506
260.1038	-30.7144	260.1	-47.5848
260.1105	-54.1872	260.098	-52.6358
260.1131	-51.7778	260.094	-57.6428
260.1172	-50.3261	260.092	-39.9129
260.1177	-58.1169	260.087	-39.2283
260.1219	-37.7956	260.086	-76.4912
280.0832	-61.2224	280.104	-47.3524
280.0859	-63.6975	280.104	-46.6348
280.0914	-48.4097	280.104	-54.3469
280.0937	-30.6097	280.103	-27.1803
280.0941	-40.9964	280.104	-40.2727
280.0962	-39.4964	280.103	-48.0736
280.0993	-37.6621	280.103	-41.0104
280.1013	-64.1621	280.102	-40.0975
280.104	-50.405	280.1	-48.4715
280.1058	-56.135	280.1	-40.9793
280.1063	-38.5253	280.097	-45.2131
280.1068	-26.3774	280.096	-38.1479
280.1071	-25.5797	280.094	-26.8885
280.1101	-42.4501	280.09	-41.6389
280.1112	-45.8983	280.088	-40.543
280.1146	-32.7538	280.084	-59.8147
280.1172	-55.1023	280.081	-36.2582
280.1195	-45.2887	280.081	-25.9012
300.073	-39.0311	300.101	-34.3468
300.0777	-45.2232	300.101	-41.13
300.078	-54.0931	300.101	-32.7311
300.0784	-62.7723	300.099	-31.1311
300.0866	-27.3935	300.1	-35.4022
300.0894	-35.6012	300.1	-28.5746
300.0899	-34.0949	300.099	-22.2567

300.0914	-70.4702	300.098	-48.2119
300.0917	-74.0882	300.097	-46.1113
300.0927	-39.922	300.096	-37.8233
300.0949	-66.6763	300.096	-21.8652
300.0965	-34.1942	300.094	-28.7041
300.0965	-40.0225	300.092	-18.6344
300.1029	-17.066	300.091	-39.641
300.1035	-33.3238	300.088	-21.6908
300.1073	-15.2552	300.083	-37.0459
300.1115	-57.1785	300.078	-41.1648
300.123	-35.2351	300.077	-39.3033

APPENDIX G

COMMAND FILE FOR DEFLECTION OF RECURVE ELEMENT UNDER THERMAL LOAD

G.1 The command file below was used to generate the model in ANSYS. The entire analysis was performed interactively thereafter.

```
/Title, Deflection of bimetallic cantilever under thermal load
```

```
/PREP7
```

```
BLC4,0,0,100,100,500
```

```
BLC4,0,100,2000,200,500
```

```
BLC4,0,300,8000,200,500
```

```
BLC4,7900,0,0,100,100,500
```

```
BLC4,6000,100,2000,200,500
```

```
BLC4,2000,500,4000,200,500
```

```
BLC4,3950,700,100,100,500
```

```
MPTEMP,1,0
```

```
MPDATA,EX,1,,181e-3
```

```
MPDATA,PRXY,1,,0.3
```

```
MPDATA,DENS,1,,8.9e-15
```

```
MP,ALPX,1,13.3e-6
```

```
MP,KXX,1,60.7e-6
```

```
MPTEMP,1,0
```

```
MPDATA,EX,2,,148e-3
```

```
MPDATA,PRXY,2,,0.3
```

```
MPDATA,DENS,2,,8.05e-15
```

```
MP,ALPX,2,4.18e-6
```

```
MP,KXX,2,10.15e-6
```

```
ET,1,SOLID87
```

G.2 Procedure for interactive analysis

1. Material properties are assigned to specific volumes.
2. The entire recurve structure is meshed using auto mesh generation.
3. Reference temperature is set and thermal loads are applied.
4. The problem is solved.
5. The results of thermal analysis are stored in 'filename.rth' file.
6. The thermal degrees of freedom are converted to structural degrees of freedom.
7. Structural loads are applied.
8. The results of thermal analysis are transferred to the nodes of the recurve.
9. The problem is solved to obtain deflection results.

VITA

Madhulika Sathe was born in Jamshedpur, India, on November 14, 1978, to Meera and Dilip Sathe. She completed her undergraduation in mechanical engineering in India before coming to LSU in Fall 2000.

While at LSU, she gained work experience at the Center for Advanced Microstructures and Devices (CAMD). She completed her thesis in Fall 2003, but her defense was delayed until Summer 2004. She expects to receive her degree of Master of Science in Mechanical Engineering in Fall 2004.